Aerial Manipulators for Contact-based Interaction

By

SALUA HAMAZA

Department of Aerospace Engineering
UNIVERSITY OF BRISTOL

A dissertation submitted to the University of Bristol in accordance with the requirements of the degree of DOCTOR OF PHILOSOPHY in the Faculty of Engineering.

OCTOBER 2019

Word count: 43431

Abstract

In this thesis, new methods are proposed to tackle contact-based manipulation conducted by flying robots. The exertion of force and physical interaction are challenging tasks when performed on an aerial vehicle. The research community in aerial robotics started to approach such challenges in the past decade, with the use of interaction controllers tailored at *aerial manipulators*. Force exchange by an aerial vehicle was only tackled in more recent years however, as the state of the art progressed and reached higher maturity. The work hereby presented addresses some of the challenges of contact-based aerial interaction and proposes a novel approach to force generation by exploiting the aerial system as a whole, combining the action from the manipulator together with motion of the aircraft. A bespoke manipulation system featuring compliance is created to tackle force-driven tasks where the ability to adjust the force output, shape the load curve and tune the time in contact according to the task specifications is demonstrated throughout multiple experiments. Optimisation is carried out at both the design and control level, to further expand on the range of applications that can be accomplished with the compact, lightweight and compliant design. This, together with novel control strategies for aerial interaction allow to perform new aerial tasks, such as pushing against and tapping on a surface, install and retrieve sensors on vertical and cylindrical surfaces, and aerial contour following. Overall the proposed approach demonstrates accuracy, robustness and reliability to tackle contact-based aerial operations in multiple scenarios.

Dedication and acknowledgements

The author of this thesis would like the acknowledge the support given by Eugenio during the whole PhD journey. Along with his continuous encouragement and advice, comes the loving support of my parents. A special thank goes to my supervisors Tom and Ioannis, who guided me in this journey and contributed to shape the researcher I am today.

AUTHOR'S DECLARATION

I declare that the work in this dissertation was carried out in accordance with the requirements of the University's Regulations and Code of Practice for Research Degree Programmes and that it has not been submitted for any other academic award. Except where indicated by specific reference in the text, the work is the candidate's own work. Work done in collaboration with, or with the assistance of, others, is indicated as such. Any views expressed in the dissertation are those of the author.

SIGNED: ..... DATE: .....

TABLE OF CONTENTS

List of Abbreviations

CAD Computer Aided Design

CoG Centre of Gravity

CoM Centre of Mass

DoF Degree of Freedom

EE End-Effector

MPC Model Predictive Control

NDT Non Destructive Testing

PD Proportional Derivative

PI Proportional Integral

PID Proportional Integral Derivative

QEI Quadrature Encoder Interface

ROS Robotic Operating System

SLAM Simultaneous Localisation And Mapping

UAM Unmanned Aerial Manipulator

UAV Unmanned Aerial Vehicle

VTOL Vertical Take-Off and Landing

List of Tables

Table **Page**

List of Figures

Figure **Page**

PUBLICATIONS AND INTELLECTUAL PROPERTY

Conference Articles

1. Hamaza, S., Georgilas, I., and Richardson, T. (2018, July). An adaptive-compliance manipulator for contact-based aerial applications. In *2018 IEEE/ASME International Conference on Advanced Intelligent Mechatronics (AIM)* (pp. 730-735). IEEE.

2. Hamaza, S., Georgilas, I. and Richardson, T., 2018, October. Towards An Adaptive-Compliance Aerial Manipulator for Contact-Based Interaction. In *2018 IEEE/RSJ International Conference on Intelligent Robots and Systems (IROS)* (pp. 1-9). IEEE.

3. Hamaza S., Georgilas I., Richardson T. (2019) Energy-Tank Based Force Control for 3D Contour Following. In *Towards Autonomous Robotic Systems* (K. Althoefer,J. Konstantinova, and K. Zhang, eds.), (Cham), pp. 41–51, Springer International Publishing, 2019.

4. Hamaza, S., Georgilas, I., and Richardson, T. (2019, November). 2D Contour Following with an Unmanned Aerial Manipulator: Towards Tactile-Based Aerial Navigation. In *2019 IEEE/RSJ International Conference on Intelligent Robots and Systems (IROS)*, IEEE.

Journals

1. Hamaza, S., Georgilas, I., Fernandez, M., Sanchez, P., Richardson, T., Heredia, G., Ollero, A. (2019). Sensor Installation and Retrieval Operations using an Unmanned Aerial Manipulator. *IEEE Robotics and Automation Letters, 3*(4), 2793 – 2800.

2. Hamaza, S., Georgilas, I., Heredia, G., Ollero, A., Richardson, T. "Design, Modeling and Control of an Aerial Manipulator for Placement and Retrieval of Sensors in the Environment." *Journal of Field Robotics* (2019). – in print.

3. Bartelds, T., Capra, A., Hamaza, S., Stramigioli, S., Fumagalli, M. (2016). Compliant aerial manipulators: Toward a new generation of aerial robotic workers. *IEEE Robotics and Automation Letters, 1*(1), 477-483.

Intellectual Property

UK patent filed by the University of Bristol – June 2017

- ▷ Application Title: Manipulator & Control Systems;
- ▷ Application Number: GB1708808.9

Awards

IEEE Robotics and Automation Letters Best Paper Award

- ▷ *Bartelds, T., Capra, A., Hamaza, S., Stramigioli, S., and Fumagalli, M. (2016). Compliant aerial manipulators: Toward a new generation of aerial robotic workers. IEEE Robotics and Automation Letters, 1(1), 477-483.*

CHAPTER 1

INTRODUCTION

In the past few decades the increasing interest towards Unmanned Aerial Vehicles (UAVs) has sprouted a number of industrial and civil applications in which these platforms are being used. Thanks to their unbounded workspace and inherent versatility, UAVs are deployed for a number of contact-less operations which exploit advanced on-board sensing, e.g. cameras, pressure sensors, flow sensors, LIDAR. Some example applications in which aerial vehicles are currently being used are civilian security, border security, fire and rescue, mountain rescue, distribution network monitoring, environmental monitoring, aerial photography, mapping and surveying. Despite proving very useful and successful, these applications are mostly limited to passive observation. However, huge potential lies in tasks that do require manipulation and physical interaction with the environment.

In the past decade a new research area has risen, *aerial manipulation*, which considers endowing multicopters with mechanical devices to enable airborne manipulation tasks. Multicopters, e.g. quadcopters, hexacopters, octocopters, are Vertical Take-off and Landing (VTOL) aircraft that can hover, take off, and land vertically. This feature, together with the ability to fly stably at low speeds, higher manoeuvrability with respect to fixed-wing UAVs, and greater payload capacity has made them particularly attractive for these type of applications. Unmanned Aerial Manipulators (UAMs) could be deployed to carry out inspection and maintenance operations in remote areas and hard-to-reach locations, performing tasks that are too risky for human operators and that require costly equipment. Example scenarios where UAMs could be exploited can include cracks repair

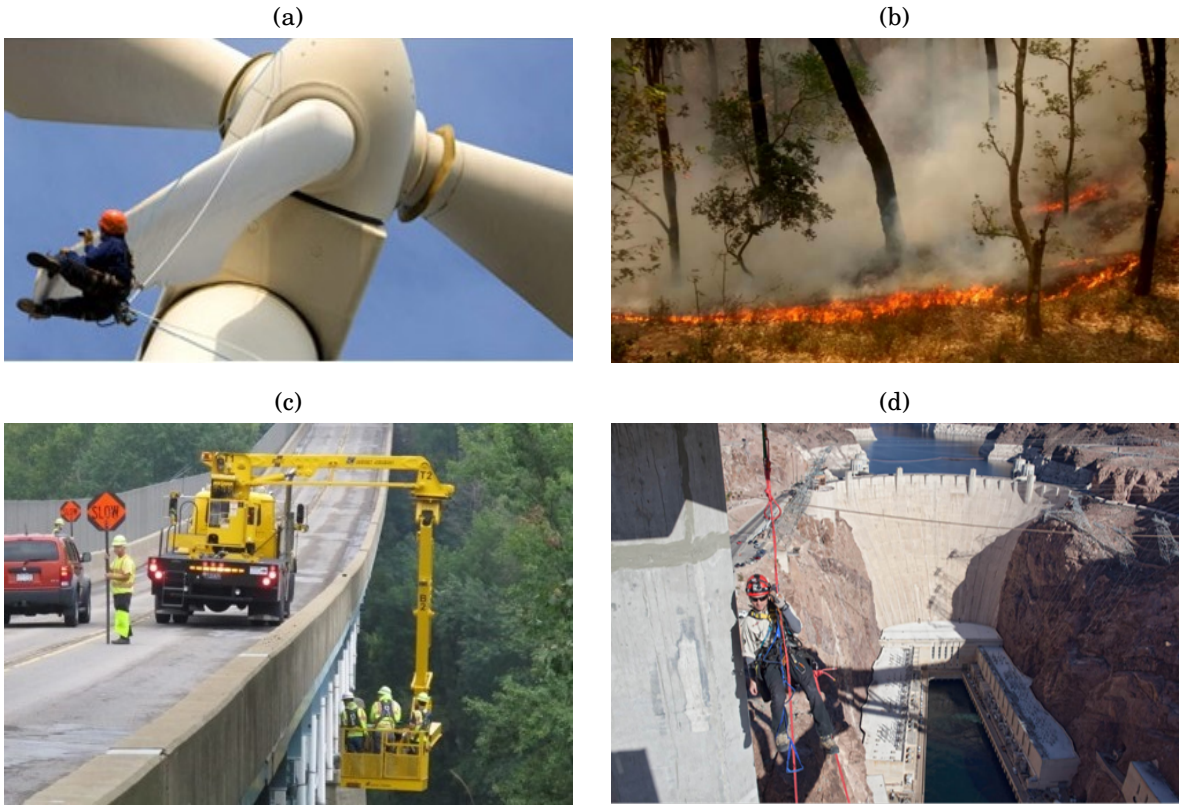

Figure 1.1: Example application scenarios for the deployment of unmanned aerial manipulators in the environment to (a) perform continuity checks on top of wind turbine blades; (b) install smoke detectors in forests for fire prevention; (c) monitor the induced traffic vibrations on bridges; (d) check the slope stability on dams.

on wind turbine blades, cleaning of clogged-up thermocouples on industrial chimneys, contact-based inspection of bridges and dams, installation and retrieval of smart sensors in wide spread areas for monitoring purposes. Figure 1.1 shows some possible scenarios for the deployment of UAMs. All these tasks are nowadays conducted by human operators and often require supporting structures such as scaffolding around the area or other special equipment to allow the operator to reach the site and safely conduct inspection and maintenance tasks. For these reasons, such example scenarios have been the case study of several investigations as part of multiple European funded projects in the past years, starting from AIRobots [7] in 2010 until more recent project such as ARCAS, Aeroarms, Aerobi, AEROWORKS, [8–11].

1.1 Motivation and Research Objectives

1.2 Background

Aerial vehicles are often solely used as agile sensing platforms, incapable of interacting with the environment. However, if manipulation capabilities could be embedded for UAVs, they could perform a much wider variety of tasks that involve contact with the environment. For example *aerial manipulators* could be deployed for maintenance and inspection tasks of infrastructure in hard-to-reach locations, or contact-based surveying of wide-spread areas. The state of the art in aerial manipulation up to now has mostly focused on grasping and load transportation with flying robots. To achieve aerial grasping, tools such as grippers, clamps or robotic hands are often attached directly to the UAV's frame in the centre part of its body, bringing a simple yet effective addition to the design.

Contact-based interaction is however more challenging to accomplish: as the UAV interacts with another rigid body, the perturbations generated by the exchange of forces and moments need to be counteracted by the aerial platform in real time. The dynamics resulting from such interaction therefore require the development of more complex control laws in order to achieve a safe flight and a good performance. Moreover, to carry out more generic manipulation tasks that extend from the simple *grasping*, a higher level of dexterity is required from the robotic manipulator. This prompted the research community to develop manipulators with more complex designs, wider workspace and higher versatility to accomplish a broad range of aerial tasks.

1.2.1 Open Challenges in Aerial Manipulation

A number of challenges arise from UAVs manipulating objects airborne and interacting with the environment. First and foremost, as the aerial manipulator exchanges forces and moments in the environment, the reaction forces are propagated from the external body to the vehicle leading to both linear and angular disturbances, e.g. drifting, oscillations, instability. The UAV has to counteract those disturbances in order to perform a safe interaction and also fulfil the task. Other types of disturbances experienced by aerial manipulators are those induced by turbulence in the close proximity with obstacles: as the UAV hovers close to a wall, ceiling or any other object, its aerodynamics are affected regardless an interaction is taking place. Both kinds of disturbances affect the UAV's dynamics and therefore its stability in-flight. Typically these challenges are addressed

by researchers by incorporating optimal controllers, model predictive methods or other compliant controllers as part of the vehicle flight controller.

Other challenges in aerial manipulation relate to the design of the manipulation system itself. The tight payload requirements of UAVs and the limited available flight time pose the biggest limitations to the design of the manipulator. Typically UAVs can fly between 15 to 25 minutes depending on the size of the battery, however the flight time is drastically reduced when extra weight is added onto the platform. Moreover as the manipulator operates, the moving masses acting on it can further destabilise the vehicle and drain the battery life. Other technological limitations are posed by the efficiency of the manipulator and its volume: a compact design is preferable as it minimises the overall inertia of the aerial platform, therefore favouring the vehicle's dynamics and response. Besides meeting the UAV's requirements, the manipulator also needs to satisfy the task requirements. Ideally the manipulator will need to have a certain degree of adaptability and versatility to allow its use in multiple scenarios, by providing an adequate workspace, range of motion and dexterity. On the other hand, higher dexterity and range of motion come at the cost of using multiple actuators that increase the overall mass and inertia of the system, leading to a shorter battery life and instability problems due to the moving masses.

The above challenges have been addressed over the years by the research community in aerial robotics, and tailored solutions have been developed to tackle some of those. Further discussion on the advances brought to the state of the art in aerial manipulation are presented in the following chapter.

Within this thesis, some of the challenges related to the design of the manipulation system tailored for aerial manipulation are addressed. In particular, the focus of this work will be to develop a system that is versatile and adaptable for a variety of contact-based tasks; that is lightweight and compact to minimise the impact it has on the aerial system's dynamics and performance, and that is capable of fulfilling contact-based interaction through the exertion of force in a robust and repeatable way.

1.2.2 Research Objectives

From the state of the art in aerial manipulation, it can be noted that little is present demonstrating the ability of UAMs to exert forces in the environment for tasks such as probing, tapping, pushing, marking of cracks, object installation, or more general non destructive testing (NDT). Such tasks are challenging to achieve on a UAV for the reasons outlined in the previous subsection. The aim of this research is to demonstrate

the ability of UAMs to interact with the environment for force-driven applications using a tailored manipulator design which allows for versatility, robust force exchange and a repeatable outcome. From the challenges highlighted above, the following research objectives have been derived to develop a novel aerial manipulator for contact-based interaction:

- the analysis of the variables involved in aerial physical interaction: which parameters affect the interaction, and in which way? Which are the critical design variables that play a role in the vehicle's dynamic response?
- the design of a bespoke manipulator for force-driven applications: following the above analysis, how can the design of a manipulation system facilitate the vehicle's dynamics for force-based interaction on the side of a UAV? which are the critical design parameter to consider when designing a manipulator for these intended tasks? how many degrees of freedom are necessary? what are the essential features of such manipulator?
- manufacturing and integration with the aerial platform, control and flight experiments of basic force-based operations: demonstrating preliminary force-based tasks that involve pushing and tapping operations against a vertical surface, analysis of forces and UAV stability;
- design & control refinement: to what extent the dynamic interaction between an aerial manipulator and its environment can be improved? Can the force curve be adjusted to follow task-specific requirements? How can the aerial system contribute towards the force exchange in synergy with the manipulator, acting as a single system? Combining control with *intelligent* body design and sensing, addressing both hardware and software refinement.
  - Real time force control and the integration of the UAV state in the 'loop'. Demonstration through flight experiments of realistic applications such as sensor installation and retrieval performed indoors over flat surfaces and outdoors on irregular cylindrical surfaces, i.e. tree trunks.
  - Passivity-based force control to tackle accurate and continuous application of a shear force for a prolonged period of time over a flat surface. Stationary experiments demonstrating the control robustness for contouring of 3D profiles. Flight experiments demonstrating 2D contour following capabilities, ideally suited for tactile-based indoor navigation of aerial robots.

1.3 Thesis Outline

This thesis is structured in 7 chapters. Chapter 1 includes an introductory background on the topic of aerial manipulation followed by the motivation which drove this work. Chapter 2 presents a review on the state of the art of aerial manipulation and highlights the key works in the field with detailed comparison and analysis. Chapters 3, 4, 5 and 6 are the core chapters of this thesis and it's where the methodology employed in this work is being presented and discussed. Chapter 7 presents the conclusions drawn from this work, together with the lessons learnt and the takeaway message. A more detailed breakdown of the core chapters in this thesis is hereby presented.

Chapter 2 presents a detailed discussion on the state-of-the-art of aerial manipulation. The works highlighted in this chapter are presented in chronological order and grouped by common challenges faced and results achieved within the aerial robotics community in the past decade. Chapter 3 presents a study of the variables involved in aerial interaction and the detailed design process for the manipulation system. Equipping the aerial system with an on-board manipulator may lead to several disadvantages in terms of stability, manoeuvrability and endurance of the flying robot. To understand how the aerial vehicle is affected by the presence of the manipulator and address the design of such, several tests are conducted in a simulation environment. The results of simulated experiments highlight the critical design parameters that pave the road to the design process for a manipulation system tailored at force-driven tasks. The manipulator design is presented, detailing the working principle of the 2 degrees of freedom (DoFs) mechanism and the mechanical integrity of its components and materials. The proposed manipulator consists of a compact and lightweight structure, and features actively variable compliance to safely interact with the environment and operate contact-based inspection or non destructive testing.

Chapter 4 validates the proposed aerial manipulator for applications such as pushing or tapping on a vertical surface. To start with, the integration of the manipulator with the flying platform is presented together with sensing and the control used to achieve active variable compliance. Multiple flights results demonstrate the ability of the proposed design to exert a range of forces in the environment and the ability to adjust the force output by tuning the manipulator compliance. The presence of the adaptively compliant manipulator is also seen in the aircraft dynamic response during interaction and in the in-flight stability. Additional flight results also demonstrate the ability to apply a series of rapid pulses over a surface (tapping) for the excitation of an object or surface, and

other NDT purposes.

Chapter 5 validates the proposed aerial manipulator for applications such as the installation and the retrieval of smart sensors in the environment. The manipulator's refinement in terms of mechanics, sensing, electronics and system integration is initially addressed. A new control approach is then implemented for the proposed manipulator suited for the positioning of smart sensors in the environment, based on force control. The integral action of the manipulator and the aerial vehicle allows to seamlessly combine the force output of each subsystem and to successfully install and retrieve sensors over flat and cylindrical surfaces (i.e. tree trunks) and in both an indoor and outdoor setting. Multiple experiments demonstrate the robustness of this approach in different challenging scenarios, followed by an in depth analysis of the results.

Chapter 6 validates the proposed aerial manipulator for applications such as aerial contour following for indoor navigation purposes. The control laws are initially formulated: a passivity-based approach is taken for the proposed manipulation system based on virtual energy tanks. This enables a compliant response at the end-effector and allows the aerial manipulator to exert a continuous shear force over a surface in a robust way. The integration of this controller together with on-board sensing allows for real-time adjustments of the force output whilst in contact, preserving the vehicle stability and overcoming any disturbances, e.g. drifting of the aircraft. The envisioned aerial application for such contour following is to aid indoor navigation of UAVs, for example in a search and rescue scenario. The results demonstrate the robustness of the approach and its potential towards aerial tactile-based navigation.

CHAPTER 2

LITERATURE REVIEW

Aerial Manipulators are a class of unmanned aerial vehicles that have the capability to perform physical interaction on an *ideally* unbounded workspace. In the past decade, a research focus in the field of aerial manipulators has risen to address the several limitations of aerial manipulators. Being floating bases, UAVs face more challenges to interact with the environment with respect to ground robots, as all reaction moments and forces need to be counteracted by the platform in flight and aren't transferred into ground.

The key driving factors of aerial manipulation research are: stable flight in the proximity of walls and other obstacles; the design of manipulation systems tailored at aerial robotics applications; the magnitude, the period of application and the shape of the force profile exerted by the aerial manipulator in flight; the positioning accuracy of the vehicle and the manipulator while performing a manipulation task. All of these topics have driven a major boost in aerial manipulation research in the past decade, and all of these present several challenges that have been tackled individually or jointly by researchers in the community.

In this chapter, a chronological review of the state of the art in aerial manipulation is presented. The discussion will be staged in sections, grouping the works that have common goals and results to allow better clarity on the advances within one topic.

2.1 The Early Stages

Aerial interaction sees its dawn in 2009 with slung load transportation and object deployment proposed by [12], and later by [13, 14]. Grasping in air is achieved thanks to a fixed hand-tool or gripper mounted on the rotorcraft frame, and it represents the first step in the field of *manipulation* bringing a useful addition to the vehicle capabilities. In fact, load transportation can be used for the delivery of first-aid packages to isolated victims in post-disaster areas (e.g. areas exposed to floods, earthquakes, fires, industrial disasters and others) and lays the foundation for future development in cooperative load transportation and tele-operation conducted by multiple aerial robots [15–18] and cooperative assembly systems [19–21]. Within these works, the main focus was to guarantee stable flight while transporting a load and therefore compensate for it in the altitude dynamics. Typically, stability has been achieved with the use of optimal controllers that improve hovering in the proximity of the ground during lift and release of the object, or in proximity of other obstacles.

Contact-based interaction on the side of a UAV was formerly introduced by Albers [1] where a quadrotor is endowed with an additional propeller oriented horizontally to generate a normal force to a vertical wall for cleaning purposes. No specific design for a manipulator is proposed but rather the addition of a cleaning tool/brush to use such force output for cleaning purposes, as illustrated in Figure 2.1. In addition to the quadrotor flying control system, a micro controller is used to collect and process the data from the ultrasonic rangefinder and to aid the control loop for the horizontal propeller. The set-point is given by the pilot and a simple PID controller allows acceleration of the horizontal propeller within given bounds so as to bring the UAV to its position in x-direction. Key results show that a mean force of 2.5 N is achieved over a period of 50 seconds. Carrying a an additional payload of 200 grams, the maximum flight time registered with this setup is 6 minutes, drastically reduced when the horizontal propeller is on. Despite the apparent short flight-time, it is to be noted that custom made UAVs typically fly under 15 minutes, whereas long-range commercial drones can reach up to 25 minutes in air. In this particular setup, the addition of the extra propeller and other electronics on-board caused an early-drainage of the battery life, which is to be expected with small sized platform that have limited payload. This work clearly shows the technological limitation of battery capacity and power transmission associated with aerial manipulators and, more in general, with UAVs. Overall, the major drawbacks associated with the results presented in this work relate to to the limited flight time

due to the presence of the extra rotor on-board, and a poor adaptability of the system in terms of the narrow scope of applications that can be achieved with the fixed tool (cleaning brush).

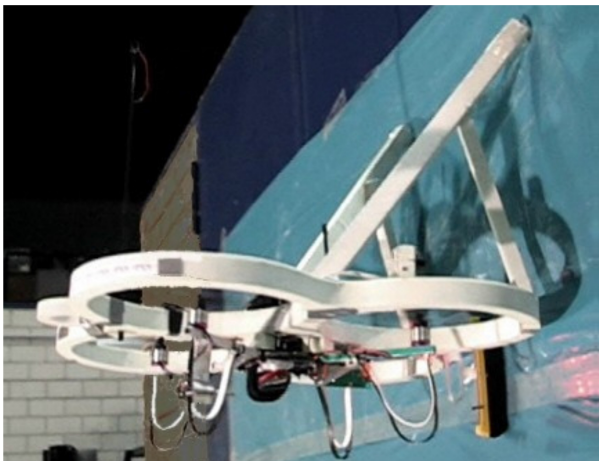

Figure 2.1: An unmanned aerial vehicle with a fixed brush tool on the side deployed for window cleaning. - [1]

In the same year, E. Pounds and A. Dollar [22] proposed a small RC helicopter for aerial grasping. The gripper mechanism is mounted internally between the aircraft's skids; the landing gear is raised during grasping to avoid contact with the ground or target objects. The under-actuated compliant gripper allows for positional errors between the helicopter and the target object. To acquire an object, the helicopter approaches the target, descends vertically to a hover state, and then closes its gripper. Once a solid grasp is achieved, the helicopter ascends with the object. Later in 2011, Pound et al. [23] study the stability of the helicopter in contact with the object. In particular, the longitudinal dynamics are examined together with the payload pitching effect on the overall system. The stability analysis is carried out by consideration of the pitching momentum due to the payload, the rotational inertia of the helicopter, and the height of the rotor plane above the centre of gravity (CoG). Ultimately, stability is formalised the Routh-Hurwitz criterion.

Grasping and cooperative load transportation with UAVs is also presented in [19, 24] where the designs of multiple compliant lightweight grippers directly attached to the aircraft frame are illustrated. In particular, the authors propose two types of robotic end-effectors: an *ingressive* one, i.e. one that can physically penetrate the surface of the target object, and an *impactive* one which can physically grasp by direct impact upon the object. In both cases, the inertial parameters of the object handled are estimated and

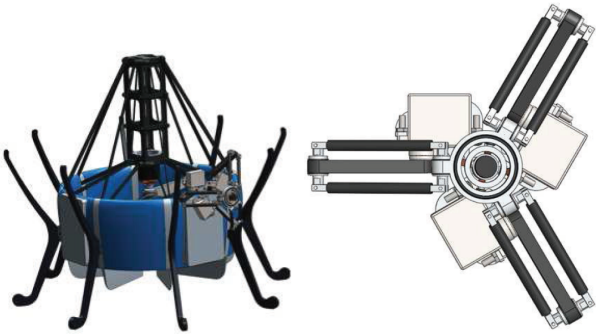

Figure 2.2: The AIRobots Manipulator: preliminary designs showing the ducted-fan and the delta robot. - [2]

used to adapt the controller and improve performance during flight.

In [2], Marconi et al. present some initial results of the European-funded project AIRobots that pioneered the field of aerial manipulation, [7]. The first prototype uses a ducted-fan UAV equipped with a lightweight Delta robot manipulator on the bottom part of the fan. The vertical axis of the Delta manipulator is tele-operated, i.e. the axis concerning the height of the Delta's end-effector, while the other degrees of freedom (DoFs) are controlled at a low level. Experimental results validate the design and the kinematics model, together with the tele-manipulation capabilities of the manipultor.

2.2 The Focus Towards Multi-DoFs Manipulators

Since 2012 the design of multi-DoF robotic arms for aerial manipulation begins. Differently from what is seen before, the focus is shifted from the optimisation of the UAV dynamics to the design of more versatile manipulation systems than offer more than just grasping. Korpela et al. [25] present their progress and results toward mobile manipulation by an unmanned aerial vehicle with dexterous arms and end-effector, outdoors. Towards this goal, the aim of their first work is to model and replicate reactive forces seen by the UAV in a gantry system, and simultaneously simulate changes in the CoG.

In the same year [3] Keemink et al. presented the mechanical design of a manipulation system that performs non-destructive ultrasonic tests on a boiler's wall. The novelty of their design lies in the use of a 3 degrees of freedom (DoFs) Delta robot endowed with a Cardan gimbal at the end-effector which provides 4 additional DoFs and higher accuracy with the benefit of using smaller actuators on the manipulation system, hence limiting the overall payload.

The configuration of the parallel Delta robot allows for planar motion (i.e. translation

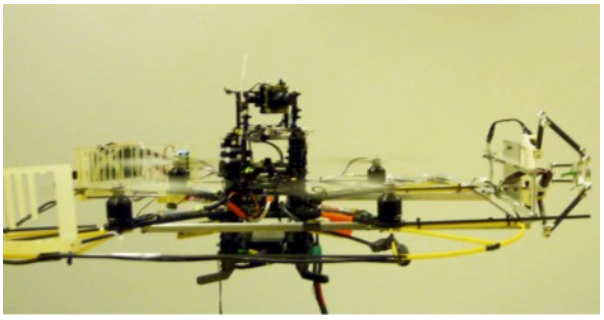

Figure 2.3: A UAV equipped with a parallel delta robot on the side deployed to perform contact inspection. - [3]

on x-y axes and rotation about the out-of-the-plane axis) and provides the manipulator with a fast and robust response. The inverse kinematics compensate for disturbances induced by the UAV dynamics at the end-effector and therefore achieve accurate positioning of the hand-tool. An impedance type of control regulates the force output at the end-effector. The key result associated with this work is the ability to exert a 5 N force on a vertical surface for side-way interaction.

Similarly in 2015 Danko et al. published their work [26] presenting a 6-DoFs parallel manipulator for airborne tasks. Their design's topology is inspired by a Stewart Platform, and relies on continuous position compensation at the end-effector. The proposed manipulator presents 6 motors at the base that each drive a revolute joint and two universal joints in series (6-RUU). Amongst the design criteria, the lengths of the manipulator's links have been chosen so that the manipulator can fold flat below the UAV whilst not manipulating. The accuracy of this design is shown during a hovering task in which external disturbances, i.e. a fan, destabilise the aircraft while the end-effector controller independently compensates for them. No interaction is however demonstrated within this work.

In 2015, Bellicoso et al. present a retractable lightweight robotic arm for aerial manipulation tasks [27]. The focus on the compact, foldable design is the key aspect of this work, which allows the arm to fold itself during take-off and landing operations. Experimental tests validate the dynamics, electronics and joint position control over the end-effector, however no physical interaction is demonstrated within this work.

2.3 Control Approaches to Aerial Manipulation

As the manipulator designs began to evolve over time, the controllers of the manipulators were optimised for contact-based interaction and force exchange. In 2012, Lippiello et al. present a Cartesian impedance controller [28, 29] for a quadrotor equipped with a 3-DoFs robotic arm. The controller provides a dynamic relationship between external generalised forces acting on the structure and the system motion. Hovering of the vehicle is tested in a simulation environment and the effects of contact forces and external disturbances are highlighted.

In [30], Fumagalli et al. propose an impedance type of controller for the manipulation system. The coupled models of the quadrotor and the Delta robot manipulator investigate the effects of the physical interaction over the aerial platform dynamics. Through this analysis, a passivity-based control law fulfils two functions: it stabilises the free-flight configuration and compensates position errors at the end-effector, and it allows the docking of the end-effector on a vertical surface. From the same authors, in [31] the ability to exert contact forces up to 3 N on a vertical wall is demonstrated with the use of the same compact Delta robot controlled in impedance, mounted on the surrounding structure of the aerial vehicle for gentle contact, NDT purposes.

In 2013 Kim et al. propose an aerial manipulator endowed with 2 robotic arms for grasping and release operations [32]. In this work the dynamical system is modelled through Lagrange-D'Alembert approach and an *adaptive sliding controller* is implemented. Successful pick-ups and releases of the object indoors are illustrated and the controller successfully compensates for induced momentum at the CoG.

A multi-link manipulator for assembly task is proposed by Jimenez et al. where a Variable Parameter Integral Back-stepping (VPIB) controller is implemented and compared to the use of standard PID controllers [33]. The proposed VPIB outperforms the PID in terms of the vehicle stability during outdoor flights.

In the same year, aerial mobile manipulation outdoors was achieved with the use of a small helicopter equipped with an industrial KUKA arm [34]. The force interaction between helicopter and manipulator was mitigated by an impedance control implemented for interaction. Results show that the redundant arm was manipulating while compensating for the movement of the helicopter. The experiment was carried outdoors and focused on the grasping of a pole by pulling it out of the fixed base. The average wind speed was 4 m/s. Low frequency oscillations of the arm coupled with the helicopter are cancelled by constraining the movement of the arm CoG in the lateral plane.

In 2014 Giglio and Pierri introduce their work on compliance control for aerial manipulation [35]. The proposed control scheme is characterised by three layers: the first layer includes a motion planner, which determines the desired motion for the actuated variables on the basis of the desired end-effector trajectory. The second layer has an impedance controller that confers a compliant behaviour to the system in the presence of forces and moments acting on the end-effector. Lastly a third layer implements a motion controller that tracks the references output of the above layer. The effectiveness of the approach is tested in simulation highlighting the benefits of the impedance filter.

Later that year, Orsag et al. propose a novel control strategy to tackle valve turning operations conducted by an aerial manipulator [36]. An integrated control scheme between the aircraft and dual-arm system is developed, where the main contributor is the yaw controller implemented on the aerial manipulator. A human-machine interface provides inputs to actuate the manipulator and guides the UAV through a coupling with the mock valve, then the turning operation is initiated. The results validate the kinematic and dynamic model, as well as the design of the human-machine interface. Key results display prolonged contact with the valve as well as different friction profiles of the grasp between the hand-tool and the valve surface.

During the same year, Fumagalli et al. developed an aerial manipulator for stable interaction with the environment [37]. The same Delta robot manipulator previously used is mounted on a quadrotor and safe interaction is investigated by means of a passivity-based controller. An additional functionality for the auto-tracking of the marker is illustrated: once the end-effector is aligned with the target, the controller aims at stabilising the gripper during contact-based operations. The maximum force applied during the experiment is 1.8 N.

A variable-impedance control applied to an aerial platform is proposed by Mersha et al., capable of adjusting the impedance of the multi-rotor and therefore improve the response to time-varying interaction forces [38]. This approach specifically focuses on safe and robust compensation of disturbances exerted by the environment, for example in case a human operator interferes with the manipulator by exerting an external force on it.

In 2015, Ruggiero et al. introduce a multi-layer architecture to control a UAV equipped with a servo robot arm [39]. At first, a novel mechanism is presented which implements a moving battery counterweight system to balance the statics of the robotic arm. Then, another layer takes care of the residual static effects of the arm within the thrust control. Lastly, an estimator of external forces and moments feeds back to the UAV's attitude

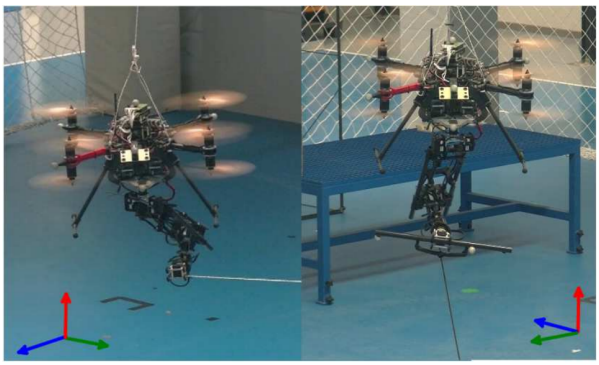

Figure 2.4: Impedance control for aerial interaction with a rope (left) and a semi-flexible bar (right). - [4]

controller to compensate neglected aerodynamic effects and the arm dynamics. Results show that the combination of the control layers benefits the performance of vehicle.

In 2016, Cataldi et al. present an impedance control scheme for aerial robotic manipulation with the aim of reducing the end-effector interaction forces with the environment [4]. The multi-level architecture proposed has an outer loop for the trajectory generator and impedance filter that modifies the trajectory to achieve a complaint behaviour at the end-effector. The middle loop is used to generate the joint space variables through an inverse kinematic algorithm. Lastly, the inner loop is aimed at ensuring the motion tracking. The proposed control architecture is tested experimentally where the end-effector holds a rope being pulled by a human operator, as illustrated in Figure 2.4. The impedance controller improves the vehicle stability in flight compared to a rigid controller.

2.4 The Introduction of Mechanical Compliance

In more recent years, new ways to tune the impedance of the system were introduced as part of the manipulator's design thanks to compliance. In 2015 the design of a lightweight compliant arm for aerial manipulation is presented by [40]. The mechanical design and construction of a 3-DoFs arm prototype (elbow pitch, wrist roll and pitch) is proposed where the addition of extension springs that resemble human ligaments is illustrated. Compliance in the forearm of the human-like manipulator is induced by the elongation/retraction of a series of springs while grasping an object. Such springs act like a muscle antagonist movement and, besides estimating the mass of the object carried, they also reduce the effect of contact forces propagated via the arm to the aerial base.

Once the mass of the object is estimated, the information is sent to the altitude controller of the vehicle for adjustments in the vertical configuration of the aircraft.

Figure 2.5: A UAV equipped with a passive, single-DoF manipulator features mechanical compliance for dynamic interaction with a vertical wall. [5]

In 2016 a work by Bartelds et al. addresses the problem of aerial dynamic physical interaction [5]. In this work, the analysis of colliding systems is presented with a novel solution to the problem of handling impacts using a passively compliant manipulator, see Figure 2.5. The decoupling of the manipulation system from the aerial base generates a faster dynamic response at the manipulator when handling collisions. The proposed design acts as a spring-damper system where the spring element is embodied by a rubber band mounted on a sliding rod; and the damping coefficient is embodied by a lock mechanism on the rod's displacement. The passive spring element converts the kinetic energy released during a collision into potential energy stored in the spring thanks to the elongation of the rubber band. The damper element is embodied by a locking mechanism which locks the tension spring in place and prevents the potential energy stored from being released. Results show that, while impacting in *rigid* mode the measured force at the end-effector reaches 54.2 N whereas in the *compliant* mode the force propagating to the aerial vehicle drops to 11.8 N, demonstrating that the impact forces are partially absorbed by the passive compliant system. Further work from the same author is presented in [41], where different control strategies for aerial manipulators handling highly dynamic physical interaction and aerial impacts are compared in simulation.

The effectiveness of compliance as a design parameter of the manipulator has been also demonstrated by Suarez et al. in [42] where a bio-inspired lightweight dual-arm featuring mechanical compliance allows for payload estimation and altitude dynamics compensation. Later in 2016 the same authors propose a compliant finger module [6]

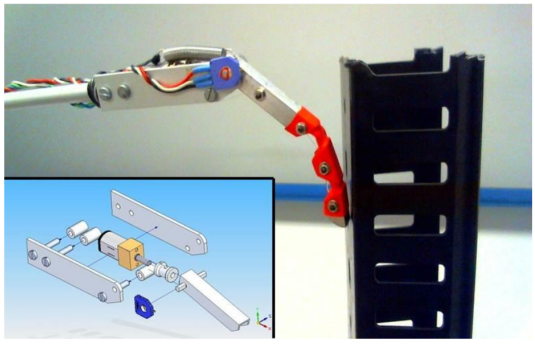

Figure 2.6: A compliant finger module for aerial manipulation. - [6]

attached at the end of the anthropomorphic arm as illustrated in Figure 2.6. The focus in this work is to estimate the joints' torques and contact forces based on the spring stroke and the joint's deflection as the finger module aids the obstacle detection. The performance of the compliant gripper module is measured on a fixed test bench.

In [43] a collision-resilient flying robot encapsulated within a protection case is proposed, enabling impact absorption thanks to its material properties. Similarly, in [44] a passive gimbal mounted on the surrounding structure transforms linear kinetic energy of impacts into rotational kinetic energy of the framing structure preserving the position of the UAV's Centre of Gravity (CoG) and absorbing collision induced disturbances.

In 2018, Suarez et al. present a work on virtual impedance control for the compliant dual arm system seen before, implemented for aerial manipulation [45]. To vary the apparent stiffness, damping or inertia of the compliant joints, the virtual impedance behaviour is developed based on the spring deflection in the joints. The impedance controller is defined in the Cartesian space and is aided by visual feedback from a camera which informs the controller loop of the joints relative position. The frequency response as well as the response to impacts is evaluated experimentally, together with the overall performance in a grasping operation conducted on a hexacopter. Key results demonstrate the potential of the impedance control approach for the compliant manipulator, with the main limitations brought by the slow response of the servo motors in the manipulator's joints.

2.5 Aerial Manipulation for Force-Based Tasks

Since the year 2017 aerial force exchange with the environment becomes the main focus of researchers in aerial manipulation. Up to this moment, results in aerial manipulation

mostly concern the validation of the UAV's flight controller for stabilisation in the altitude dynamics, and the validation of the manipulator's kinematic model and controller. At this stage in time, the state of the art in aerial manipulation had progressed and demonstrated stable control of each individual system independently, i.e. the UAV and the manipulator, as well as their integration in flight.

Force exchange has a key role in aerial manipulation for a multitude of tasks. Most tasks that involve physical interaction such as contact-based inspection or NDT require forces that are higher than 3 N, therefore new ways and methods to exert higher forces in-flight are introduced in the literature. Besides the interest to control the magnitude of the force, researchers have also proposed ways in which the period of application of such force, or the curve profile could be adjusted.

The first example is found in [46], where a novel approach to force exchange is introduced with the use of a tilt-rotor UAV. This system is able to apply a force over an inclined surface and be able to control independently both linear and angular accelerations of the UAV to counteract any opposing forces and moments resulting from an interaction. Although this method only allowed the application of 7 N force, the novel fully actuated UAV presents a very stable behaviour throughout the task. Within the mathematical model presented by the author, the forces and moments are grouped in a *wrench*, as a way to present the dynamics of the UAV more neatly. The term *wrench* borrows from the Screw-Theory, formally introduced by Sir Robert Stawell Ball and widely used in Robotics to describe the kinematics and dynamics of spatial rigid bodies [47].

Similarly to [46], in the work of Papachristos et al. [48] the exertion of large forces for object manipulation is achieved through the use of a direct thrust-vectoring actuation on a tilt-rotor, with resulting forces over 20 N. Along the same lines, the work proposed by [49] shows a hexarotor performing a peg-in-hole task using a 6-DoF manipulator inspired by a HEXA parallel robot. To generate a force on the interaction plane, i.e. X-Y plane of the aerial manipulator, the rotors' axes are tilted of a certain cant angle. This inclination distributes part of the aircraft thrust into a force normal to the wall for peg-in-hole purposes.

In late 2017 Takahiro et al. present the first successful contact operation outdoors for bridge inspection [50]. An octo-rotor UAV equipped with a 1-degree-of-freedom manipulator performs a preliminary experiment where the force applied by the aerial manipulator is proportional to the UAV's pitch when it comes in contact with the bridge pier. During contact, the UAV is able to exert a force at the end-effector over 10 seconds; with a mean error of 4.27 N against the 20 N desired force. The setup used in this

experiment consists of two laser rangefinders to measure altitude and planar position of the UAV with respect to the vertical wall; a single DoF manipulator with a force sensor mounted at the end-effector and four shock absorbers to stabilise contact after the collision.

In the same year, Wopereis et al. measured substantial forces up to 16 N applied by an aerial vehicle equipped with a passive manipulator pitching at high angles against a flat vertical surface [51]. This work mainly focuses on the control strategy over the pitch and yaw angles to guarantee stable contact for prolonged periods of time, with the main limitation lying in the assumption of a static contact point and limited end-effector motion due to its passive nature.

At the end of 2018 a work by [52, 53] shows a tricopter UAV equipped with an additional fourth propeller laying horizontally for physical interaction with the environment. The “boomcopter" utilises the horizontal propeller propulsion to apply forces while in hover state through a static end-effector. The scope for such design is the ability to position objects over flat vertical surfaces thanks to a press-to-release mechanism embedded in the end-effector., however no flight experiments are presented.

2.6 Conclusions

Based on the state of the art examined in this chapter, this study aims to address some of the challenges of aerial manipulation and proposes a novel lightweight compact manipulator tailored for contact-based interaction and the exertion of force on the side of the UAV.

Multiple works in the field demonstrated how the introduction of mechanical compliance [5, 42, 54] or compliant control [4, 28, 30, 35, 38, 39] is highly beneficial for the interaction carried out by floating platforms as UAVs. Compliance can in fact bring a benefit towards the overall aircraft stability and also alleviate some of the disturbances propagated by the end-effector to the aerial vehicle.

The work proposed in this thesis takes inspiration from the above and exploits the use of compliance in different ways to aerial facilitate force exchange. The ability to use a variable-stiffness variable-damping manipulation system will also be evaluated for the exertion of forces in the environment and the interaction with different targets. Having an adaptively compliant aerial manipulator can extend the range of applications that can be pursued, offering a higher flexibility in its uses. Compliance will therefore be proposed in different forms throughout this thesis.

The importance of having a *smart* body design that works in synergy with the control strategy is also something that is highlighted in this thesis. Similarly to the approach taken in the works [40, 42], the aerial manipulator's performance is examined from the design perspective. The analysis and experimental validation carried out in this work are tightly connected to the design considerations and assumptions to create an effective manipulator, tailored to force-driven aerial tasks. A focus on how the morphology of the manipulator can favour the mechanics resulting from aerial interaction is therefore a recurring theme in this work, as well as one of the objectives of this thesis.

The following chapters also investigate the use of well established interaction control methods within novel applications in aerial robotics. The main goal is to assess whether such control strategies used in combination with the proposed design and on-board sensing, represent a viable approach for aerial physical interaction and force exchange by an aerial robot.

Only a few works can be found in the literature that tackle the exertion of forces higher than 5 N with UAVs [46, 48, 51]. This is because research in aerial manipulation has only reached a higher level of maturity in the past two to three years. In this thesis the exertion of considerable forces is tackled in multiple ways through the combined action of the active manipulator and the vehicle's thrust, or by using the vehicle's own inertia. Once again, this type of approach highlights the importance of exploiting each subsystem's characteristics to accomplish the mission's objectives, as opposed to limiting the refinement to a single element.

Lastly, this work introduces novel application scenarios for the validation of each *design and control* approach. As often found in the literature, manipulators are deployed for grasping of objects from the ground, or for object transportation/handling. Very few examples display the use of aerial manipulators for side intervention with a wall [37, 50, 53, 55]. Tackling side interaction brings additional challenges on the control perspective, as the aircraft is subject to asymmetrical forces and moments which may lead to instability. Within chapters 4 to 6, three different scenarios will be evaluated where sideways interaction is examined within realistic conditions.

CHAPTER 3

AERIAL ROBOTS FOR PHYSICAL INTERACTION: MODELING AND DESIGN

Publications

This chapter has resulted in the following peer-reviewed research output:

1. Hamaza, S., Georgilas, I., and Richardson, T. (2018, July). An adaptive-compliance manipulator for contact-based aerial applications. In *2018 IEEE/ASME International Conference on Advanced Intelligent Mechatronics (AIM)* (pp. 730-735). IEEE. [56]

Aerial manipulation is a relatively novel topic in the robotics community, which received a major boost in the recent years thanks to the latest developments in motion planning, navigation, sensing and battery capacity for aerial vehicles. One of the key challenges of aerial interaction is the ability to cope with external disturbances caused by the exchange of forces and moments with the environment. Being a mobile and floating platform, a UAV is less able to counteract disturbances induced by contact with an object compared to a grounded robot. Even more so in the case of UAMs, for which the applications require the vehicle to hover in the proximity of obstacles and walls, where flying capabilities and aerodynamics are most affected.

With regards to the manipulation system for the UAV, the previous chapter showed how in the later stages of the state of the art researchers moved towards multi-DoFs manipulators to allow a higher degree of versatility and adaptability of the robotic platform. Robotic manipulators can be categorised in two classes, *serial* and *parallel*. Serial manipulators are found commonly in the industrial sector, they are designed as a series of links connected by actuated joints that extend from the base to the end-effector, often resembling a human-arm-like configuration. Parallel robots on the contrary are formed by several kinematic chains which share the same base and the same end-effector. In aerial manipulation, the choice for a manipulation system on-board usually falls on serial type of manipulators. These manipulators are often selected amongst off-the-shelf industrial solutions [12, 34, 57, 58], or they can be custom-made single or dual arm systems consisting of multiple servo motors in series that mimic the range of motion of a human arm [25, 32, 36, 40, 42, 59].

Another trend found in the literature is to add compliance through *software* implementation rather than through *hardware*. Compliance aids the interaction between two rigid bodies by providing a smooth transfer of the input force and displacement from one body to the other. Such property is beneficial as it assures safer interaction between the rigid systems. In the state of the art of aerial manipulation, only a few works highlight the benefits of introducing mechanical compliance as part of the manipulator design to aid the aerial task [5, 40, 54]. The author of this thesis contributed to the work in [5] published within the first year of this PhD, which was awarded *Best Paper in Robotics and Automation Letters (RA-L)* during the flagship *IEEE International Conference on Robotics and Automation (ICRA)* in 2017. In this work the benefits of adding mechanical compliance to the aerial manipulator are highlighted by comparing the vehicle's response in the case of a rigid/stiff interaction with a wall, as opposed to a compliant interaction.

Following the findings in aerial manipulation, the work described in this chapter addresses the modelling of aerial interaction and investigates the crucial design parameters that affect the vehicle's stability and performance in flight. In the following sections, the vectors' dynamics of the system are evaluated in a simulation environment to study aerial interaction with a vertical wall. The analysis and the simulation results are then used to extrapolate the key design parameters for the manipulator that will drive the design stage. Hence, the design of a bespoke manipulator is addressed: the proposed solution consists of a compact and lightweight design featuring mechanical compliance within a 2-DoFs system.

3.1 Aerial Manipulator Dynamics

In this section, the mathematical description of the system is briefly presented. The aerial manipulator is modelled as a multi-rotor platform carrying an external load. The aerial system's dynamics have been studied in the literature extensively in these works: [2, 15, 24, 33, 60–62]. In this section, the equations of motions of the aerial manipulator are presented considering the two systems as separate, therefore providing the generalised equations of motion of the aerial system and the manipulator's dynamic equations.

3.1.1 Aerial Vehicle Model

A generic aerial system with n-rotors is considered, i.e. a 6-DoFs rigid body. Two coordinate frames are then identified: the world frame $\mathcal{W}$ and the body-fixed frame $\mathcal{A}$ centred in the vehicle CoG. The pose of the moving body with respect to the world frame is described by the vector $\mathbf{p} = [\zeta_x\ \zeta_y\ \zeta_z\ \phi_R\ \theta_P\ \psi_Y]^T$ comprising of translational and rotational terms. The equation of motion of the system is:

$$\mathbf{M}\ddot{\mathbf{p}} + \mathbf{C}(\mathbf{p}, \dot{\mathbf{p}})\dot{\mathbf{p}} + \mathbf{G}(\mathbf{p}) = \tau + \tau_{\mathbf{man}} \tag{3.1}$$

where $\mathbf{M}$ is the mass matrix with all inertial terms of the system, $\mathbf{C}$ is a skew-symmetric matrix with centripetal and Coriolis terms, $\mathbf{G}$ represents the gravitational terms acting on the system. On the right side, τ represents the output torque and thrust force generated by the vehicle's rotors; $\tau_{\mathbf{man}} = [\mathbf{F_m}\ \mathbf{M_m}]^T$ is the vector of external forces and moments induced on the vehicle by the manipulator.

3.1.2 Manipulator Model

The aim is to understand how the terms $\mathbf{F_m}$ and $\mathbf{T_m}$ affect the aerial vehicle's dynamics during interaction. To start with, the manipulator is modeled as a load directly attached to the vehicle. The coordinate frame $\mathcal{M}$ is centred in the manipulator's CoG. Such frame moves relatively with the manipulator's while performing a task, and this motion is independent of the aircraft motion. Similarly as before, the position and orientation of frame $\mathcal{M}$ with respect to frame $\mathcal{A}$ can be described with vector $\mathbf{p_m} = [\zeta_{mx}\ \zeta_{my}\ \zeta_{mz}\ \phi_{mR}\ \theta_{mP}\ \psi_{mY}]^T$. The manipulator's equation of motion is:

$$\mathbf{M}\ddot{\mathbf{p}}_\mathbf{m} + \mathbf{C}(\mathbf{p_m}, \dot{\mathbf{p}}_\mathbf{m})\dot{\mathbf{p}}_\mathbf{m} + \mathbf{G}(\mathbf{p_m}) = \sigma_{\mathbf{ext}} \tag{3.2}$$

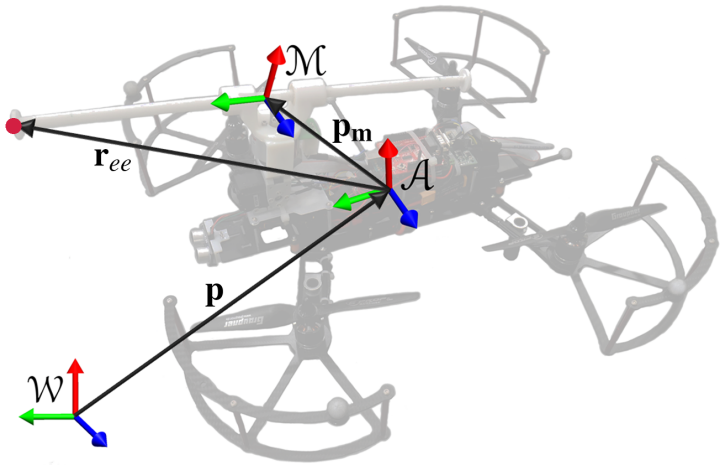

Figure 3.1: Aerial manipulator sketch and coordinate frames.

where $\mathbf{M}$ is the mass matrix of the system, $\mathbf{C}$ is the damping matrix with centripetal and Coriolis terms and $\mathbf{G}$ is the matrix describing the gravitational terms. For the equilibrium, this equates to the sum of all external forces and moments acting on the manipulator σ_{ext}, for example the external actions due to interaction. It is to be noted that Equation (3.2) solely describes the manipulator dynamics and does not consider the dynamic effects of the aerial vehicle (see Equation (3.1)).

Now, let us define vector $\mathbf{r}_{ee} = [x_{ee}\ y_{ee}\ z_{ee}]^T$ that links the origin of frame $\mathcal{A}$ to the tip of the end-effector, as illustrated in Figure 3.1. The external forces and moments acting on the vehicle caused by the interaction of the end-effector with the environment, expressed in frame $\mathcal{A}$ are:

$$\sigma_{ext} = \begin{bmatrix} \mathbf{R}_M^A\ \mathbf{F}_{int} \\ \mathbf{r}_{ee} \times \mathbf{R}_M^A\ \mathbf{F}_{int} + \mathbf{R}_M^A\ \mathbf{M}_{int} \end{bmatrix} \tag{3.3}$$

where $\mathbf{F}_{int}$ and $\mathbf{M}_{int}$ represent the interaction force and moment respectively, and $\mathbf{R}_M^A$ is the rotation matrix from frame $\mathcal{A}$ to frame $\mathcal{M}$.

The above equation shows the external moments and forces resulting from the interaction with an object. To be able to minimise such forces and moments and therefore minimise the disturbances on the flying vehicle, the terms $\mathbf{F}_{int}$ and $\mathbf{M}_{int}$ and $\mathbf{r}_{ee}$ need to be addressed. Starting from the force $\mathbf{F}_{int}$ and moment $\mathbf{M}_{int}$, a way to implicitly minimise these quantities can be achieved by minimising the propagation of such quantities to the aerial platform through the use of compliance. Vector $\mathbf{r}_{ee}$ can also be minimised within the design process, therefore bringing a more favourable response in the vehicle and reducing the induced momentum. There parameters become the three key drivers for the design a manipulation system that:

- is able to absorb/filter the undesired forces exerted at the end-effector and mitigate the propagation of those to the aircraft with the use of actively-variable compliance;
- has a small-sized end-effector in order to reduce the contact surface to a single point, therefore reducing/zeroing the moment $\mathbf{M}_{int}$;
- can adjust vector $\mathbf{r}_{ee}$ by moving the end-effector location independently and minimise the cross-product in Equation (3.3)

3.2 Design Considerations

In general, the approach found in the literature when it comes to designing a manipulator for aerial robotics applications is to use serial manipulators with n-joints providing n-DoFs. As previously discussed, these type of manipulators offer greater dexterity and versatility in the number of tasks that can be accomplished, with respect to lower DoFs manipulators. However, they bring drawbacks in terms of higher weight that the vehicle needs to carry and balance, higher inertia, shorter flight time and often lower manoeuvrability. Hence, it is important to understand the trade off between versatility and performance, along with the task requirements. Overall, it is advisable to limit the weight where possible and avoid redundancy whilst still devising the right tool for the job. For contact-based tasks that require the exertion of a force normal to a surface, e.g. NDT or contact inspection, a simple probe oriented towards the target surface provides a compact, weight-efficient solution to the problem.

The distribution of masses both statically and dynamically is to be taken into consideration. In reference to Equation (3.2), the inertial term $M(q)$ and damping $C(q,\dot{q})$ contribute dynamically as a function of position and velocity, whereas vector G leads to a static contribution. This is so because the UAV's motion is affected by the presence of the manipulator due to gravitational effect. The overall mass of the system, including the aircraft and the manipulator, $\bar{m}$ and inertia $\bar{I}$ is given by:

$$\begin{cases} \bar{m} & = m_a + m_m \\ \bar{I} & = I_a + I_m + m_m \|r\|^2 \end{cases} \tag{3.4}$$

Where r is the position vector linking the manipulator's CoG to the aircraft CoG, and subscripts a and m stand for *aircraft* and *manipulator* respectively. By minimising the magnitude of r and keeping a compact design, the UAV's angular stability is improved and the induced momentum is reduced (see $\|r\|^2$).

Besides the static instability due to gravitational components, the manipulator generates dynamic disturbances as well due to its internal motion, i.e. $M(q)\ddot{q} + C(q,\dot{q})\dot{q}$, that can be minimised by reducing moving masses. Moreover, to generate a more dynamically balanced flying system it is advisable to have symmetry on the vehicle so to centre the manipulator CoG as close as possible to the aircraft CoG.

Now, by looking again at Equation (3.3) it can be noticed how minimising vector $\mathbf{r}_{EE}$ has a positive effect on the momentum induced by the interaction. Thus, it becomes a crucial design parameter for a manipulation system that is tailored to force-based interaction. Further discussion on this will follow in the next section.

Lastly, as previously seen the state of the art on aerial manipulation shows that impedance or passivity-based type of controllers and mechanical compliance are highly beneficial for the overall system, making the interaction safer and more robust.

3.3 Simulation

The type of interaction studied is a *side* interaction, where the aerial manipulator approaches a vertical wall at a non-zero velocity and pushes against it. For the analysis, the underlying assumptions discussed in the previous section and the design considerations highlighted above are evaluated in the Simulink® environment. The goal of the simulation study is to investigate whether different configurations of the manipulator have an effect on the aerial system's dynamics, and whether the disturbances generated during interaction can be partially dissipated or absorbed by the manipulator itself.

3.3.1 Model Requirements

Looking at Equation (3.3), the momentum generated by the interaction force F_{int} is the cross product between the end-effector position with respect to the CoG, and the contact force. Such force is directed opposite to the UAV velocity thus, minimising the induced moment is equivalent to:

$$min \left| \frac{r_{EE}}{\|r_{EE}\|} - \frac{v}{\|v\|} \right| \tag{3.5}$$

In other words, the end-effector should be ideally positioned in such way that the contact point and the UAV's CoG are aligned, as shown in Figure 3.2. However, as it is often not feasible to recreate such configuration due to hardware constraints, the effects of multiple end-effector's configurations on the aircraft will be studied and simulated.

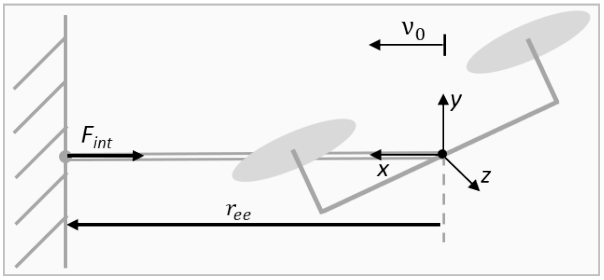

Figure 3.2: Ideal location of the contact point during interaction, which minimises the induced moment.

In order to minimise the propagation of disturbances from the environment to the aerial platform, the introduction of a spring-damping system as part of the manipulator is here evaluated. Introducing compliance as part of the design allows for a safer interaction, but also it filters out undesired disturbances [5, 40, 48, 54]. Damping is also essential to prevent the aircraft from bouncing on the target surface following an impact. Firstly, let us consider the system's energy conservation during collision: the manipulator exchanges translational kinetic energy E_t and rotational E_r, but also potential energy V with the environment. The following equation holds:

$$\frac{d}{dt}\Big(E_t + E_r + V\Big) = 0 \tag{3.6}$$

As stated before, the objective is to minimise the induced angular momentum on the aerial platform, thus yielding to a null change of rotational energy over time, $dE_r/dt \approx 0$. Hence, the linear kinetic energy could be rewritten as:

$$\frac{d}{dt}E_t = -\frac{d}{dt}V \tag{3.7}$$

The equation above implies that, ideally, if the manipulator could behave as a pure storage element, i.e. a mechanical spring, it could convert the total kinetic energy of the impact into potential energy. This further validates the need for a spring-like tool for energy storage, but also for a damper to dissipate such potential energy. To tackle this, a system with variable stiffness and variable damping is proposed; and different stiffness K and damping C coefficients are tested.

3.3.2 Model Description

The environment chosen for simulations is Simulink®, with the use of the SimMechanics® library to recreate a model of aerial interaction with an underactuated platform, i.e. a

quadrotor, carrying a 2-DoFs manipulator. It is assumed that the interaction takes place with a straight surface, e.g. a rigid wall, and no lateral forces, e.g. gusts, act on the aerial manipulator other than the interaction force. Thus, the type of interaction is planar.

The UAV is actuated so to move on the plane of interaction, starting from a hover state. Its motion is translational along x-y and rotational about the z axis. At time t_0 the aircraft moves forwards towards the obstacle in the x axis direction with a constant velocity $v_0 = 0.27m/s$ and with given pitch angle α_{attack}. The manipulator consist of a revolute joint actuated by a servo motor, and a passive slider joint for translational motion of the end-effector. The slider has pivot on the servo motor, to allow independent pitch of the end-effector. Variable compliance is modelled by means of a spring-damper mechanism where both the stiffness and damping coefficients are actively changed. The spring-damper mechanism guides the elastic behaviour of the prismatic joint.

The interaction between the two objects, i.e. the aerial manipulator and the obstacle, is recreated by means of a translational hard-stop constraint: the UAV is free to move along the x direction until the hard-stop bound is met and contact is established. This type of block is frequently used in SimMechanics to emulate collision of objects falling on the ground. Similarly the UAV is able to move forward with the given speed v_0 until the conditions of the hard-stop apply, then it is forced to stop. The obstacle object is modelled as a rectangular body with high stiffness and damping, e.g. a rigid wall.

To generate a realistic model, the geometry, inertia and mass properties of the actuator on-board reflect those of commercial components. Likewise the aircraft model mimics the properties of commercially available quadrotors.

Figure 3.3 displays an intuitive representation of the system as a whole. The manipulator's pitch motion is decoupled from the vehicle's thanks to the presence of the active revolute joint (orange circle labelled R). Within the spring-damper system, a prismatic joint (labelled P) controls the spring's stroke, i.e. the end-effector relative position. The wall is modelled as a fixed constraint with *infinite* stiffness K_{wall}.

In Figure 3.4, the model built in the Simulink environment is illustrated. The blue blocks represent the aerial manipulator, consisting of the UAV and the manipulator. The aerial platform on its own consists of several blocks where the geometry of a general quadrotor has been recreated. Motion constraints are imposed throughout all components using different types of joints: prismatic, revolute, weld, planar. Initial conditions on the aircraft and the manipulator are also given within the blocks named IC.

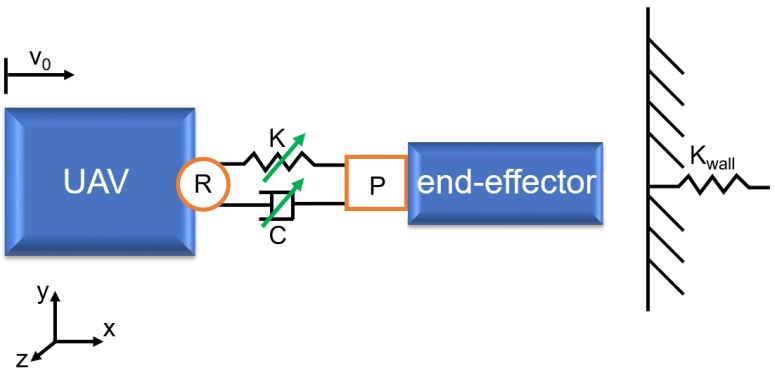

Figure 3.3: Schematic of the planar model built in Simulink displaying the relevant model parameters.

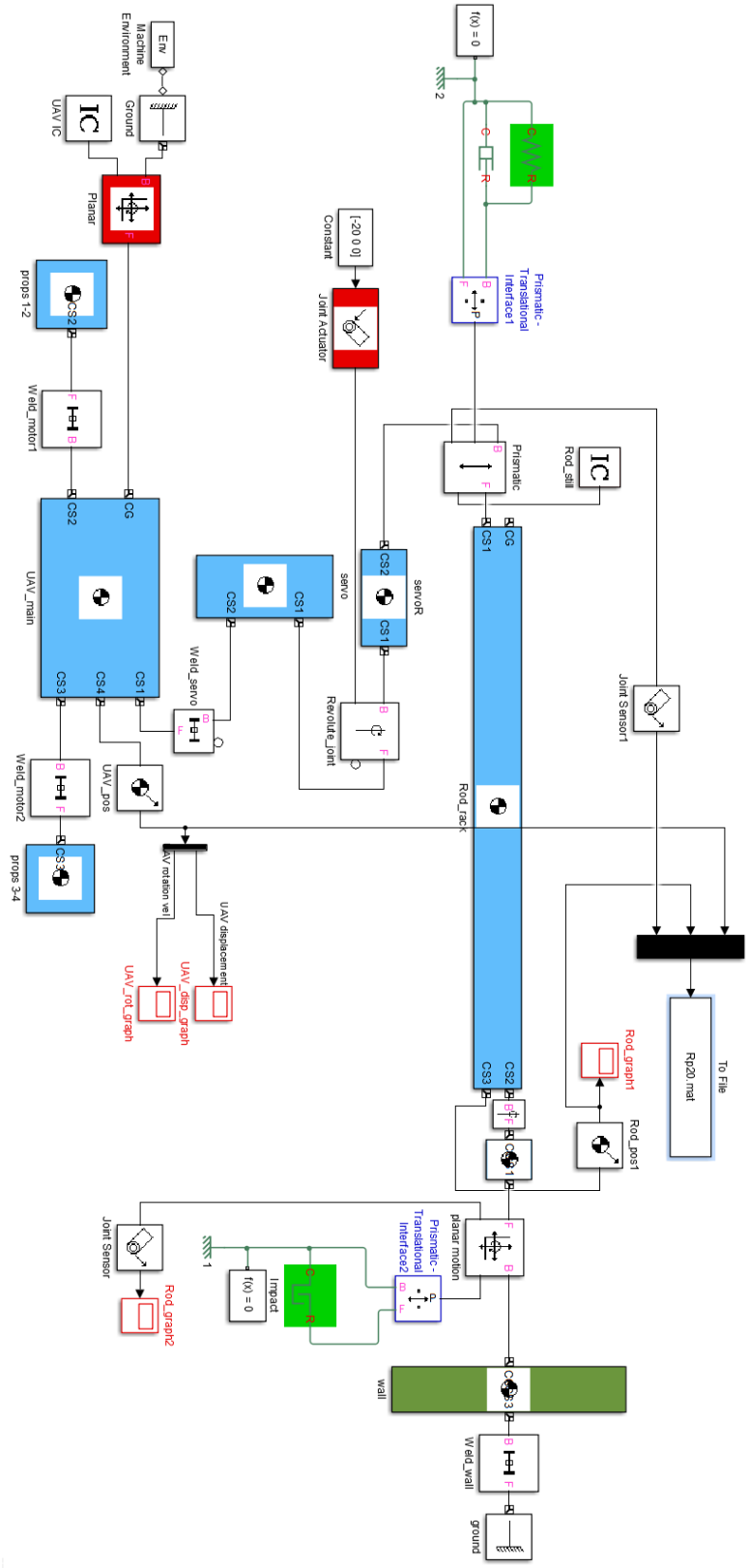

Figure 3.4: Overview of the Simulink block diagram.

3.3.3 Simulation Results

In figure Figure 3.5 the angular displacement θ about the z axis, and the interaction torque $\mathbf{T}_{int}$ measured at the origin of frame $\mathcal{A}$ are illustrated. Both parameters display the effects of a different manipulator configuration on the aircraft CoG. The horizontal component $r_{ee,x}$ is chosen so to protrude outside the propellers physical boundaries and avoid interference with the rotors.

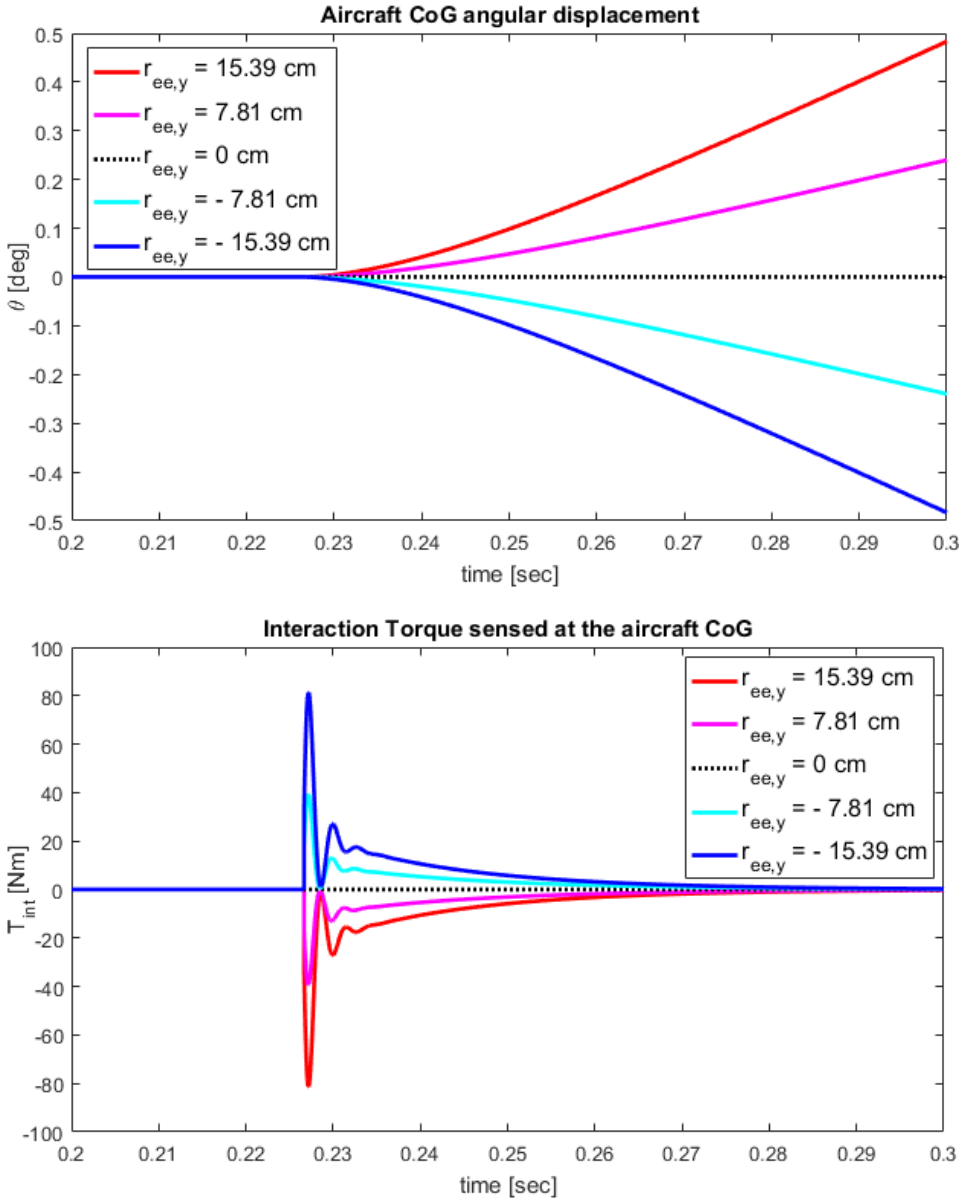

Figure 3.5: The angular displacement and the torque due to interaction are measured on the aircraft CoG in different end-effector configurations. In particular the effects of the sign and magnitude of vector $r_{ee,y}$ are demonstrated over the torque $\mathbf{T}_{int}$.

The vertical component $r_{ee,y}$ is examined in three different scenarios: a positive $r_{ee,y}$ places the end-effector above the aircraft CoG, a negative $r_{ee,y}$ places it below its CoG and a null component makes the end-effector vertically aligned with the aircraft CoG.

As the tip of the end-effector moves along the vertical axis, the peak moment $\mathbf{T}_{int}$ is proportional to the magnitude of $r_{ee,y}$. Moreover, $\mathbf{T}_{int}$ has direction dependent on the sign of $r_{ee,y}$. A positive torque generates clockwise when $r_{ee,y} > 0$, viceversa it is anti-clockwise with $r_{ee,y} < 0$, and null when the end-effector is vertically aligned with the aircraft CoG. This concept is illustrated in Figure 3.6.

The angular displacement θ increases exponentially after the collision takes place (at $t \approx 0.23$ sec), and reaches about $\pm$ 20° at t = 2.5 sec (outside figure boundaries).

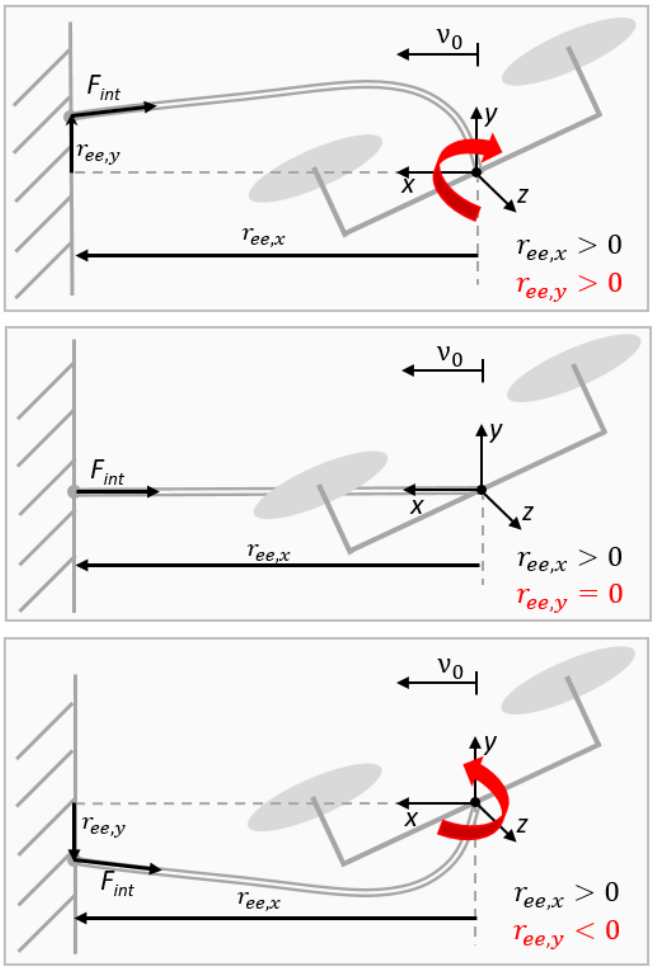

Figure 3.6: Schematic drawing of a UAV equipped with a generic manipulator. As the end-effector protrudes out, the contact point can fall in three possible locations. Depending on where the contact point is, the vertical component of vector r_{ee} changes, namely $r_{ee,y}$. This affects the magnitude and direction of the moment induced by $\mathbf{F}_{int}$.

For the sake of these initial simulation tests, the vehicle's flight controller is not implemented in the Simulink model, hence the force induced by the collision with the wall causes an *infinite* motion in the opposite direction. In fact, the vehicle in this model behaves as a passive friction-less body, unable to counteract external disturbances. In reality though, the flight controller would respond to external disturbances in an attempt to regain stability, and its motion in space would eventually cease.

In Figure 3.7 the interaction forces measured at the end-effector and at the UAV's

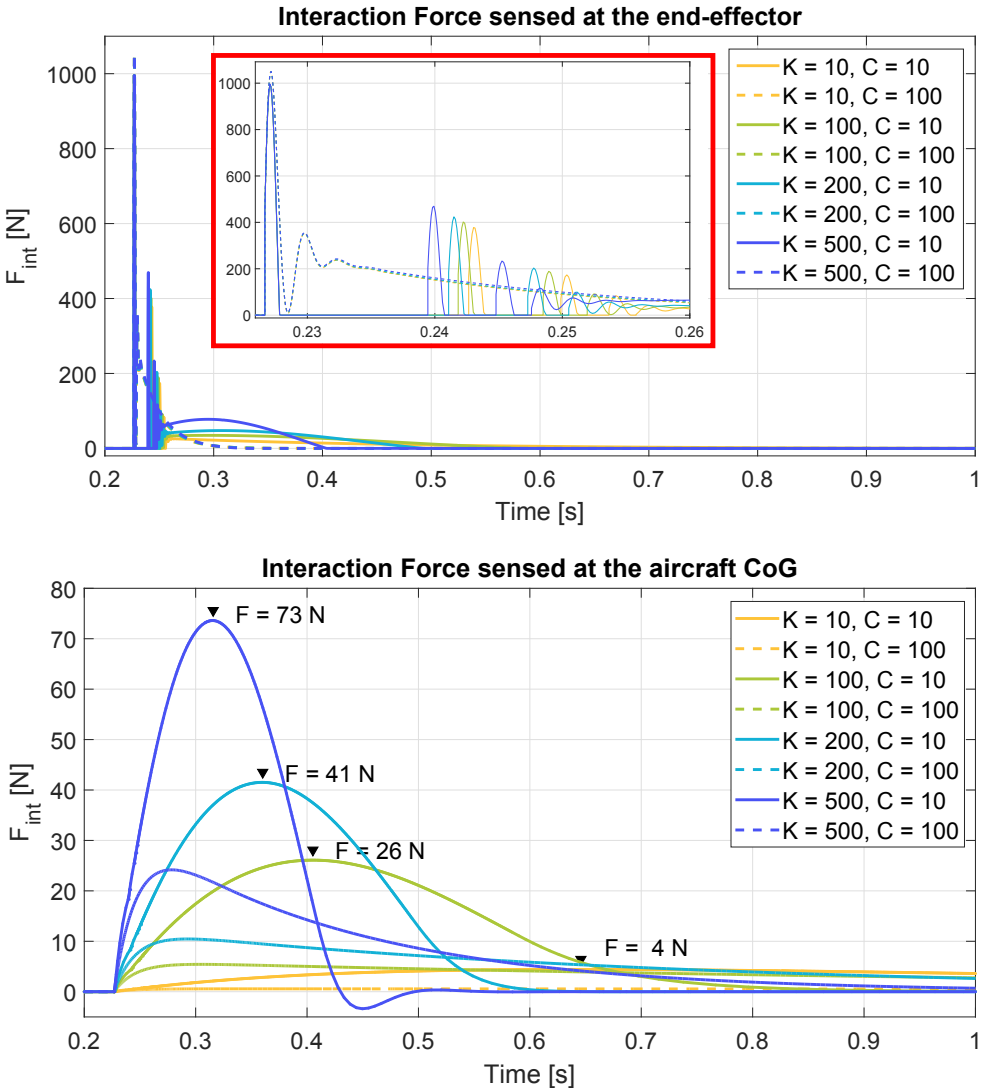

Figure 3.7: A comparison of different stiffness K [Nm] and damping coefficients C [N/(m/s)] of the active spring-damper system. The interaction force is measured at two key locations: the end-effector (top figure) and the aircraft CoG (bottom figure). The response is substantially different due to the presence of compliance in the manipulator.

CoG are illustrated. Both figures show the effects of varying the stiffness K [Nm] and damping coefficient C [N/(m/s)] of the linear actuator on the forces profile. The following conclusions are drawn:

- the presence of a spring-damper element on the manipulator mitigates the forces experienced by the UAV CoG in magnitude, frequency and in the exponential decay;
- low stiffness values K produce forces that are lower in magnitude (yellow lines) and have a wider span over time, as opposed to high stiffness values (blue lines);
- higher values of damping coefficients C (dashed lines) are preferred over low values of C (solid lines) as damping dissipates the impact energy and causes the force to slowly decay over time.

From this analysis it can be inferred that the presence of spring-damper system as part of the manipulator's design is a key element that allows to partially absorbs the interaction forces, prevents the vehicle from bouncing, and damps the propagated disturbances over time. Moreover, the possibility to adjust such stiffness and damping parameters through variable compliance offers a higher versatility in terms of shaping the output forces and dynamic behaviour of the aerial system during the interaction with different target objects. Lastly, the location of the end-effector also represents a crucial design variable that can minimise the induced moments and benefit the aerial system's stability.

3.4 Manipulation System Design

Within the objectives of this thesis features the design of a lightweight compliant manipulator that is tailored at aerial contact inspection and other force-driven tasks that require low dexterity. The proposed system consists of 2 active DoFs, one translational and one rotational. The former is embodied by a prismatic joint, which is actuated by a brushless DC motor driving a rack and pinion transmission. Although the use of a passive slider was initially contemplated as a tool with which the UAV could have interacted with the environment, an active solution was preferred to maintain control over the end-effector position and the force output. The rotational DoF is provided by a servo motor which allows for independent pitching of the end-effector, irrespective of the aircraft. The overall mechanism design is illustrated in Figure 3.8.

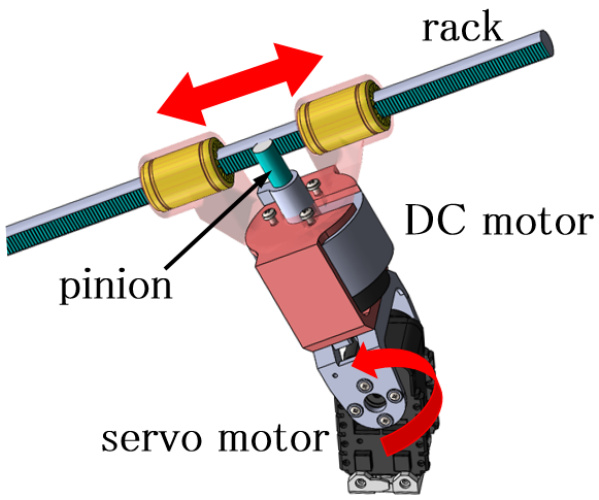

Figure 3.8: Manipulator's mechanical design: a servo motor drives the pitching of the end-effector; translational motion is given by a rack-and-pinion transmission driven by a DC motor. As the DC motor spins, the pinion moves the rack housed inside two linear bearings (in yellow). Thanks to the backdrivable motor, the rack's motion is bidirectional.

The ability of the manipulator to tackle different stiffness K and damping C coefficients, and act as a variable compliance tool is implemented within the prismatic joint itself. This will be discussed in detail in the following chapter.

3.4.1 Mechanical Components

The selection of mechanical components breaks down to the rack and pinion, 2 linear bearings and the housing. Starting with the rack, this mechanical component is a standard solution in industry for power transmission, often available is various materials and shapes. Typically, the wide majority of racks available on the market have a square profile rather than tubular. The tubular design is preferred as it avoids the use of linear guides throughout the entire length, i.e. rack sliders, and replaces them with simple and lightweight bearings. In this way, the volume required on the vehicle to house the slider is significantly reduced, as well as the mass. Therefore, the selection narrowed down to a custom-made round racks in Delrin® (plastic) material, outer diameter of 10 mm, 0.5 tooth modulus, 400 mm length and 40 g in mass.

The selected rack has to withstand the loads incurred during interaction, therefore the structural integrity of this component is something to verify. In particular, two types of validation are carried out: the admissible *buckling force*, and the maximum allowed force on the tooth. Using Euler's critical load formula for slender structures [63] yields

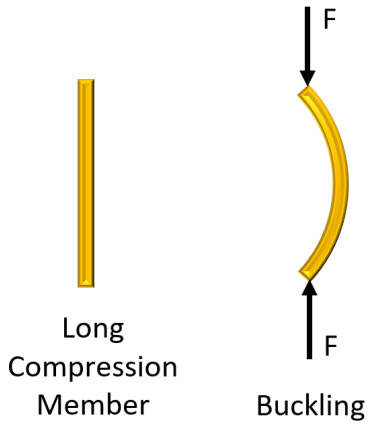

Figure 3.9: Buckling on slender profiles.

to:

$$F_{buckling} = \frac{\pi^2 EI}{(KL)^2} \tag{3.8}$$

where F is the maximum allowed compression force along the beam, E is the modulus of elasticity, I is the smallest second moment of area [m^4] of the cross section of the beam, K is the beam effective length factor, and L is the beam unsupported length. Substituting each parameter as in Table 3.1, leads to $F_{buckling}$ = 290.17 N.

Young's modulus E [GPa] @ 20°C	Moment of area $I = \pi r^4/4$ [m^4]	Effective length factor K	Beam unsupported length L [m]
2.7	4.9×10^{-10}	0.7071	0.3

Table 3.1: Mechanical properties for analysis on buckling load.

From the literature [5], the peak force sensed during a rigid impact of an aerial platform against a vertical wall is 54.2 N (averaged over a number of flight tests), which drops down to 11.8 N when compliance is added to the manipulator. It is assumed that an impact generated by an aerial vehicle of similar mass properties as the one seen in the above reference will generate a force below 100 N, which is below the buckling limit for a rack with the selected geometry and material.

Now follows the validation of the admissible force on the tooth, to prevent the gearing from breakage during the transmission of such impact force. Using Lewis formula [63], the equation treats the tooth as a simple cantilever, with tooth contact occurring at the

tip. The overall Lewis stress should be less than the admissible yield stress, $\sigma_{LW} < \sigma_{yield}$.

$$\sigma_{LW} = \frac{W_t P}{F y} \tag{3.9}$$

where W_t is the tangential tooth load, P is the pitch diameter, F is the face width of the tooth and y is the Lewis a-dimensional form factor. Considering an impact force of 100 N acting tangentially (no normal component, brings to the worse case scenario) yields to:

$$\sigma_{LW} = 147.57 \text{ Pa} \qquad \sigma_{yield} = 97 \text{ MPa} \qquad \text{hence} \qquad \sigma_{LW} << \sigma_{yield}$$

Tangential tooth load W_t [N]	Pitch diameter P [mm]	Tooth face width F [mm]	Lewis factor y
100	5	7	0.484

Table 3.2: Mechanical properties for the study on maximum tooth load.

The above shows that the flexural stress acting on the tooth is within the admissible yield tensile stress for Delrin material.

The choice for the pinion that drives the rack is restricted by the same tooth modulus of 0.5; while the material was chosen to be stainless steel. The incongruence between the two materials in the transmission is not ideal, as the steel teeth of the pinion tend to wear off the plastic ones on the rack more easily on the long run. However, this was a conscious choice as the metal pinion provided a better coupling and engagement with the tooth than its plastic counterpart. Another reason behind this choice is the fact that, thanks to its compact size, the extra weight accounted for the metal pinion was overall still acceptable. The pinion is mounted on the motor shaft via a shaft coupling.

Two igus® linear bearings are selected to guarantee accurate alignment between the rack and the pinion, serving the double function of improving the coupling in the transmission, and releasing the pinion from any radial load that might generate. Such igus® bearings are lightweight, lubrication-free linear guides made out of corrosion-free materials, i.e. high performance polymers, and are used as a sliding surface. Each bearing weighs 7 g. Finally, the housing for the overall mechanism is 3D-printed in ABS material, with a wall thickness of 4 mm. For an overview on all hardware components, please refer to Table 3.3 at the end of the following section.

For the initial design stage, no specific gripper design is hereby proposed. The design of the hand-tool follows the application's requirements and it is considered on a case-specific basis. Examples of potential gripper designs could include the housing for a small

object/sensor that needs installing, or a nozzle to spray insulation material, or a textured fingertip to provide tactile feedback over a surface, or a marker pen holder, and so on.

3.4.2 Sensing

The manipulator is equipped with 2 sensors: an inductive Maxon MILE (Maxon's Inductive Little Encoder) quadrature encoder on the motor, and an ultrasonic distance sensor located at the front of the aircraft.

The encoder is directly coupled with the motor and measures the end-effector's relative position. The readings from the encoder are sent to the motor driver via a Quadrature Encoder Interface (QEI), then converted to metric measurements and updated in the manipulator control block. Knowing the position of the slider joint and its relative displacement results in more accurate positioning over the end-effector, and guarantees to operate within the rack's physical boundaries.

The proximity sensor is mounted at the front of the vehicle and informs the manipulator's on-board computer of the relative position between the UAV and the obstacle ahead. The selected sensor is a commercially available ultrasonic sensor to measure the relative distance between the aerial vehicle and the object ahead.

3.4.3 Electronics

The selection of the electronics for the manipulator includes two motors, the motor controller boards, and a dedicated on-board computer.

Starting with the actuator of the slider joint, amongst the requirements for the motor driving the pinion-rack mechanism are a high nominal and stall torque, backdrivability, and a high sampling frequency for fast response time. As the motor needs to react *instantaneously* to possible impacts, a high stall torque guarantees a safe operation and provides a safe upper bound for short periods of time, e.g. 3 seconds. The backdrivable feature allows motion in both directions: "receiving" force as an input from the environment, and generating output force. The selected motor is a Maxon® brushless DC motor with 780 mNm stall torque and Hall sensor, weighing 150 g.

The servo motor selected is a Robotis Dynamixel AX12A, with stall torque of 1.5 Nm, and real-time position feedback. This motor is often selected for robotics applications thanks to its high accuracy, robust position control and high torques, therefore offering a good compromise between cost and mechanical properties.

The motor driver board is a custom-made board offering position and current control modes of operation, in a compact and lightweight design. The communication protocols available on the motor board are of type CAN. The on-board computer that communicates with the DC motor, servo motor and the proximity sensor is an Arduino UNO board with CAN-Bus shield and logging capabilities. All mechanical and electronic components are listed in Table 3.3.

Table 3.3: Table with information on all components.

Image	Model	Specs.
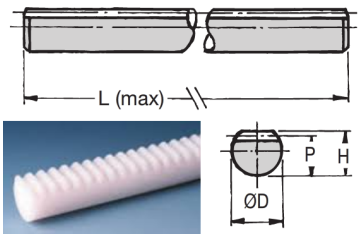	• Manufacturer: HPC Gears • Material: White Delrin • Part number: ZTR0.5	• MOD=0.5 • P=8.70, ⌀=10, H=9.20, L=400 [mm] • Weight = 40 g
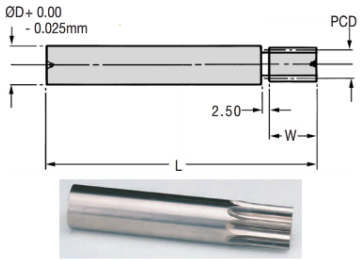	• Manufacturer: HPC Gears • Material: Stainless steel 303S21 • Part number: SP0.5-9	• MOD=0.5, Teeth=9 • PCD=5, ⌀=8, W=5, L=35 [mm] • Weight = 22 g
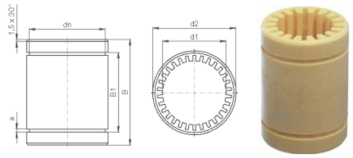	• Manufacturer: Igus • Material: Iglidur® J solid polymer • Part number: RJM-01-10	• $\varnothing_{inner}$=10 [mm] • Quantity=2 • Weight = 7 g
	• Manufacturer: Arduino • Part name: Arduino UNO	• Microcontroller: ATmega328P • Operating Voltage 5V • Digital I/O Pins 14 • Clock Speed 16 MHz • Weight = 25 g

Image	Model	Specs.
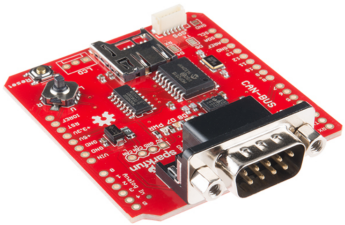	• Manufacturer: Sparkfun • Part number: CAN-BUS Shield	• CAN v2.0B up to 1 Mb/s • High speed SPI Interface (10 MHz) • CAN connection via standard 9-way sub-D connector • Micro SD card holder • Connector for serial LCD • Weight = 50 g
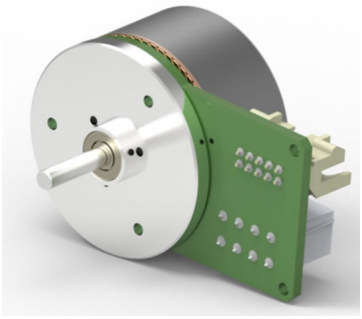	• Manufacturer: Maxon Motors • Part number, motor: EC 45 flat ⌀42.8 mm, brushless, 50 Watt, with Hall sensors	• Nominal voltage 24 V • No load speed 6710 rpm • No load current 185 mA • Nominal speed 5240 rpm • Nominal torque (max. continuous torque) 83.4 mNm • Nominal current (max. continuous current) 2.33 A • Stall torque 780 mNm • Stall current 23.3 A • Max. speed 10000 rpm • Max. axial load (dynamic) 3.8 N • Max. radial load 20 N, 5 mm from flange • Weight = 150 g

Image	Model	Specs.
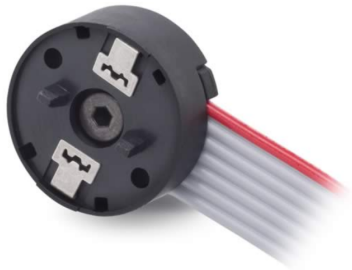	• Manufacturer: Maxon Motors • Part number, sensor: Encoder MR, Type M, 32 Counts per turn, 2 Channels	• Counts per turn 32 • Number of channels 2 • Max. mechanical speed 15000 rpm • Weight = 15 g
	• Manufacturer: Robotis • Part number: Dynamixel AX-12	• Nominal voltage: 9 - 12 V • Stall Torque: 1.5 Nm • No load speed: 59 rpm • Running Degree: 0° - 300° • Data Rate: up to 1Mbps • Weight = 53.5 g
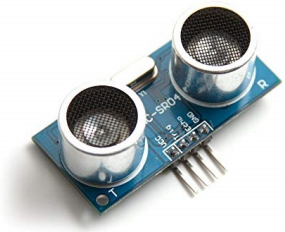	• Manufacturer: Shanhai • Part number: HC-SR04	• Nominal voltage: 5 V • Working Frequency: 40Hz • Range: 2cm - 4 m • Weight = 5 g

3.5 Integration with the Aerial Platform

The choice of a suitable platform for force-driven aerial applications was mainly constrained by two factors: the vehicle's available payload, and the available flight time at the maximum payload. In the case of the proposed manipulator the total mass of all mechanical and electronic components reaches 500 g, allowing the user to select a smaller sized platform that is safer to interact with, easier to fly and less costly to maintain and repair in case of failure.

Commercially available aerial platforms were preferred over customised solutions.

This is to support the idea that aerial manipulation technologies should be made more accessible to end-users, therefore validating the proposed manipulator as an add-on tool for already existing platforms. Moreover, the modular design gives end-users more freedom in terms of selecting the platform that is most suited to their needs, and the versatility to switch from UAV to UAM applications on the go.

The proposed 2-DoF manipulator design is manufactured and it is integrated on the Lumenier® QAV400 quadcopter (950 g) powered by a 4s 4000 mAh battery (330 g). The on-board flight controller is the Eagle Tree Vector FPV Controller, which allows attitude, position, and way-point flying modes. The platform itself came in a *ready-to-fly* solution, fully built and tuned. The vehicle was paired with a FrSky Taranis X9D radio transmitter, and interfaced with the ArduPilot Mission Planner ground control software. Four custom-made propeller guards in carbon fibre material (130 g) were designed and manufactured for this platform to conduct experiments more safely and prevent damages to the exposed propellers.

The platform's available payload was evaluated in a weight allocation experiment, which consisted in gradually increasing the mass of the quadcopter by added weights. Two modes of flying were performed: "normal" manoeuvring where the UAV was manually piloted to fly at a constant speed inside a flight arena; and "aggressive" manoeuvring where the pilot would impose rough changes in the quadcopter's direction or throttle, and

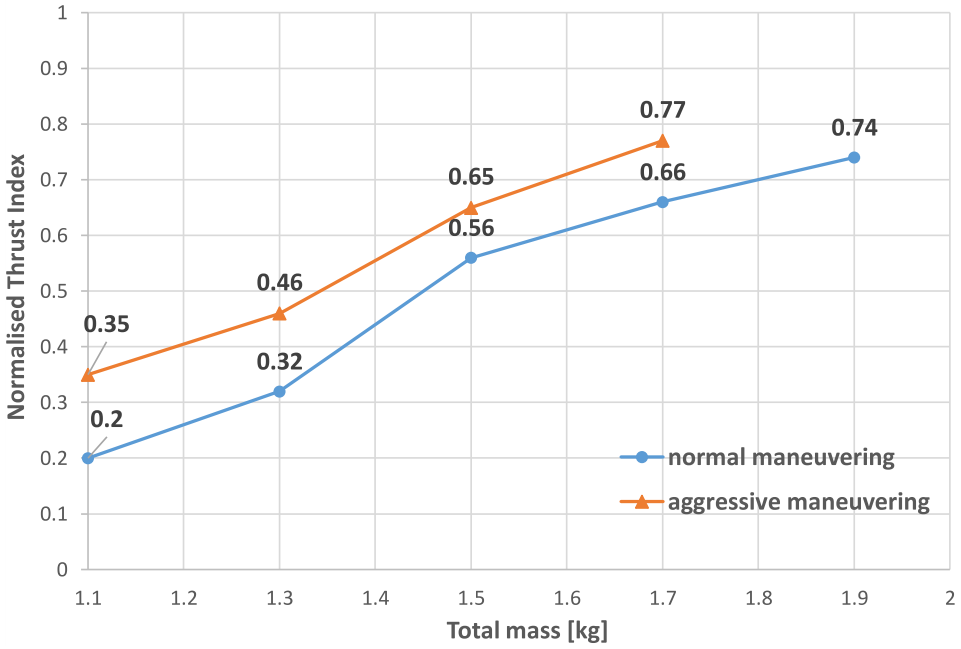

Figure 3.10: Weight allocation experiment on the QAV400 platform.

jerky movements. Results of this experiment can be seen in Figure 3.10. To fly within the safe limits and avoid overloading the rotors, it was assumed that the normalised rotors' thrust, i.e. the thrust capacity of the vehicle normalised in the scale $[0, 1]$, should not exceed 80% of the total. This parameter becomes an index of how reliably and safely the platform can fly with the increased payload. From the experiments, it was found that the total thrust in normal manoeuvring was 74%, with a total mass of 1.9 kg. This demonstrated that the QAV400 can fly with the envisioned payload of 500 g, powered by a 4000 mAh battery.

3.5.1 Aerial Manipulator Configuration and Architecture

The first step towards the integration of the manipulation system on the aerial vehicle is deciding where to place all the components. The selected quadrotor QAV400 has its core structure made out of 3 aluminium plates that house the flight controller and the wiring safely. Such structure makes the mounting of the manipulator possible on both the top and bottom plate.

As previously seen, the general rule when it comes to add masses on the aircraft is to position them as close as possible to the CoG to reduce the aerial system's inertia. However, it is often not feasible to centre the manipulator on the vehicle's CoG due to hardware constraints. In this case, the "top" configuration is preferred as it generates a more *favourable* vehicle response. As the UAM is in contact with a vertical surface on the side of the vehicle, the horizontal component of the rotors thrust is greater or equivalent to zero depending whether the vehicle is tilted forward or is hovering respectively. During interaction, if the resultant force from interaction is lesser than the thrust horizontal component, the UAV will not sense any disturbance as the summation of the two vectors will result in a force still directed towards the wall. However, if the interaction force is higher than the thrust horizontal component, the UAV condition will change as an effect.

To better understand the type of response that can be induced on the vehicle by such force, let us consider the point of application of such interaction force with respect to the vehicle's CoG. If the location of the end-effector, therefore the point of application of the force, is above the vehicle CoG, the response induced will generate a momentum on the aircraft that is anti-clockwise, causing the UAV to back off the wall. On the other hand if the point of contact was to be below the vehicle's CoG, the induced momentum would be clockwise, causing the aircraft to tilt towards the wall, potentially leading to collision.

Another reason why the top configuration was chosen relates to hardware constraints. In fact, the available space on the bottom plate is limited, and dependent on the geometry

of the landing gear. This places additional constraints to both the volume and range of motion available to the manipulator. Therefore, the “top" configuration is favoured.

The manipulator’s components (hardware, electronics and sensing) are placed in such a way that the weight is distributed symmetrically with respect to the vehicle’s CoG. In this respect, the prismatic joint is mounted towards the front of the aircraft, while the battery is placed at the back to balance out the weight. Figure 3.11 illustrates some computer-aided design (CAD) drawings of the UAM from different views and the hardware layout.

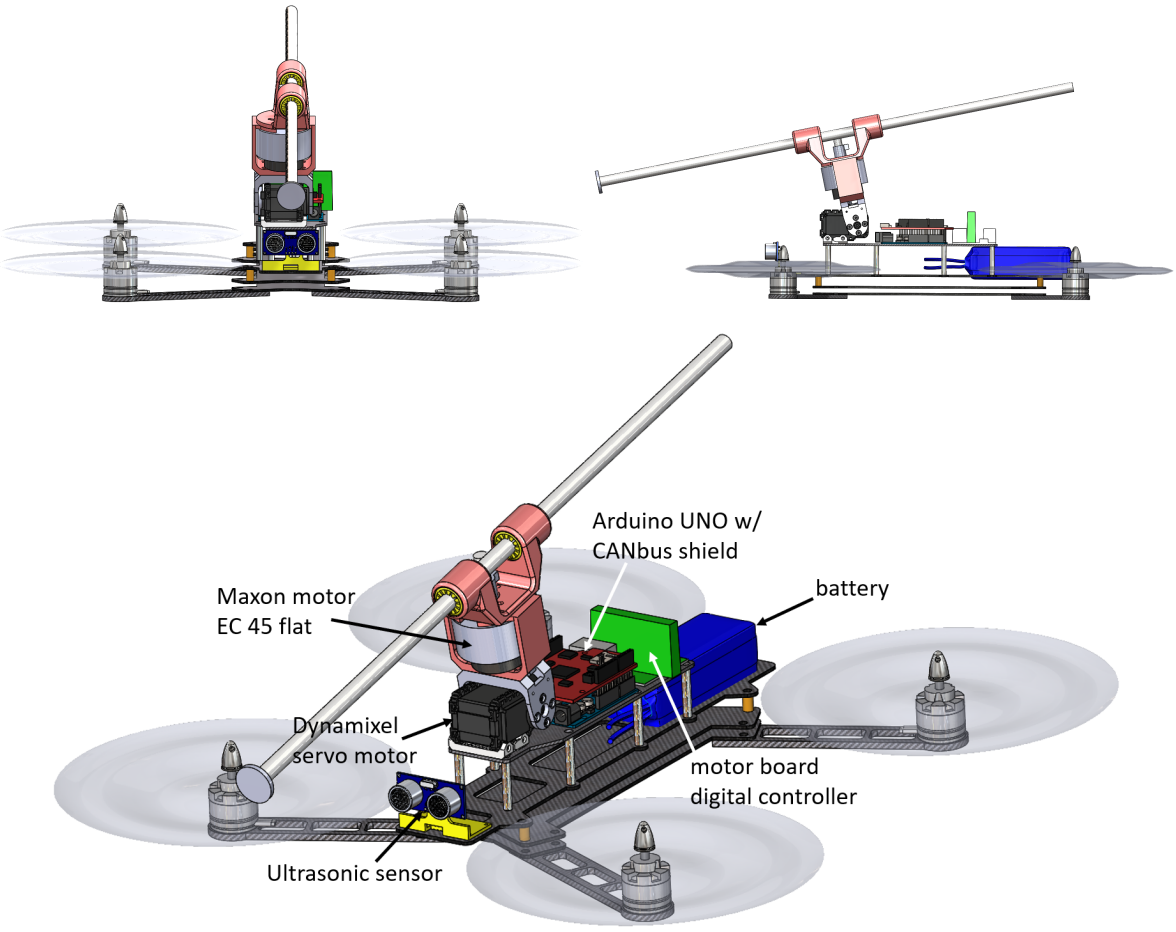

Figure 3.11: CAD drawings of the overall aerial system and components layout. ** The colours chosen in this representation are not necessarily true to reality.

3.6 Conclusions

In this chapter, aerial robotic interaction is analysed with the use of vector dynamics: the modelling is presented and discussed, highlighting the key design parameters for a manipulation system that facilitates aerial interaction. The mathematical assumptions and the design considerations derived are then channelled in a simulation study for planar interaction of an aerial system equipped with compact manipulator on-board. Results from the simulation study demonstrate the validity of the model and the benefits of compliance as a feature of the manipulator. Follows the design stage for a novel, 2-DoF manipulator tailored at force-driven tasks that require limited dexterity. Lastly, the integration on the aerial platform is detailed, where preliminary flights are conducted to verify the payload limits of the aerial system.

Differently from what is found in the state-of-the-art of aerial manipulation, this chapter presents a novel, design-driven analysis that aims to extrapolate useful design features for an aerial system interacting with a vertical surface. The analysis is addressed towards the creation of a bespoke manipulator where the *body* of the aerial system as whole can play a major role in aiding aerial interaction, in synergy with the intelligence/control laws. This is a novel approach to aerial manipulation where the main contribution lies in the attempt of offloading the computation from the brain (control) to the body, thorough the proposition of a smart, tailored design.

Future chapters will further expand on the design process and tailor the manipulator for different aerial tasks. Other control approaches will also be evaluated for compliant force-exchange with different targeted environments.

CHAPTER 4

AN AERIAL MANIPULATOR WITH VARIABLE COMPLIANCE FOR PUSHING AND TAPPING TASKS

Publications

This chapter has resulted in the following peer-reviewed research outputs:

1. Hamaza, S., Georgilas, I. and Richardson, T., 2018, October. Towards An Adaptive-Compliance Aerial Manipulator for Contact-Based Interaction. In *2018 IEEE/RSJ International Conference on Intelligent Robots and Systems (IROS)* (pp. 1-9). IEEE. [64]

Aerial tasks that involve the exchange of forces in the environment on the side of the aerial manipulator as opposed to grasping an object from the ground have been only addressed in a few works in the literature. Side interaction on an aerial system introduces more challenges as the forces and moments induced on the aircraft CoG are asymmetrical and can easily lead to instability. Key works in the state of the art show the application of up to 5 N in quasi-static conditions [1, 31, 37, 46]. In 2017, a simple one-DoF aerial manipulator was used to perform wall contact on a bridge outdoors, showing that the force applied by the octo-rotor UAV is proportional to its pitch angle [50]. The conversion from the rotors' horizontal thrust component to the demanded

interaction force is handled by the manipulator, with the help of direct force feedback on the end-effector.

The benefits of introducing compliance as part of the manipulation system have been demonstrated both in the *hardware* and *software* side. As previously highlighted in chapter 2, compliance has been implemented as part of the aerial maipulator's design with the addition of soft materials [5], or collision-resilient structures encapsulating the UAV [43, 44], or with the use of mechanical springs [40, 54].

With regards to compliance implemented in software, several contributions in the state of the art demonstrate how *compliant* control aids force estimation and motion feedback at the end-effector, improving stable contact during an interaction [4, 30, 35, 65, 66].

The work described in this chapter demonstrates how the proposed 2-DoF aerial manipulator featuring active variable-compliance is able to tackle some of the challenges of aerial dynamical interaction. To show the effectiveness of the design and the benefits brought by a variable-gain PID controller, two different tasks are tackled by the aerial manipulator: pushing and tapping against a vertical wall. The ability to perform such tasks can be exploited in a variety of contexts such as aerial object placement on a vertical surface, aerial surveying by contact with the exertion of different force profiles, the excitation of an object/area through a series of physical pulses for inspection, maintenance or cleaning purposes.

Thus, two main contributions are hereby presented: the control approach used to recreate a variable-compliance manipulation system where the ability to adjust the force

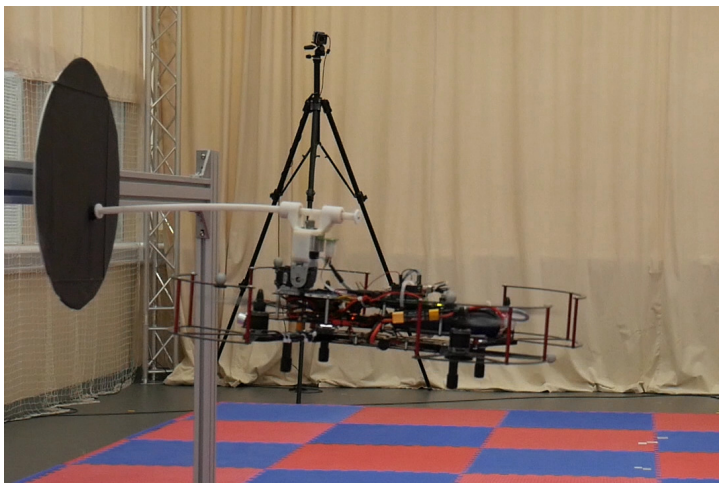

Figure 4.1: A quadrotor equipped with an adaptively-compliant manipulator interacting with a vertical surface.

output can be used, and the ability to shape the loads applied over a vertical surface, e.g. a single pulse for longer periods of time, or a rapid series of shorter pulses.

4.1 Manipulation System Control

In this section, the ability for the manipulator to behave as a variable-impedance tool is addressed.

The analogy between Proportional Integral Derivative controller (PID) and a spring-damper system is exploited to achieve a variable-stiffness behaviour on the slider joint and respond to external forces in a compliant way. To understand this analogy, the following example is presented. Cars have spring-damper mechanisms as part of their suspension system on each of their wheels. The spring element is in duty of keeping the car a certain distance above the ground, just like the proportional term of a PD controller. The variable that is controlled on the suspension system is the stroke of the spring, while in a PD controller it is the error in the set-point variable the one to minimise. Shock absorbers on a car damp the vehicle's vibrations generated from the suspension system, likewise the derivative portion of a PD controller damps the oscillations and prevents overshooting.

In the case of PID controllers the proportional gain K_P provides the rack with a spring-like behaviour, the derivative gain K_D generates a damped motor's response and the integral gain K_I is in charge of driving the steady-state error to zero. The choice of having a PID controller over a standard PD is to allow the integral gain K_i to overcome the system's static friction. In fact, below a certain PWM threshold, the power output sent by a standard Proportional Derivative (PD) controller could not overcome the static friction of the brushless DC motor and of the transmission components. Hence, the choice for PID over PD allowed a quicker steady state response even at lower power inputs.

To generate a spring-like behaviour on the translational joint, the motor driving the pinion will mimic a torsional spring. Torsional springs are types of springs that store energy in a twisting, rotational motion. In order to store potential energy, the spring must be twisted as a result of a pulling or pushing force. In the case of the rack-and-pinion transmission, the pinion (spring element) is loaded by the twisting motion imposed by the movement in the rack: as an external force causes the rack to slide, translational motion converts into rotational at the pinion. At this stage the motor is forced to move away from the reference and an error in position generates. In order to minimise this error the motor will respond with a torque increase in the opposite direction, releasing

the energy stored in the spring.

Both the torque and current outputted by the motor increase proportionally with the positioning error, causing the rack to respond in a more forceful way in the opposite direction. In this way, the motor will correct any sensed error induced by the end-effector, and respond by counterbalancing the opposing force. In Figure 4.2, the analogy between PD controllers and spring-damper systems is illustrated, where the controller is represented as a virtual spring-damper that corrects the error between the actual position x, and the reference x_{ref}.

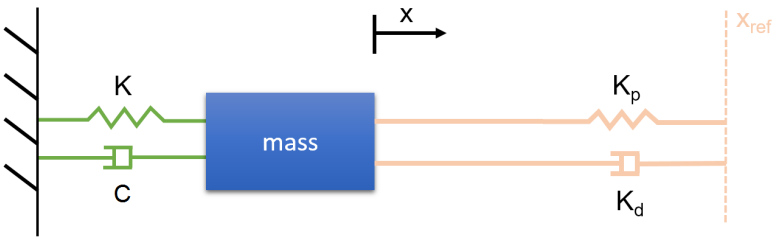

Figure 4.2: Analogy between a spring-damper system and a PD controller.

To tune the PID gains on the DC brushless motor, the Ziegler-Nichols' rule is applied [67]. The tuning method consisted in starting with a simple Proportional controller, with a low/zero value of gain K_p. After the gain K_p is gradually increased, the steady-state oscillation is reached. This critical proportional gain is noted as K_{cr}, with period of oscillation T_{cr}. In Table 4.1 the values obtained to tune the PID controller are listed, where T_i and T_d represent the integral and the derivative time constants respectively. Computing the gains leads to $K_i = 213.33$ and $K_d = 0.027$.

Table 4.1: Ziegler-Nichols parameters for PID controller.

K_{cr}	T_{cr}	$K_p = 0.6K_{cr}$	$T_i = 0.5T_{cr}$	$T_d = 0.125T_{cr}$
8	0.045	4.8	2.25×10^{-2}	5.63×10^{-3}

So far, a way to mimic a spring-damper system on a rack-and-pinion mechanism through software is proposed. However, what is more interesting to see is whether different stiffness and damping coefficients have an effect on the aerial manipulator's behaviour and dynamic response. In essence, the goal is to check the effectiveness of various stiffness K and damping C coefficients on a real aerial prototype. This is implemented through the tuning of the controller gains, K_p and K_d.

The ability to adjust the compliance of the manipulation system will result in different behaviours, and tackle different aerial applications. What is expected is that

lower gains will generate a more compliant response to the forces exerted/absorbed by the end-effector and a less aggressive performance in general; while higher gains will create a stiffer response. The former configuration, i.e. lower gains, can be useful in a scenario where the vehicle approaches the wall at a high speed with the risk of possible collisions, or to respond to sudden disturbances that require the manipulator to absorb any undesired impact/kinetic energy. On the other hand, higher gains will produce a more rigid behaviour and greater output forces at the end-effector to tackle, for example, a placement task. In essence, adjusting the manipulator's gains will change the mechanical impedance of the end-effector and its dynamic response to forces received and outputted. This provides us with a *adaptively* compliant tool for aerial contact-based applications.

4.2 Experiments

In this section the initial flight tests carried out to validate the proposed aerial manipulator are presented. Over 60 airborne experiments were conducted to demonstrate both the effect of *adaptive* compliance and the ability to perform force-based tasks, such as pushing against, or tapping a surface.

Amongst the challenges faced in the experiments there is the ability to tackle aerial physical interaction with a more dynamic approach than the one found in the literature: instead of hovering in the proximity of the target, the UAM approaches it at a constant speed. Therefore, the ability to exploit variable compliance to absorb the kinetic energy produced during impact is a key factor, as failing this may lead to potential damage of the platform.

Another challenge faced is the ability to exert different force outputs at the end-effector while the UAV is in close proximity with the target obstacle, it being more prone to disturbances. Lastly, another challenge is related to the ability of the UAV to counteract the interaction force and hold its position while the manipulator is in contact with the target. This is particularly difficult to achieve during the *Tapping Task* experiments, where for each time the end-effector establishes contact with the surface, a motion backwards is induced on the UAV. To be able to complete the tapping for several cycles, the disturbances propagating to the aerial system need to be damped and smoothed by the manipulator's compliance.

4.2.1 Experimental Setup

The platform used in the experimental validation is the previously presented Lumenier QAV400® quadcopter (950 g) powered by a 4s 4000mAh battery (330 g). The manipulator overall mass is about 550 g; the aircraft all-up weight is about 1.9 kg including the front propeller guards. A VICON motion capture system is used to acquire ground truth measurements of the aerial system. A 6-axis Force/Torque sensor (FTSens, IIT, Italy) is mounted on the wall where the interaction takes place and measures the contact force. The force sensor is controlled by an external Arduino UNO® board with logging capabilities.

It is to be noted that the sensor's measurements are used as ground truth measurements and they are not fed back in the manipulator's controller. This was due to the fact that the aircraft had already saturated the available payload in this configuration and could not account for additional weight. Therefore, the sensor was used as a validation tool rather than a loop-closure element. Force sensing on-board however will be addressed as part of the manipulator's refinement in the following chapters.

4.2.2 Pushing Task

The first scenario addresses the application of force on a vertical wall. Recalling the gains found through Ziegler-Nichols' method: $K_p = 4.8$, $K_i = 213.33$ and $K_d = 0.027$. To adjust the active spring-damper system one can intervene on the proportional and derivative gains. In this instance, as the gain K_d is in the order of 10^{-2}, it was decided to discard the tuning of such: being K_d already low in value, it would not be possible to appreciate differences in the damping by changing its value. Therefore, the following experiments focus in the effects deriving from changes in the proportional gain only.

Four different proportional gains were selected to validate the variable-compliance behaviour of the aerial manipulator. The gains were selected at 10%, 20%, 50%, and 60% of the ultimate value K_{cr}, respectively $K_p = 0.8$, 1.6, 4 and 4.8. For each of these gains, between 12 to 15 flight experiments have been conducted. All gains tested are within the safe limit found through Ziegler-Nichols ($K_p \leq 4.8$, see Table 4.1). Over 50 flights in total demonstrate the ability for the proposed UAM to push against a vertical surface with different compliant settings.

4.2.2.1 Experiment Outline

Each experiment is laid out as follows: the aircraft flies through a series of way-points allowing it to reach the target location at a constant speed of 0.25 m/s and perform the interaction task. The dataset generated at each flight can be staged as follows: *approaching the target, interaction phase, recovery / settling phase, homing*.

For each flight, the interaction effects on the UAV's dynamic response are measured through the CoG position *x-y-z* and orientation *roll-pitch-yaw* angles, tracked by the VICON system. The forces exerted on the wall are also measured by the Force/Torque sensor.

4.2.2.2 Results

Table 4.2 summarises the effect of adaptive compliance on the UAV's angular dynamics measured over multiple data-sets. The mean value μ, standard deviation σ and peak amplitude of the UAV *roll*, *pitch* and *yaw* angles are presented, averaged over all flights conducted with the same compliant condition, i.e. the same K_p value. To extrapolate the trend of the angular dynamics due to the interaction, μ and σ are computed considering the *interaction* and *recovery / settling* phases in the dataset, discarding the *homing* and *target approaching* stages.

	K_p = 0.8	K_p = 1.6	K_p = 4	K_p = 4.8
$\mu_{roll} \pm \sigma_{roll}$	0.36 ± 0.81	0.29 ± 1.00	0.31 ± 1.09	0.72 ± 1.30
peak amplitude$_{roll}$	2.25	2.39	2.47	2.46
$\mu_{pitch} \pm \sigma_{pitch}$	0.70 ± 3.45	0.73 ± 3.76	0.75 ± 4.16	0.73 ± 4.24
peak amplitude$_{pitch}$	9.37	10.63	11.24	17.30
$\mu_{yaw} \pm \sigma_{yaw}$	-0.57 ± 1.77	-0.05 ± 1.95	-0.64 ± 2.06	-0.84 ± 2.89
peak amplitude$_{yaw}$	0.09	0.17	1.16	0.59

Table 4.2: Mean value μ [deg], standard deviation σ [deg] and peak amplitude [deg] of the UAV angular states (roll, pitch, yaw) measured by the VICON tracking system and averaged over a minimum of 10 flights for each K_p.

Looking at the table, the first consideration that can be made relates to the higher values in the standard deviations compared to the mean values in all angles; more noticeably in the pitch angle. This shows that, within the time period considered in the experiment, the change in the variable is big, but instantaneous. Prior the contact with the surface, the aerial system angles aren't affected and stay close to zero as the aircraft is in hover state. At the moment of contact, a sudden change in the angles is imposed instantaneously, causing the angular profile to spike and oscillate until convergence to zero is reached again after settlement. This is more noticeable in the pitch angle, as the pitch plane is the plane where the interaction takes place.

Secondly, it can be noticed that by increasing the stiffness of the manipulator, i.e. higher proportional gains in the PID control, the standard deviation σ increases indicating that more fluctuations are present on the aircraft CoG, therefore higher disturbances propagate to the aircraft. In particular, the pitch state is the one mostly affected during the interaction (see σ_{pitch} and peak amplitude$_{pitch}$ in Table 4.2). A comparison between the peak amplitude$_{pitch}$ in the first and last column of the table shows an outcome that is almost doubled in magnitude, leading to a peak amplitude up to 17 degrees. Figure 4.3 provides a side-view on the aircraft interacting with the wall. This time-lapse sequence

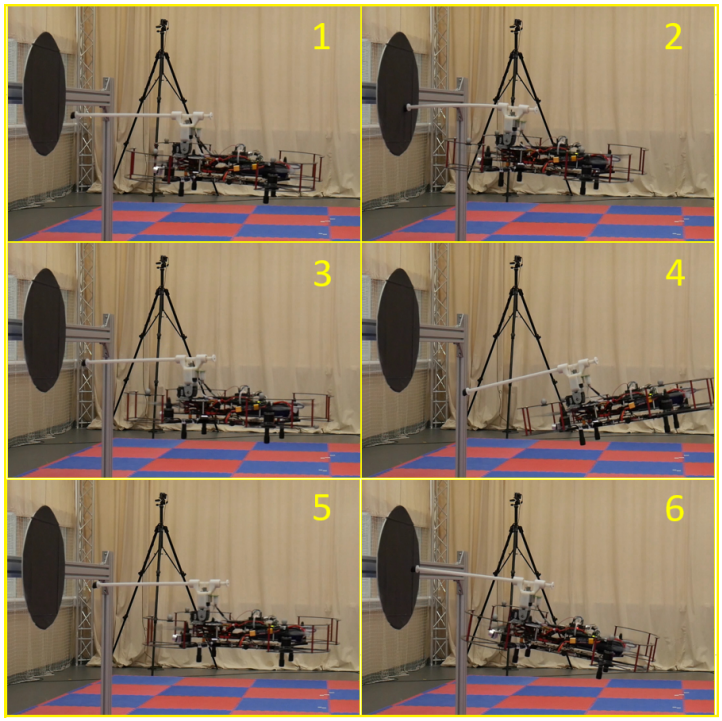

Figure 4.3: A time lapse sequence of aerial interaction with a wall, captured during a single flight with K_p = 4.8.

was recorded during a single flight with K_p = 4.8 and clearly shows how the vehicle's oscillatory behaviour in pitch after the task has been completed.

The information on disturbances about the x-z axes, namely changes in *roll-yaw* angles, is also displayed in the table. It can be inferred that higher compliance is beneficial to the UAV's angular dynamics in different ways: despite an increase in the σ_{yaw} of about +1 degree, the peak amplitude of both roll and yaw angles are consistently low throughout the table.

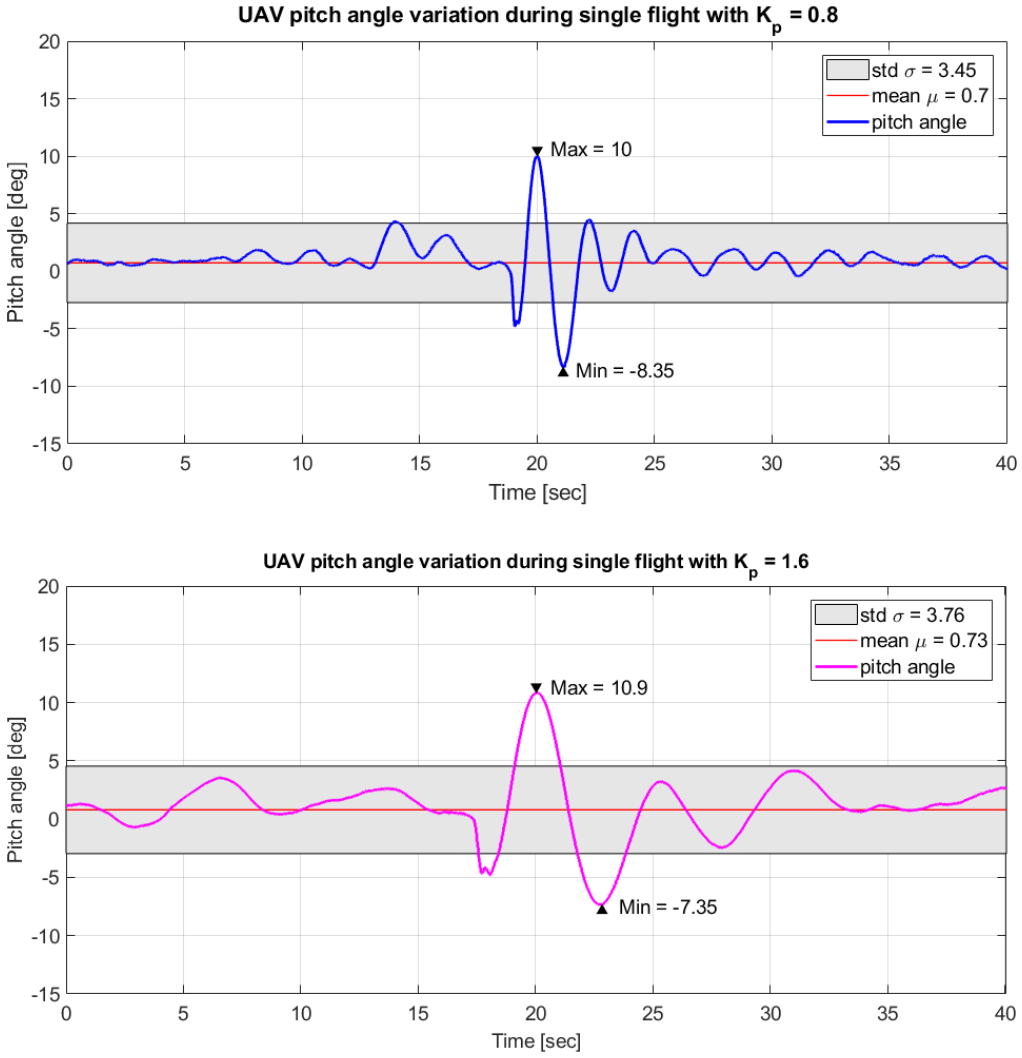

In Figure 4.4 the variation in pitch angle over time is displayed for each K_p tested. In each sub-figure, a sample of the pitch data captured during a single flight has been plotted against the averaged mean μ_{pitch} and standard deviation σ_{pitch} from Table 4.2 to provide a visual clue on the increase of σ_{pitch} (width of the greyed bands) over higher gains. The peak amplitude of each sample flight also increases accordingly.

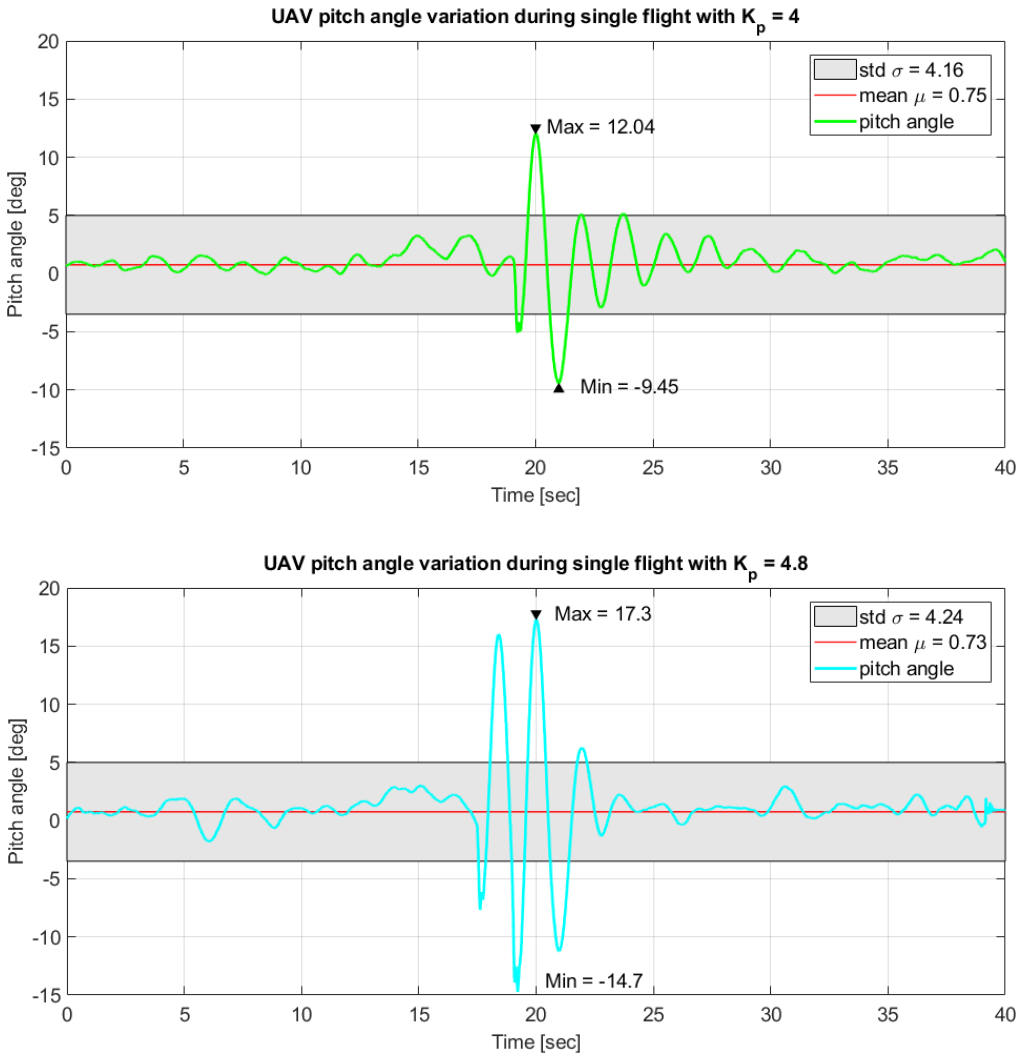

Figure 4.4: Four sample flights illustrate the variation in pitch angle over time for each K_p tested. As K_p increases, higher disturbances are sensed in the pitch.

A comparison of the forces exerted by the end-effector during interaction is illustrated in Figure 4.5. It is demonstrated that more compliant configurations generate lower forces at the end-effector, and this is in line with the theoretical evaluation seen in the previous section. Figure 4.7 shows the force exerted with gain $K_p = 4.8$ where a stable interaction is achieved with the wall for a period over 10 seconds. This behaviour is a consequence of the increased PID control action that generates a higher force in response to higher disturbances and it overcomes the actuator's own friction.

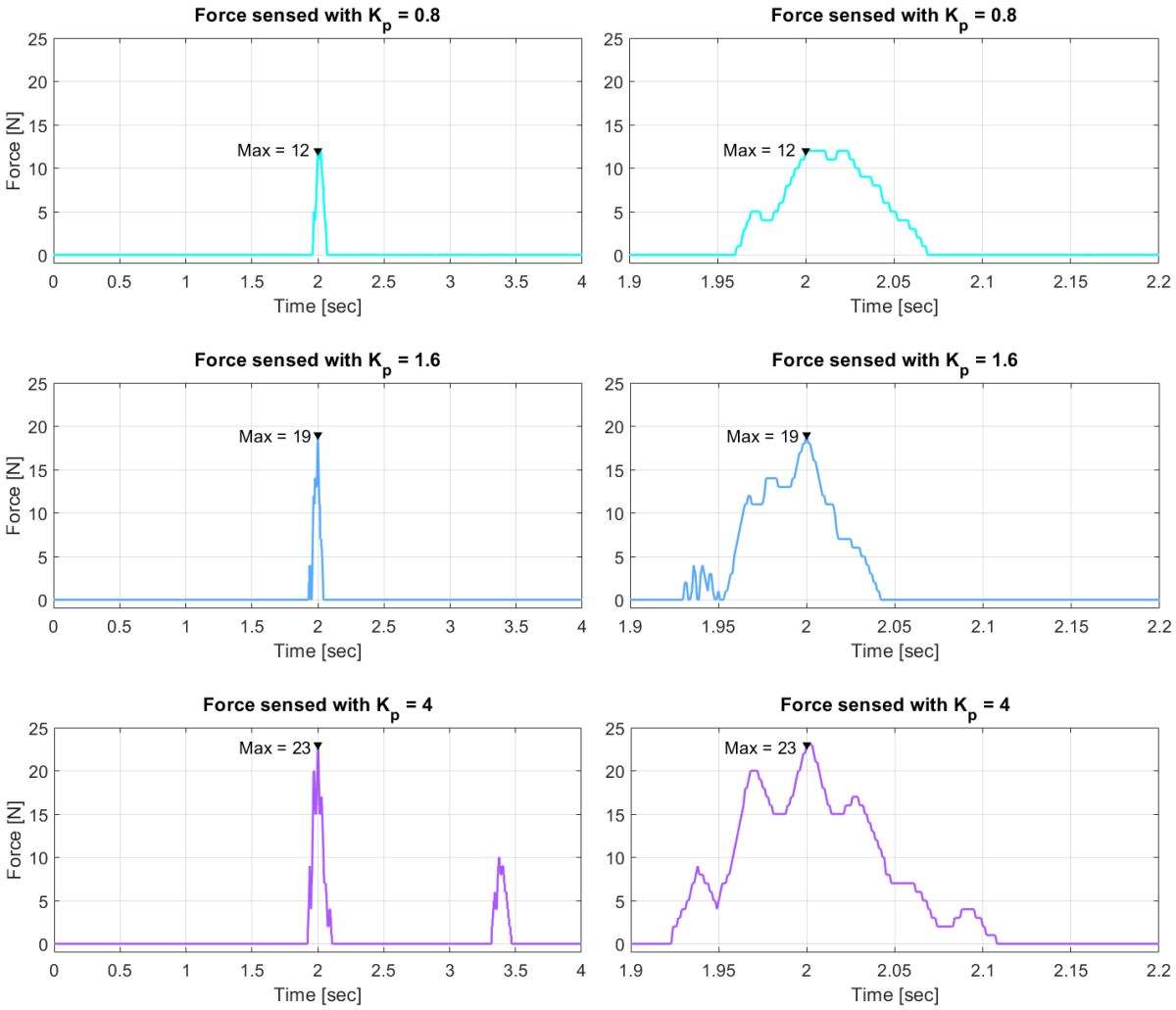

Figure 4.5: On the left side - a comparison of forces exerted by the adaptive compliance manipulator for different proportional gains. Lower gains produce a less aggressive behaviour during interaction and therefore lower forces. On the right side - a detailed image of the plots, showing the force curve within [1.9 2.2] seconds.

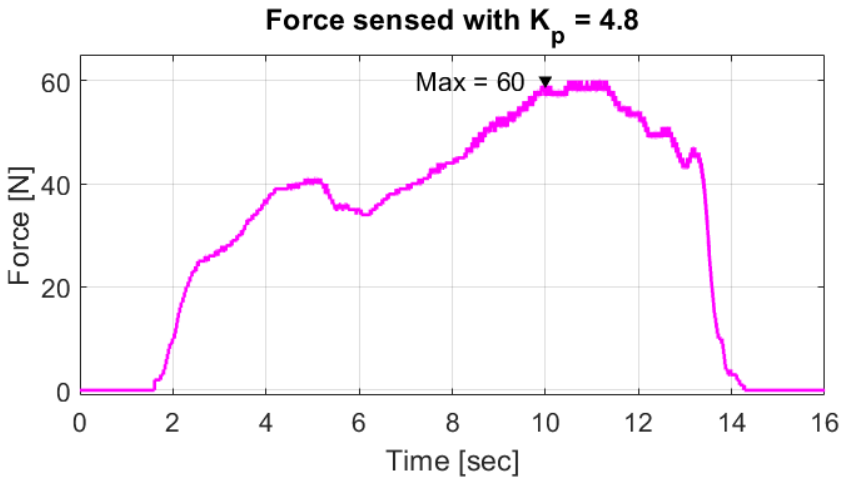

Figure 4.6: The force exerted by the adaptive compliant manipulator during a sample flight with K_p = 4.8.

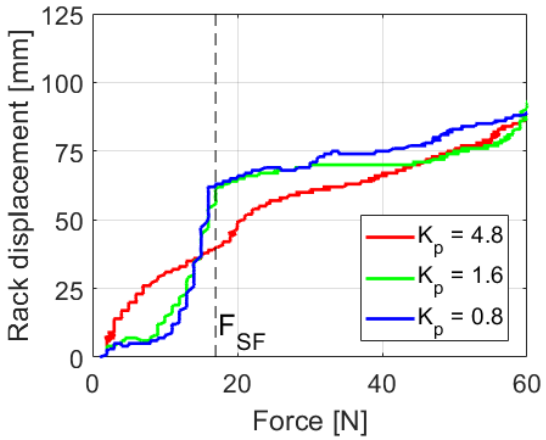

Figure 4.7: Response to external force on the actuator's displacement for given controller gains K_p.

(bearings, gears and motro's resistance to turn) To better understand this, a characterisation of the actuator is presented in Figure 4.7. Within this experiment, a set of hanging weights was attached to the rack, at increments of 100 grams. The position of the rack was monitored and measured by the encoder at each weight increment for a given K_p. It was seen that, at K_p equal to 0.8 and 1.6 the rack displacement was less than 5 mm for up to 1.5 kg, and spiked to 63 mm as the weights were generating 18 N force on the actuator (about 1.8 kg). This phenomenon can be explained as the pulling force of the weights on the actuator needed to be high enough to overcome the resistance of the internal electro-mechanical components and therefore generate enough displacement on the rack. The resistance within the actuator results from a number of

factors, some of them generated by the mechanical components, e.g. friction within the bearings and the gears teeth, and some of them resulting from the electronics, e.g. the inherent resistance of the motor to spin. In any case, the behaviour of the actuator is affected by these factors regardless of the controller governing the motion. For lower gains such as 0.8 and 1.6, the PID action was only triggered by a higher error in position, as small errors were not compensated for. For $K_p = 4.8$ the controller action was initiated since the very beginning of the experiment and at low forces (weights) applied to the actuator. This behaviour is shown in Figure 4.7. In the figure, the force overcoming the electro-mechanical resistance of the actuator at low K_p gains is denoted as F_{SF}.

	$K_p = 0.8$	$K_p = 1.6$	$K_p = 4$	$K_p = 4.8$
$\mu_{force} \pm \sigma_{force}$	9.66 ±1.86	15 ±2.24	17.5 ±4.11	53.83 ±4.96
max_{force}	12	19	23	60

Table 4.3: Average μ and max values of forces sensed whilst pushing and tapping on a surface, with different proportional gains K_p. Each average μ in the table is computed over a number of at least 10 flights for each K_p.

Table 4.3 illustrates the force peak μ_{force}, standard deviation σ_{force} and the maximum force measured for each K_p value and averaged throughout the entire set of experiments. As expected, the mean and maximum values increase with higher proportional gains, where a stiffer spring is emulated by the controller. The value of σ_{force} in the table provides information on the repeatability of the experiment: higher gains cause an increase in σ up to 4.96 N, as opposed to more compliant configurations that typically provide a more consistent response and less variations in the force.

4.2.3 Tapping Task

In this section the ability of the proposed manipulator to *tap* onto a surface is demonstrated. The experiment is laid out as follows: the UAV approaches the wall at a constant speed of 0.25 m/s and, when the wall is in range, the rack protrudes out and establishes contact with it. Two set-points act as lower and upper bounds in the PID control, which periodically switches between them causing the end-effector to tap onto the surface. As a number of sequences is completed, the rack retracts and the vehicle is homed.

To validate the tapping behaviour, a set of 10 experiments is conducted at a fixed proportional gain, namely $K_p = 4$. The reason behind choosing this specific gain in the tapping experiments is because the gain should ultimately be high enough to provide consistent and reliable response within the operation, hence posing a lower bound on the selection of the K_p. The highest gain available however ($K_p = 4.8$) was not suitable for this type of task, proving too stiff and inducing oscillations. Therefore, the choice fell on the second highest gain, namely $K_p = 4$.

The natural response of the system results in a tapping excitation of approximately 10 Hz, as seen in Figure 4.8. By looking at the force measurement in Figure 4.8, an initial peak in the force can be identified, followed by a period of transition until a steady limit cycle is reached. The average force exerted during tapping throughout all flights is $\mu \pm \sigma = 5.6 \pm 2.27$ N. The frequency of taps measured on the wall was 11.16 Hz on average.

In practice, the desired tapping/excitation frequency is application-specific, with typical requirements expected to be in the range of 0-20 Hz. Future refinements in both

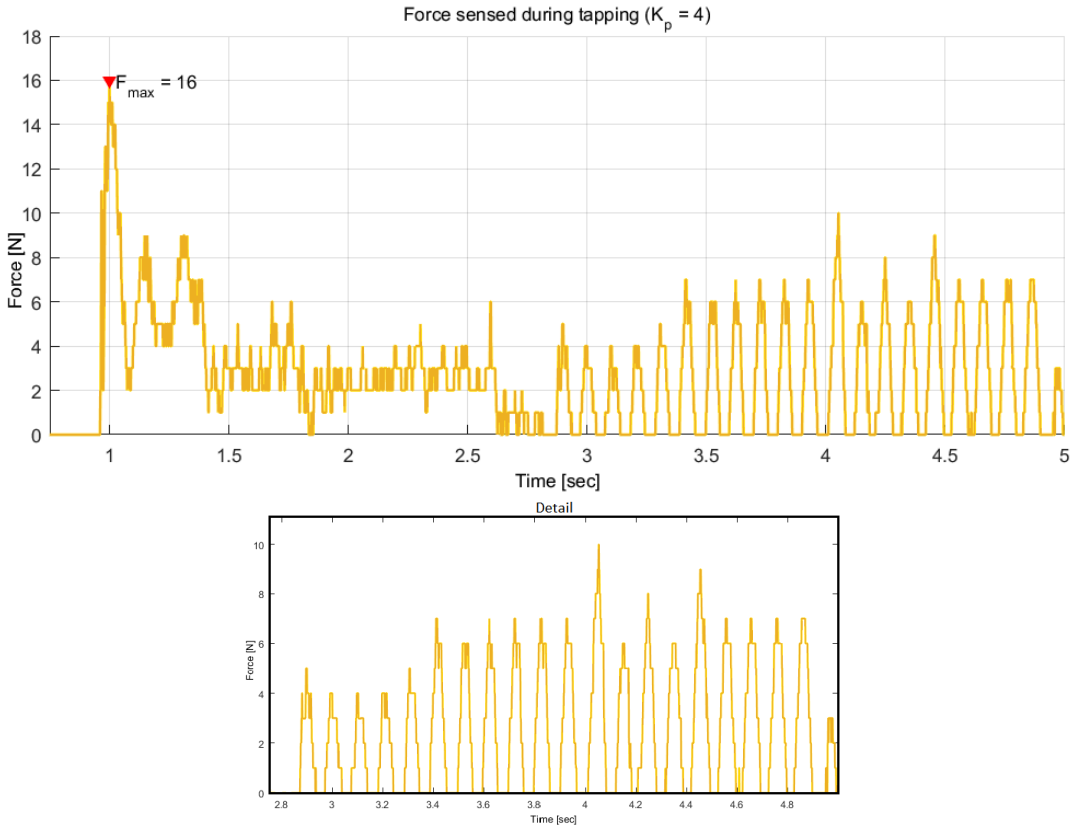

Figure 4.8: Tapping force sensed in a sample flight: after an initial impact and transition period the response moves towards a steady limit cycle (displayed in the figure detail).

the manipulator and vehicle control system could focus on minimising the transition period as the aircraft initiates the tapping process, as well as minimising the initial impact and reaching a steady state excitation faster.

4.3 Conclusions

The work presented in this chapter proposes a novel approach to aerial manipulation with the introduction of variable compliance on the manipulator. This behaviour is achieved through a variable-gain PID controller, which not only allows to adjust the force output at the end-effector, but also it favours the vehicle's response during physical interaction.

From the experiments conducted, some key results and *lessons learnt* are derived:

- the ability to physically apply forces with the UAV through the use of an active manipulator was achieved within the experiments. In addition, unprecedented forces of over 20 N were exerted at the wall in a repeatable and robust fashion;
- the ability to adjust the force output thorough the tuning of the controller's gains. Over 50 flight experiments demonstrate the variable-compliance behaviour and show how compliance aids the stability of the vehicle by lessening the propagated disturbances over the CoG. This outcome shows the potential of the control approach for tackling a variety of aerial tasks;
- the ability to adjust the force curve and the time in contact with the wall were demonstrated with the proposed design: a regular excitation on a surface over a given period of time (tapping) were demonstrated for the first time on an aerial manipulation. This type of interaction is more challenging than other contact-based operations, as it naturally induces disturbances on the vehicle, e.g. bouncing. Repeated cycles of rapid force exchange were performed in flight with a repeatable outcome.
- the variable-gain PID control has proved successful within this framework. However, other types of adaptive controllers could be implemented, e.g. Model Predictive Control methods (MPC), where the adjustment of the controller gains is achieved in real-time, adding a benefit to the dynamic response;
- the presence of the ultrasonic sensor can automate the manipulator's behaviour in the proximity of the target, however the sensor readings were often unreliable and

suffered from latency. This led to late engagement of the end-effector with the wall surface in multiple occasions. Other rangefinder solutions could be investigated for future developments;

- the presence of a rotational degree of freedom allows the manipulator to independently pitch, regardless of the vehicle angular configuration. For the proposed design, the rotational DoF was introduced to move the end-effector location on the vertical axis, hence favouring a lesser momentum on the vehicle. However, the servo motor actuating the rotational DoF suffered from latency and could not consistently adjust the angle in real-time. As a result, the end-effector location was often not aligned with the CoG, inducing a non-zero momentum on the aircraft. Further solutions could be investigated to provide a better alignment between the end-effector and the aircraft CoG.

To conclude, this works aims to demonstrate the potential and versatility offered by the proposed aerial system as a whole, and the effectiveness of variable compliance implemented for this design. This feature could be something useful for UAVs, which are often deployed for interaction with various targets and environments, having to comply with different materials, textures, and other mechanical constraints. Future developments will look at ways to achieve a fine tuning of the force output and to further implement compliance for more challenging applications.

CHAPTER 5

AN AERIAL MANIPULATOR FOR THE INSTALLATION AND RETRIEVAL OF SENSORS IN THE ENVIRONMENT

Publications

This chapter has resulted in the following peer-reviewed research outputs:

1. Hamaza, S., Georgilas, I., Fernandez, M., Sanchez, P., Richardson, T., Heredia, G., Ollero, A. (2019). Sensor Installation and Retrieval Operations using an Unmanned Aerial Manipulator. *IEEE Robotics and Automation Letters, 3*(4), 2793 – 2800. [68]

2. Hamaza, S., Georgilas, I., Heredia, G., Ollero, A., Richardson, T. "Design, Modeling and Control of an Aerial Manipulator for Placement and Retrieval of Sensors in the Environment." *Journal of Field Robotics* (in print). – [69]

In this chapter, the ability for an aerial manipulator to install and retrieve smart sensors in the environment is addressed. Remote sensing can bring several advantages as it allows real-time monitoring of infrastructure and on-line surveying, therefore contributing towards hazard prevention and a faster response in case hazards occur. Safety is of paramount importance when it comes to the development of new infrastructure, and this is the reason why on-line sensing is nowadays an essential feature that allows to build more robust reliability curves and reach higher safety standards.

Aerial manipulators capable of installing sensing devices in hard-to-reach locations or wide-spread areas can greatly benefit already existing infrastructure by adding this desirable feature. Example scenarios for these aerial applications are the installation of vibration sensors to monitor the structural integrity of bridges and dams, or thermocouples on the walls of high industrial chimneys to track the temperature of exhaust fumes released in air, or smoke detectors on forest trees that check the levels of carbon dioxide for fire prevention, and so on.

To carry out installation and retrieval tasks, the aerial manipulator should be capable of exerting a force on the environment and have a designated tool that aids the positioning of the sensing devices. As previously seen in chapter 2, the state of the art in aerial manipulation has progressed towards new methods of delivering the force at the end-effector, exploiting the rotors' thrust of the flying vehicle in different ways.

In [48] the use of a tilt-rotor UAV allows to generate a force at the hand-tool while the retained attitude control ensures stable hovering. Similarly in [49] a UAV with "canted" thrusters enables dexterous interaction with the on-board parallel manipulator. In [52, 53] this concept is stretched with the use of a tricopter that has an additional fourth propeller mounted horizontally. The "boomcopter" utilises the horizontal propeller propulsion to apply a force in hover state through a fixed end-effector. Lastly in 2017, substantial forces up to 16 N are applied by an aerial vehicle that pitches at high angles, i.e. up to 45°, against a vertical surface, transferring the horizontal thrust component on the target surface [51].

The key contribution highlighted in this chapter lies in the novel approach to force exertion by the aerial manipulator. The force output generated at the end-effector results from the combined action of the UAV's pitching motion and the active manipulator itself, and allows to have a compliant approach with the target surface and a slow force build-up. The use of compliance in this scenario serves a double function: it provides a safe interface between the end-effector, the sensor to be installed, and the environment (for interaction with delicate sensors or surfaces), and it aids the stability of the vehicle during interaction.

A refined version of the manipulator's design is proposed, with two bespoke end-effector solutions for installation and retrieval tasks respectively. This design together with the control architecture are tested in different scenarios to demonstrate the robustness of the approach. The interaction with both vertical and cylindrical surfaces is tackled, in indoor and outdoor testing.

5.1 Aerial Manipulator's Design Refinement

As previously discussed, there are several benefits associated with low-DoFs manipulators. Some of them are are the lower kinematics and control complexity, lower mass, lower repair and maintenance associated costs, better manoeuvrability and battery life. Where possible, it is therefore essential to limit the total DoFs and avoid redundancy while still devising the right tool for the job.

To tackle installation and retrieval of sensors in the environment, the design of the aerial manipulator was revisited for this application. Some of the limitations of the present version were highlighted at the end of chapter 4, and those have led the following refinement stage. The changes brought together are hereby listed, with detailed discussion in the following sections.

- introduction of aluminium components in the linear joint to ensure a more accurate coupling in the pinion-rack transmission;
- increased range of motion of the end-effector through the use of a longer rack;
- removal of the rotational degree of freedom;
- refinement of the housing for the mechanical components and introduction of additional bearings to improve the pinion-rack coupling;
- introduction of better sensing: a high precision, high sampling rate distance sensor replaces the ultrasonic solution;
- introduction of better electronics: a high performance digital positioning controller and an on-board computer with higher computational capabilities replace the previous solutions;
- better user interface and software integration through the use of Robotic Operating System (ROS).

5.1.1 Mechanics

In the new version of the manipulator, the slider joint is still embodied by the rack-and-pinion mechanism, where the torque/force transmission is improved thanks to the use of an aluminium-aluminium coupling. From the experiments carried out, it was noticeable that the Delrin material of the rack is more prone to deterioration and wear

when coupled with a stainless steel pinion. The wearing of the Delrin teeth was also enhanced by the high forces propagating during impacts in the multiple experiments conducted.

The replacement of a *standard* pinion with a custom-made double-sided pinion supported by two ball bearings also benefits the accuracy and the coupling. In fact, the ball bearings serve a double function: they contribute to release the motor from any radial tension that might generate during interaction, and they ensure that no deflections or moments are transferred to the motor via the pinion.

The decision to remove the rotational degree of freedom follows the lessons learnt from the initial set of experiments discussed in the previous chapter. The servo motor could not operate real-time adjustments of the pitch angle at the end-effector, as the motor's response was too slow to be used in such dynamic scenario. A solution to this could have been to incorporate a higher performance DC brushless motor, similar to the one of the slider joint. However the mass restrictions forced to discard this solution.

To compensate for the lack of the independent pitch motion in the manipulator, the housing of the slider joint was revisited to fit an inclined base. Such inclination in the housing allows the end-effector location to be closer to the aircraft CoG on the vertical axis, and therefore decrease the induced momentum. The angled base features the design parameter δ. To select the right angle, the data-sets produced on the experiments were evaluated to extrapolate the average pitch angle at which the vehicle approached the target surface. Such information allows to compute some basic trigonometry calculations and retrieve the optimal angle that aligns the end-effector with the aircraft CoG.

To account for possible variations in the attitude of the UAV and different speeds of approach in future experiments, the angle δ was chosen to be less than the optimal. This guarantees that the end-effector location will always lay above the aircraft CoG even when pitching more severely. If this condition was not met, i.e. the end-effector location dropped below the aircraft CoG, the induced momentum during interaction would cause the vehicle to collide against the target, as discussed in chapter 3. Figure 5.1 illustrates a cross section of the prismatic joint and its components.

5.1.2 Sensing

Sensing on the manipulator was also improved. In addition to the digital encoder on the DC motor, a high-performance rangefinder replaces the previous ultrasonic solution. The selected sensor is the TeraRanger One, a lightweight and cost-efficient sensor for fast-moving robotics and automation applications. The rangefinder uses the Time-of-

Flight technology and is preferred over ultrasound or infrared technologies as it provides a much higher sampling frequency and long range measurements (over 12 metres). Similarly, laser technology was also discarded due to the bulkiness and high mass of commercially available laser scanners. TeraRanger One is sized 35 x 29 x 18 mm, weighs 8 g and can measure distance within 14 m ± 4cm under different light conditions, making it suitable for both indoors and outdoors testing.

5.1.3 Hardware and Software Architecture

The on-board flight controller was replaced by the Pixhawk 4® autopilot, with a PX4 firmware. This autopilot offers several flight modes: attitude, position and waypoint, and it is often used in mobile robotics research for its high reliability standards. The ground control software used to calibrate the vehicle's gains is QGroundControl.

The manipulator's on-board computer is replaced by a Raspberry Pi 3 (1.4 GHz 64-bit quad-core ARM Cortex-A53 processor) with wireless LAN connectivity and logging capabilities. This processor is responsible for the aerial manipulator's task management during experiments and the manipulator's control blocks. The brushless DC motor is actuated by a Maxon EPOS2 24/3 motor digital controller board. This motor board offers high sampling rates in all operational modes: 10 kHz in *current mode*, and 1 kHz in

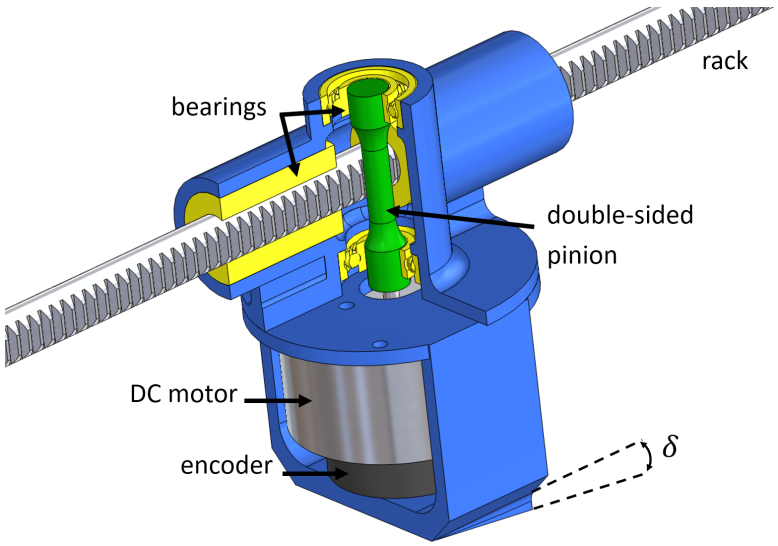

Figure 5.1: Cross section of the transmission mechanism and relevant components. A double-sided pinion (in green) drives the motion of the rack, whilst the encoder measures the relative position. A set of 2 ball bearings and 2 linear bearings (in yellow) assure accurate positioning of the pinion and the rack respectively.

position and *velocity* mode. Such high performance allows to have real-time control over the manipulator, within a compact and lightweight solution (10 g).

Table 5.1 displays the new and the replaced components in the refined version of the manipulator, and Table 5.2 illustrates a a comparison between the aerial system and the manipulator's relevant properties.

Table 5.1: Table with information on the new and replaced components.

Image	Model	Specs.
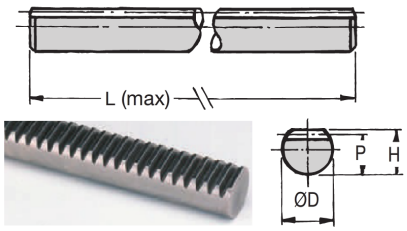	• Manufacturer: HPC Gears • Material: Aluminium • Part number: ATR0.5	• MOD=0.5 • P=8.70, ⌀=10, H=9.20, L=500 [mm] • Weight = 90 g
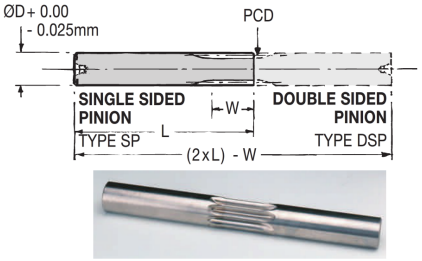	• Manufacturer: HPC Gears • Material: Aluminium • Part number: DSP0.5-9	• MOD=0.5, Teeth=9 • PCD=5, ⌀=8, W=10, L=30 [mm] • Weight = 21 g
	• Manufacturer: SKF • Part number: 6000	• $\varnothing_{inner}$=10 [mm] • $\varnothing_{outer}$=26 [mm] • Quantity=2 • Weight = 18 g

Image	Model	Specs.
	• Manufacturer: Raspberry • Part name: Raspberry Pi 3	• QuadCore 1.2GHz Broadcom BCM2837 64bit CPU • 1GB RAM • 4 USB ports, 1 microSD • 2.4GHz 802.11n Wireless • Weight = 42 g
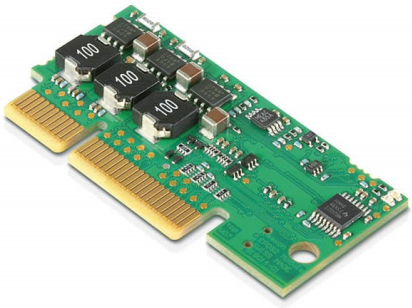	• Manufacturer: Maxon Motor • Part name: EPOS2 24/3 Digital Positioning Controller	• Operating voltage = 11V • Max. Voltage = 24V • Max. output current = 4A • Sampling rate current mode = 10kHz • Sampling rate position & velocity mode = 1kHz • Weight = 10 g
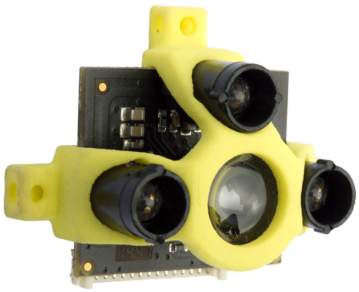	• Manufacturer: TeraBEE • Part name: TeraRanger One	• Principle: Infrared Time-of-Flight (ToF) • Range = 0.2 to 14 [m] • Resolution = 0.5 [cm] • Sampling rate = 1kHz • Weight = 8 g

Table 5.2: System components and specifications.

QAV400 quadcopter		1-DoF manipulator	
Motors	FX2216-9 1100kv	Motor	Maxon motor DC45 flat 50 Watt, 780 mNm stall torque
Propellers	8x5”	Motor controller	Maxon EPOS 24/3A Digital Controller 24 V, 3 A, 10 kHz sampling rate, 10 grams
Battery	LiPo 4s 2200 mAh	Battery	LiPo 4s 2200 mAh
Flight controller	Pixhawk 4 PX4 firmware	On-board computer	Raspberry Pi 3
Sensing	2 IMUs Barometer GPS	Sensing	Terarager One rangefinder 0.2 - 14 m range, 1kHz sampling rate MILE Maxon Encoder, 1024 CPT
Max. payload	0.8 kg	Max. payload	0.2 kg (1 kg if used stand-alone)
Flight time	10 minutes @0.5 kg	Operation time	max. available flight time or 2 hours if used stand-alone

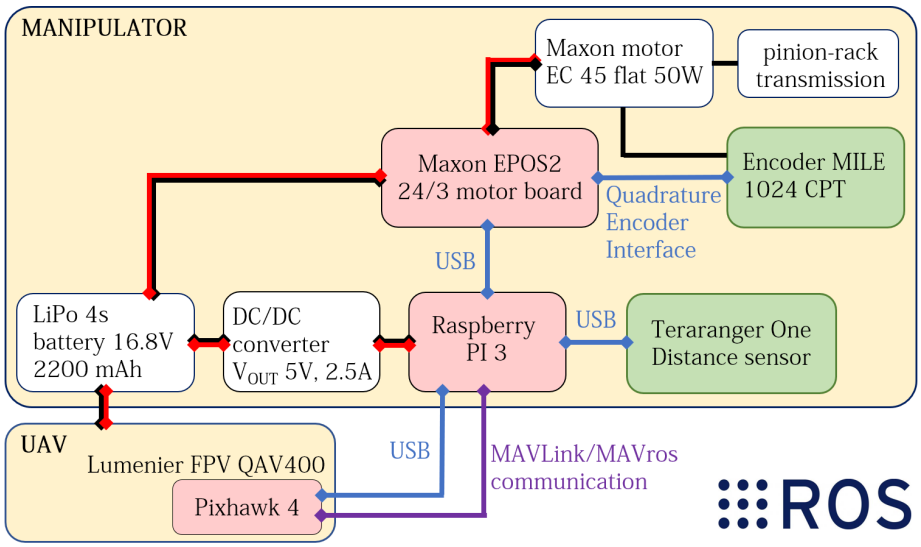

Figure 5.2: Hardware and software architecture of the aerial manipulator. The red blocks highlight the on-board processors, while the green ones the sensors.

The software implementation is done in Robotics Operating System (ROS). The main control node runs on the on-board Raspberry Pi and communicates with the UAV flight controller through a MAVLink/MAVros bridge. The overall system architecture is presented in Figure 5.2.

5.2 Configuration & Mass Properties

Similarly to what was seen in the first design stage, the manipulator's components are placed in such a way that the weight is distributed and symmetrical with respect to the vehicle's CoG. In this respect, the prismatic joint is mounted towards the front of the aircraft, while the battery is placed at the back to balance out the weight. Figure 5.3 illustrates some CAD drawings of the aerial manipulator in the new layout.

In Table 5.3 the mass properties of the UAV and UAM are presented to highlight the differences in inertia of the present system with and without the maipulator's on-board. The centre of mass (CoM) coordinates are calculated based on a reference frame positioned in the centre of the vehicle with *z-axis* pointing upwards, x and y axes pointing towards the front and the side of the vehicle respectively. From the table it can be inferred that the presence of the manipulator does not have a significant impact on the aircraft's CoG and on the moments of inertia along the main axes. In fact, the CoM of the system is only shifted by 1 cm along the *z-axis* and 2 cm along the x.

Table 5.3: A comparison of the UAV and UAM mass properties. The mass m, centre of mass (CoM) coordinates, and moments of inertia J_{ii} are calculated according to the reference frame shown in Figure 5.3.

	Aircraft only	Aircraft & manipulator	
m	1.35	1.85	$[kg]$
x_{CoM}	0.48	0.5	$[m]$
y_{CoM}	0	0	$[m]$
z_{CoM}	0.17	0.18	$[m]$
J_{xx}	0.03	0.03	$[kg \cdot m^2]$
J_{yy}	0.04	0.05	$[kg \cdot m^2]$
J_{zz}	0.07	0.07	$[kg \cdot m^2]$

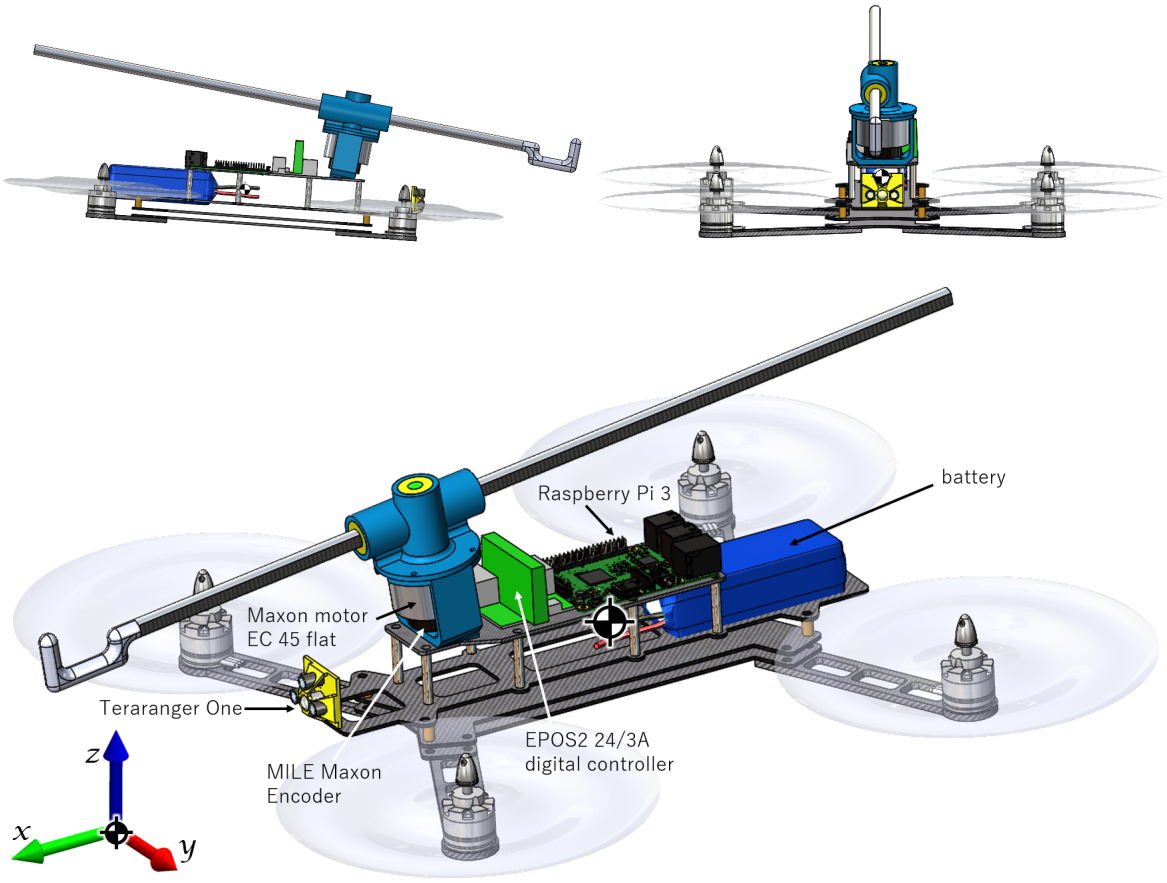

Figure 5.3: 3D view of the aerial manipulator in the new layout. For clarity, the reference frame is shown on the side of the figure. The colours used in these CAD drawings are not necessarily representative of reality, they originate from a style choice.

5.3 End-effectors Design

Two different end-effectors are devised to address sensor installation and retrieval operations. For the placement task, the use of magnetic force is adopted to hold the sensor in place during flight and installation. The tip of the rack is equipped with a flat surface that resembles a lid. On top of it, a series of small Neodymium magnets are arrayed in such a way to prevent repulsion forces in between them. The same configuration is replicated on the outside of the sensor case, by mirroring the magnets. The adhesion force produced by the magnets F_{grip} must be enough to carry the sensor itself and overcome the forces generated by aerodynamic disturbances in flight, especially during take-off and in proximity of the wall:

$$F_{grip} \geq m_p g + F_{dist} \tag{5.1}$$

where m_p is the payload mass (e.g. sensor), g is the gravitational acceleration and F_{dist} is the force due to disturbances in flight, e.g. turbulence generated by the surrounding propellers during take-off, or due to the wall-effect. The computation of F_{grip} can be quite complex especially because it is dependent on the force due to disturbances, which is unknown and varies for each flight. To derive F_{grip} empirically some preliminary experiments were performed testing the reliability of different sizes of magnetic surface available. It was found that 2.5 cm^2 of magnetic surface provided a reliable adhesion

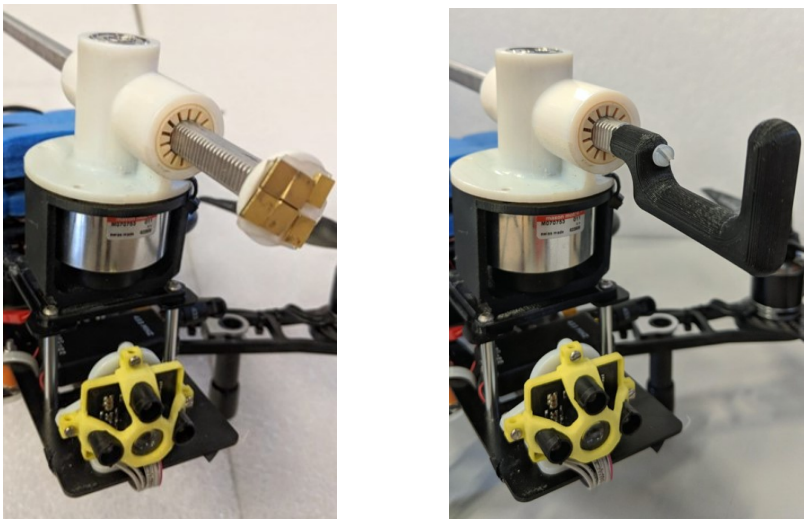

Figure 5.4: Two gripper designs are manufactured for installation and retrieval tasks. The former uses an array of small magnets to hold the object in place during take-off and in the proximity of the obstacle; the latter consist of a long open hook that engages with a looped ring on the sensor case.

between the gripper and a sensor of approximately 40 g, experiencing a failure rate of 2.08% spanned over 48 flights.

For retrieval tasks the gripper consists of a square hook with a threaded hole at one end. To secure the hook in place, a bolt is fastened along the hole, inside the rack. This design is selected as it facilitates the grasp, and for its manufacturing simplicity. To allow the hook to engage with the sensor a metal string was looped around the sensor case, acting as a support for the gripper and easing the pull. Figure 5.4 illustrates a close-up of both designs.

5.4 Modelling and Kinematics

Let us consider a quadcopter equipped with 1-DoF manipulator as depicted in Figure 5.5. By defining two coordinate frames, i.e. the ground frame $\mathcal{G}$ and the body-fixed frame $\mathcal{B}$, one is able to fully describe the motion of the aerial platform in space. However, in aerial manipulation two additional reference frames are adopted to account for the presence of the manipulator and the object to manipulate. The first, $\mathcal{M}$, is centred in the manipulator's CoG and the second, $\mathcal{E}$, is centred in the gripper/hand tool.

It is now assumed that the manipulator centre of gravity coincides with the one of the aircraft. This assumption is based on the design choices discussed in the previous section and on the values found in Table 5.3: the proposed compact manipulator gathers its components at the base, shifting the manipulator's centre of mass towards the core of the platform where it is mounted. Also, while in operation the only moving part is the rack, which accounts for less than 5% of the aerial manipulator's total mass. Therefore, the rack's motion only brings a limited change in inertia of the system, without impacting on the CoG position as much as other bulkier solutions, see [13, 42, 59].

The reference frames used to solve the kinematic problem are displayed in Figure 5.5. Let us define three pose vectors: ${}^{\mathcal{G}}\boldsymbol{\pi}_{\mathcal{B}}$ describes the pose of the aircraft with respect to the ground frame, and vectors ${}^{\mathcal{G}}\boldsymbol{\pi}_{\mathcal{E}}$ and ${}^{\mathcal{B}}\boldsymbol{\pi}_{\mathcal{E}}$ describe the pose of the end-effector with respect to the ground and aircraft frames respectively. Vectors $\boldsymbol{\pi}$ consist of linear and angular terms about the *x*-*y*-*z* axes.

Due to the nature of quadcopters being underactuated systems the kinematics problem of the aerial manipulator is considered as a whole, as disturbances in the *roll-pitch-yaw* states affect the position of the end-effector. Hence the kinematic chain $\boldsymbol{\chi} = [\zeta_x\ \zeta_y\ \zeta_z\ \phi\ \theta\ \psi\ \mathbf{q}]^T$ describes the aerial system as a single, where $\boldsymbol{\chi}$ represents a $(6+1)$ dimension vector consisting of the aircraft linear and rotational terms (6 DoFs in

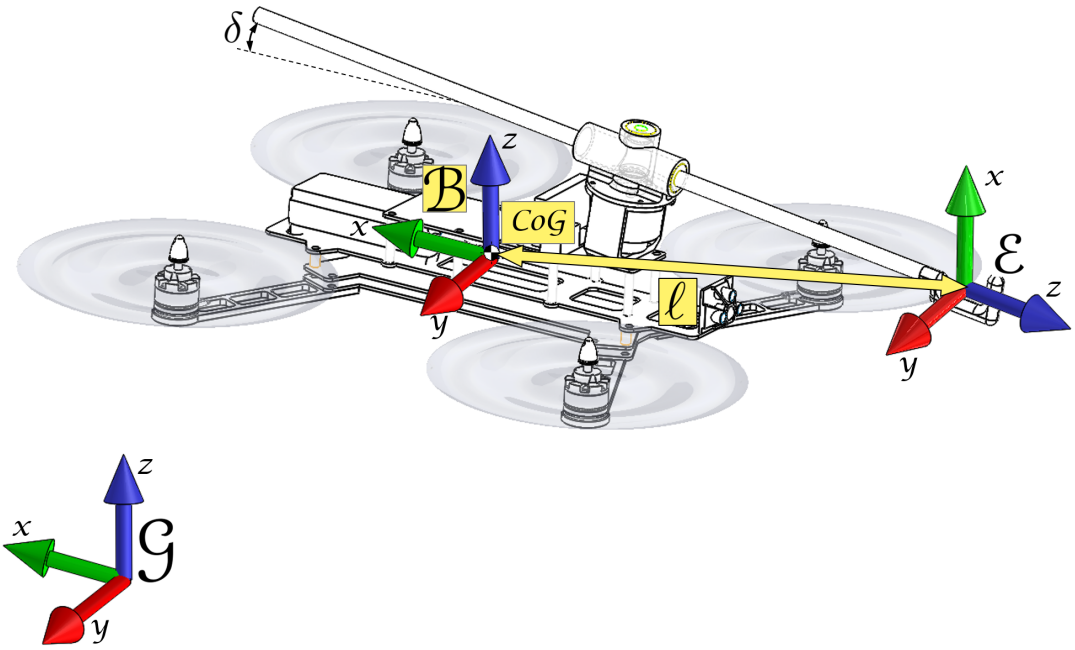

Figure 5.5: Aerial manipulator's reference frames.

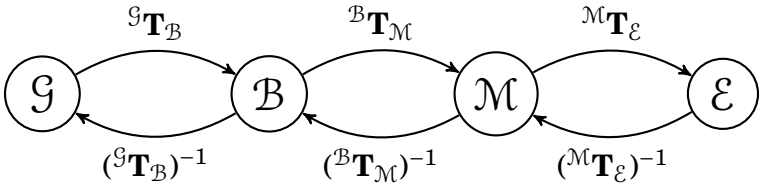

Figure 5.6: Schematic diagram representing the forward and inverse Kinematics problem for a generic aerial manipulator.

space), and the scalar $\mathbf{q}$. The position of the end-effector with respect to the ground frame is represented by vector ${}^{\mathcal{G}}\boldsymbol{\pi}_{\mathcal{E}}$, which combines the multiplication of three homogeneous transformation matrices as follows: Each homogeneous transformation (${}^{i}\mathbf{T}_{i+1}$) is a (4 × 4) matrix encompassing rotational and translation information of a space vector from frame i in superscript, to the resulting frame $i+1$ in subscript. Following the assumption that frames $\mathcal{B}$ and $\mathcal{M}$ coincide, the forward kinematics (FK) problem yields to:

$$ {}^{\mathcal{G}}\boldsymbol{\pi}_{\mathcal{E}} = {}^{\mathcal{G}}\boldsymbol{\pi}_{\mathcal{B}} + {}^{\mathcal{B}}\mathbf{R}_{\mathcal{E}}\,{}^{\mathcal{B}}\boldsymbol{\pi}_{\mathcal{E}} = {}^{\mathcal{G}}\mathbf{T}_{\mathcal{E}}(\boldsymbol{\chi}) = {}^{\mathcal{G}}\mathbf{T}_{\mathcal{B}}(\zeta_x\ \zeta_y\ \zeta_z\ \phi\ \theta\ \psi)\ {}^{\mathcal{B}}\mathbf{T}_{\mathcal{E}}(\mathbf{q}) \tag{5.2} $$

The position of the aerial manipulator depends on the relative position of the body-fix frame ${}^{\mathcal{G}}\boldsymbol{\pi}_{\mathcal{B}}$, and the end-effector ${}^{\mathcal{B}}\boldsymbol{\pi}_{\mathcal{E}}$. From Equation (5.2) it is now possible to solve the 1-DoF manipulator FK as a decoupled problem. Let us consider Figure 5.5: the UAV frame $\mathcal{B}$ has the $z_{\mathcal{B}}$ axis pointing upwards; frame $\mathcal{E}$ is rotated clockwise about $y_{\mathcal{B}}$ of an angle of $90° + \delta$, where δ takes into account the small inclination of the prismatic joint

on the platform. Therefore, the end-effector is aligned with $z_{\mathcal{E}}$ and the distance between frames $\mathcal{B}$ and $\mathcal{E}$ along $z_{\mathcal{E}}$ varies with the motion of the slider, namely variable ℓ. With the above conditions, the Denavit-Hartenberg parameters are:

Table 5.4: Denavit-Hartenberg parameters for the proposed 1-DoF manipulator.

	i	a_{i-1}	α_{i-1}	d_i	θ_i
Link	1	0	$90° + \delta$	ℓ	0

which yields to:

$$(5.3) \qquad {}^{\mathcal{B}}\mathbf{T}_{\mathcal{E}}(\mathbf{q}) = \begin{bmatrix} 1 & 0 & 0 & 0 \\ 0 & cos(90° + \delta) & -sin(90° + \delta) & -\ell sin(90° + \delta) \\ 0 & sin(90° + \delta) & cos(90° + \delta) & \ell cos(90° + \delta) \\ 0 & 0 & 0 & 1 \end{bmatrix}$$

The last column of the matrix displays the end-effector *x-y-z* coordinates with respect to frame $\mathcal{B}$. By knowing the extension of the rack, namely variable ℓ thanks to the on-board encoder, and the angle δ as part of the manipulator's design choices, the manipulator's FK problems is solved. The computation of the FK will then be used in the control block of the manipulator, as seen in the following section.

5.5 Control

The control method used in this work focuses on the ability to install and collect small objects in the environment, such as smart sensing devices. Breaking down the task requirements leads to the ability to apply a compression or tension force over a surface, hence the ability to control the interaction force is tackled. The presence of the active slider will allow to control the way the aerial manipulator approaches and eventually makes contact with the surface, by using it as a mechanical impedance tool on the environment. Another advantage of having an active manipulator as opposed to a passive one, is that it caters the UAV with an additional DoF and allows for a prompt, quicker response to the system as a whole. This is possible thanks to the simpler dynamics governing the manipulator and the embedded high-performance motor board of the joint.

5.5.1 Current-to-Force Mapping

The active prismatic joint is controlled in force through a PI current controller. Brushless DC motors present a constant relationship between the input current and the generated

output torque, in accordance with the motor's specifications. For the selected motor the torque constant provided by the manufacturer is K_T = 33.5 mNm/A. The estimated manipulator's force $\mathbf{F}_m$ is proportional to the motor's output torque. Hence, introducing K_T yields to:

$$\mathbf{F}_m = c\, K_T r_p \varepsilon_e \varepsilon_m \tag{5.4}$$

where c is the input current, K_T is the torque constant and r_p is the pinion pitch radius. The above equation also factors in the efficiency loss in the actuator due to its internal friction ε_e, and the one due to the gearing in the pinion/rack transmission, ε_m. Both ε_e and ε_m are <1 and can be derived experimentally. Preliminary experiments are conducted to evaluate the manipulator force output in static condition, in particular the mapping between the current and the rack feed force. The experiments consist in generating a step signal in current on the motor, increasing by 100 mA every 5.5 seconds while the tip of the rack is in contact with a surface. The output force along the rack is then measured at the tip, via a 6 axis force/torque sensor.

Results are shown in Figures 5.7 and 5.8. The former shows the force and current signals plotted over time. The horizontal blue lines show the mean value of the force data, whilst the grey vertical lines display where an abrupt change in the mean value of the force is met. These changes are in conjunction with the current steps, despite a small delay at the beginning of each line due to the time shift between the current signal sent by the motor and sensed by the force sensor. It can be observed that the minimum current required to overcome the static friction of the system and sense a force of about

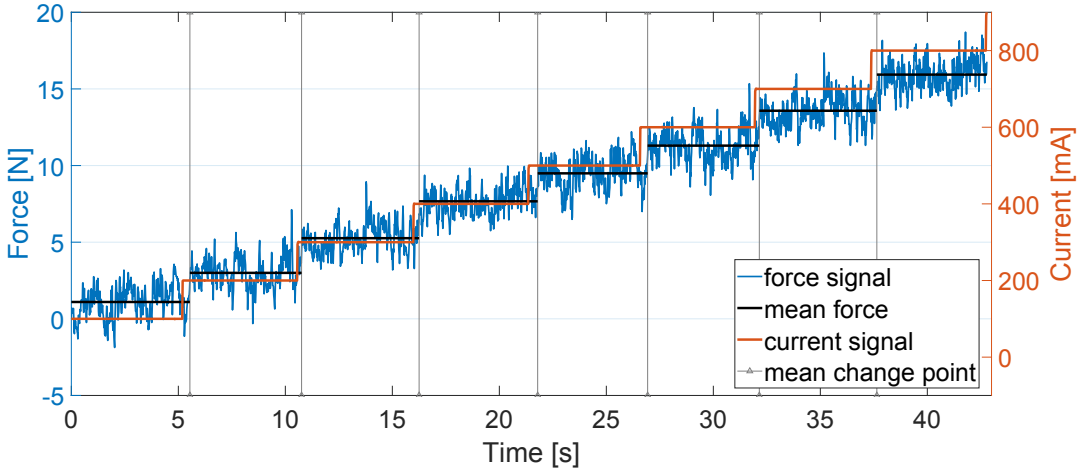

Figure 5.7: Evaluation of the manipulator feed force in static condition: mapping between the input motor current (right axis) and resulting output force measured via a force/torque sensor (left axis). The relationship between the two variables is linear.

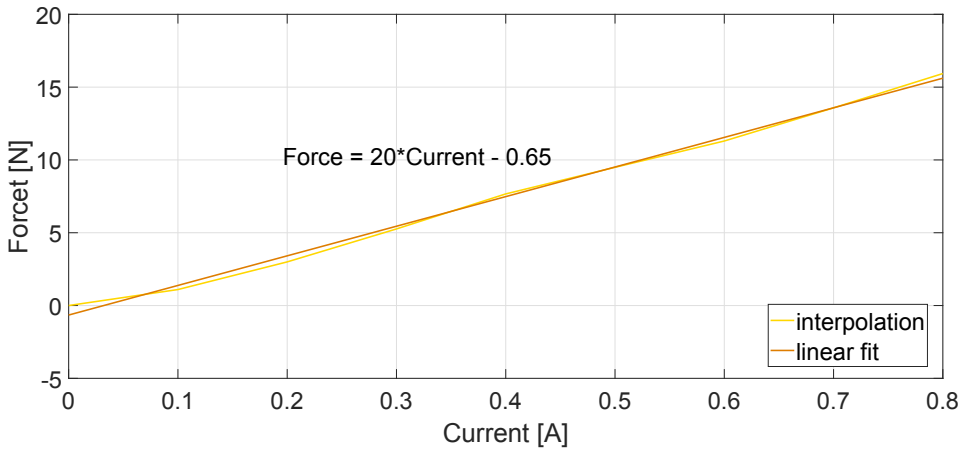

Figure 5.8: Interpolation of the mean force values of the current-to-force mapping of the previous figure and a 1st-order fitting.

1.6 N is 100 mA. Figure 5.8 shows a line connecting the mean values in force (yellow line) and the linear regression of those (orange line). The equation displays the relationship between force and current found experimentally and can be compared to Equation (5.4) where the product of coefficients $K_T r_p \epsilon_e \epsilon_m$ can be grouped in single constant, namely the slope of the linear fit. The range of operation of the motor current used in the later flight experiments is below 600 mA, and this is in line with the values calibrated in this experiment.

5.5.2 Pitch-to-Force Mapping

Besides the action of the manipulator, the aerial vehicle contributes to the largest part of the force output on the surface. Let us consider the UAV in contact with the surface by mean of a rigid rod and pitching forwards at an angle of θ. As the rod lies on the y-z plane, the force $\mathbf{F}_a(u)_{z\ axis}$ generated by the vehicle and propagated through the stick will lie on the same plane, as illustrated in Figure 5.9. This force represents the static horizontal component of the vehicle's thrust, along the z axis as follows:

$$\mathbf{F}_a(u)_{z\ axis} \propto mgtan(\theta) \tag{5.5}$$

The above equation shows how the force sensed at the target surface is proportional to the vehicle weight and pitch angle in the static case, however this does not take into account the motion of the vehicle. The dynamics involved in the interaction contribute towards the total contact force, for example the vehicle's speed of approach, the impact with the surface, the aerodynamic disturbances in the close proximity of the wall, and

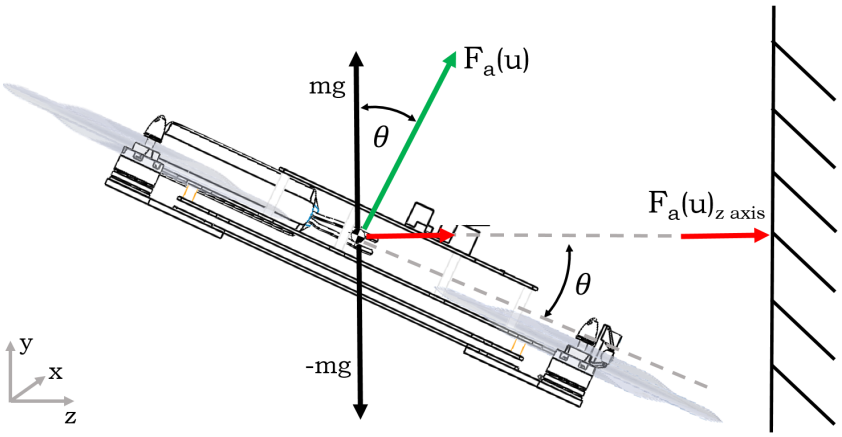

Figure 5.9: Sketch of the UAV pushing against a vertical surface via a rigid stick. The vehicle generates a force on the target surface that is proportional to its weight and pitch angle, in static conditions.

the total mass of the system interacting with the surface. In this section the focus is to evaluate what happens in the static case, as the vehicle is already in contact with the wall and the mass of the system is known in advance. It is assumed that the vehicle is in contact with the wall, pitching at an angle θ. Part of the vehicle's thrust vector $\mathbf{F}_a(u)$ is transferred to the surface, specifically its horizontal component. To retain contact with the surface for prolonged periods of time, the vehicle needs to balance out an equal and opposite reaction force and moment generating at the surface. This way, the UAV is able to cancel out such reaction forces and reach the equilibrium.

To have a qualitative estimate of the UAV's contribution towards the output force in static conditions, several calibration experiments have been performed with the same setup as the one used later on in flight experiments. Within this calibration, the system's mass and configuration are well known and they are the same which will be used later on in the experiments. The speed of approach is kept as low as possible as the UAV approaches the surface. The flying path of the vehicle is kept as short as possible, i.e. the vehicle is already in close proximity with the wall. Lastly, the manipulator's controller is disabled and the rod rigidly attached on the vehicle to mimic the conditions of Figure 5.9. The quadcopter approaches the vertical wall flying in *position* mode. Once smooth contact is established with the surface, i.e. avoiding impacts, the pitch angle is progressively increased while the force output is measured by a 6-axis Force/Torque sensor mounted on the wall. Results show that on average, the pitch angles measured by the flight controller in flight were between 5° to 17°. Forces measured by the force sensor were on average below 30 N. In Figure 5.10, a sample test is illustrated.

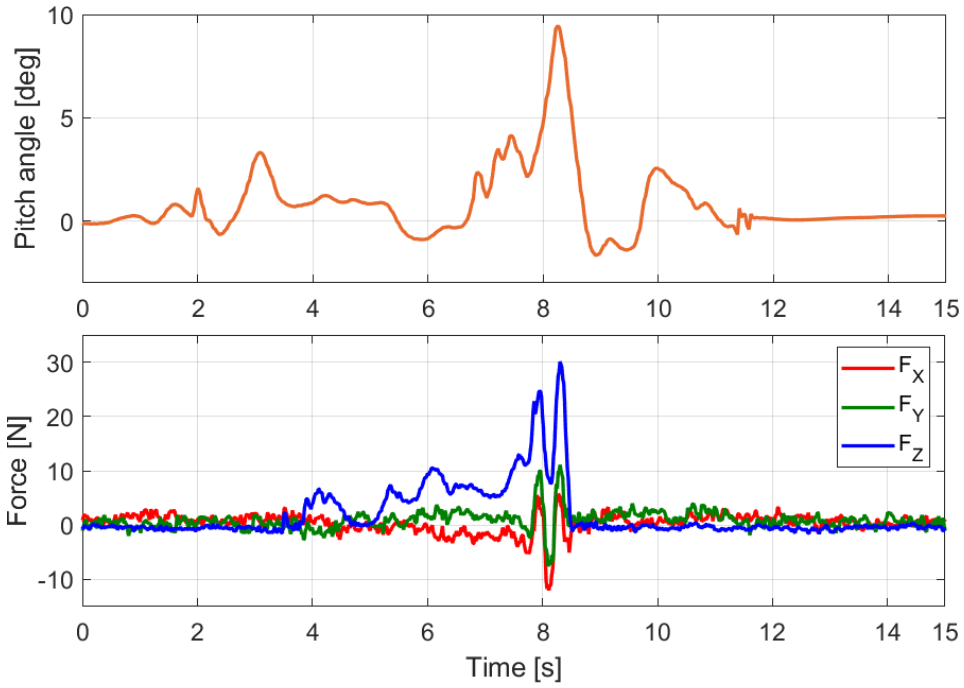

Figure 5.10: Sample flight experiment to evaluate the pitch-to-force ratio of the aerial vehicle.

It can be seen that at about t = 4 s, contact is established with the wall as a positive force is sensed. The force profile shows the lack of peaks at the beginning of the experiment (no impacts), and this reflects the attempt to perform the experiments in close-to-static conditions, as mentioned above. Contact is maintained for just over 4 seconds with the wall. After 2 seconds since the initial contact, the pitch is progressively risen to 10°. At the same time, the force sensed on the wall reaches 30 N (see blue line F_z, the axis normal to the surface), while some lateral forces are also sensed on x-y axes.

It was found that with angles higher than 5° the throttle value on the UAV would rise more quickly, generating a sudden change in the force output measured at the wall and additional perturbations in the yaw angle. This is also visible in the figure, as forces along x-y axes are more prominent as the pitch rises beyond 5°. Although the Figure above is just a sample of several experiments performed to describe the pitch-to-force mapping, this trend was consistent throughout multiple data-sets, with a force on average above 25 N at 10° and a standard deviation of ± 4.3 N.

5.5.3 Force Control

Let us consider the control problem of a mass m, i.e. the UAV, attached to a spring element, i.e. the manipulator, with stiffness k_m. The final goal is to be able to control the UAV and maintain a desired contact force $\mathbf{F}_{des}$ with the environment, which is the force acting in the spring element $\mathbf{F}_m = k_m x$. Hence, the equation that describes the physical system is:

$$\begin{aligned} \mathbf{F} &= m\ddot{x} + k_m x + \mathbf{F}_{dist} \\ &= m k_m^{-1} \ddot{\mathbf{F}}_m + \mathbf{F}_m + \mathbf{F}_{dist} \\ &= m k_m^{-1} [\ddot{\mathbf{F}}_{des} + k_{vf} \dot{e}_f + k_{pf} e_f] + \mathbf{F}_m + \mathbf{F}_{dist} \end{aligned} \tag{5.6}$$

where $\mathbf{F}_{dist}$ is the force due to disturbances, e.g. friction in the manipulator gearing, $e_f = \mathbf{F}_{des} - \mathbf{F}_m$ is the force error between the desired force $\mathbf{F}_{des}$ and the contact force $\mathbf{F}_m$. The above equation considers a close-loop system where the force output on the environment $\mathbf{F}_m$ is sensed and fed back, leading to the control law:

$$\ddot{e}_f + k_{df} \dot{e}_f + k_{pf} e_f = 0 \tag{5.7}$$

Following the method proposed by [70], one can assume that while the end-effector is in contact with the environment, its dynamics do not change over time. Accordingly, the contact forces do not change over time in static conditions, except for some small oscillations present in the system, e.g. noise. Therefore, the time derivatives terms of the force can be set as zero: $\ddot{\mathbf{F}}_{des} = \dot{\mathbf{F}}_{des} = \dot{\mathbf{F}}_m = 0$. Hence rearranging Equation (5.6) for an open-loop system and including $\mathbf{F}_{des}$ yields to:

$$\mathbf{F} = m k_{pf} k_m^{-1} e_f + \mathbf{F}_{des} \tag{5.8}$$

The aerial manipulator control architecture is illustrated in the block diagram of Figure 5.11 and follows a decentralised approach [33, 71, 72] to take advantage of the high performance embedded motor controller of the manipulator.
Starting from the left side, the desired force $\mathbf{F}_{des}$ is subtracted to $\mathbf{F}$, generating an error e_f that is the input of the proportional control law seen in Equation (5.8). The force demand is then converted into a desired current value c_{des} and inputted in the motor controller board Maxon EPOS2 24/3 that runs on a Proportional-Integral (PI) control loop. The motor board actuates the slider joint and moves the manipulator towards the target, i.e. the environment block. The position, velocity and current states at the end-effector are measured and sent to the forward kinematics block. The force exerted

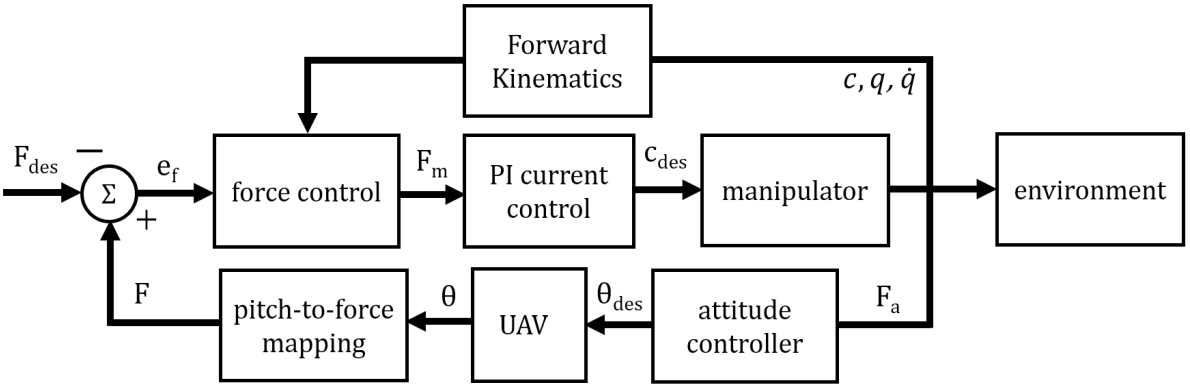

Figure 5.11: Block diagram of the aerial manipulator's control.

by the UAV pitching motion is estimated and corrected by adjusting the desired pitch angle θ_{des}, the resulting angle is then converted to force using the mapping seen in the previous section.

The *task manager* and main force controller run on the on-board Raspberry Pi 3. The internal PI current control runs on the Maxon EPOS2 24/3 digital board operating at 10 kHz. The motor states $q, \dot{q}$ are measured by the digital encoder; the vehicle relative position is measured by the distance-sensor. Both sets of data are processed by the Raspberry Pi which computes the forward kinematics and the mapping between force and current, as discussed in section [5.5.1].

5.6 Indoor Experiments

This section presents the validation of the novel aerial manipulator's design in an indoor setting. The proposed mechanical design, combined with dedicated sensing and the control laws previously discussed is tested for the installation and retrieval of smart sensors in the environment. The ability to carry out such operations on a flying vehicle can aid on-line monitoring and surveying of hard-to-reach locations and wide spread areas, without the need to build scaffolding or supporting structures. A total of 48 flight experiments are conducted to validate installation and retrieval operations indoors over a flat vertical surface. An interaction with a vertical surface already encompasses the vast majority of targeted environments where the aerial manipulator could be deployed, such as a bridge wall, a dam, a wind-turbine blade with low-curvature profile, the side of a building, and so on.

5.6.1 Experiment Outline

Each experiment is staged as follows: at first, the pilot flies the quadcopter in *position mode* towards the target whilst the on-board flight controller corrects any positioning error on the vehicle (approach stage). The use of a VICON motion capture system is employed to correct the pose estimator on the flight controller. The UAV then approaches the contact surface, i.e. a flat wooden panel, and once the vehicle is hovering in close proximity, the manipulator's task manager reads the vehicle angular states and the distance sensor measurements. If the values are within the accepted threshold, the manipulator autonomously triggers (interaction stage). On top of these requirements, an upper layer is implemented in the task manager which relies on the pilot confirming a "go-ahead" input before triggering. This input is implemented on one of the radio control switches and allows the pilot to visually check if the operation is safe to conduct. It was found that this additional safety measure allowed a more robust and repeatable behaviour over the numerous experiments carried out. This is presumably because the triggering of the manipulation system happened at the right moment thanks to the pilot's input. In the "settling" stage, the manipulator has completed the installation/retrieval task, the rack retracts and the UAV is homed.

During the interaction, force measurements are collected by a 6-axis Force/Torque sensor (Robotiq FT 300) mounted on the target surface. The sensor sampling rate is 100 Hz and provides readings up to ± 300 N on the force and ± 30 Nm on the moment. It is important to highlight that the force information from the sensor is used as a

ground-truth measurement during the indoor experiments, and not as a way to close the force control loop. Lastly, all force data presented in this section follow the convention seen in Figure 5.5, namely F_z is the force normal to the wall and it is the one to be controlled.

5.6.2 Sensor Installation Indoors

The objective of these experiments is to validate the bespoke manipulator design and control laws for installation tasks that require a considerable exchange of force with the environment. The challenge faced in these experiments is to seamlessly combine the force output of the manipulator and of the vehicle in a stable and safe way with a slow force build-up, and to be able to use this force to place a sensor securely onto a flat surface. The second challenge is to control the direction of the force to guarantee a correct installation; if the lateral component of the force is too high due to undesired yaw on the UAV, the end-effector may slip over the target inducing a sudden rotation in the system, leading to failure and potential damage to the UAV. This will be further discussed in the following section “Outdoor Experiments".

A total of 33 experiments were performed to validate installation tasks indoors. In Figure 5.12 results of a single sample flight during a successful installation are illustrated, with a focus on the range information of the distance sensor, the force generated by the manipulator, the end-effector position, and the UAV angular states. Figure 5.13 displays the force measured by the Force/Torque sensor mounted at the target during the same experiment.

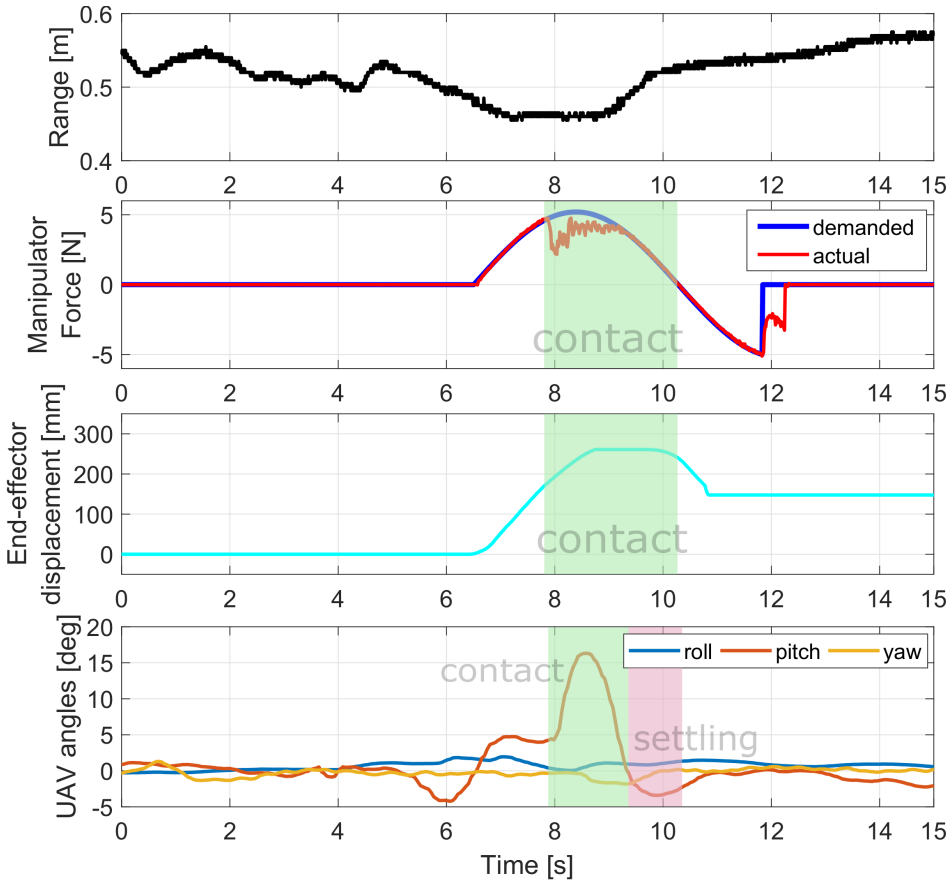

Figure 5.12: Sensor installation indoors - data collected by the on-board Raspberry Pi 3. From top to bottom: range information by the distance sensor mounted at the front of the UAV; compression force exerted by the manipulator, end-effector position and UAV angular states. The highlighted boxes delimit areas of interest, namely the contact stage and the UAV settling stage after interaction.

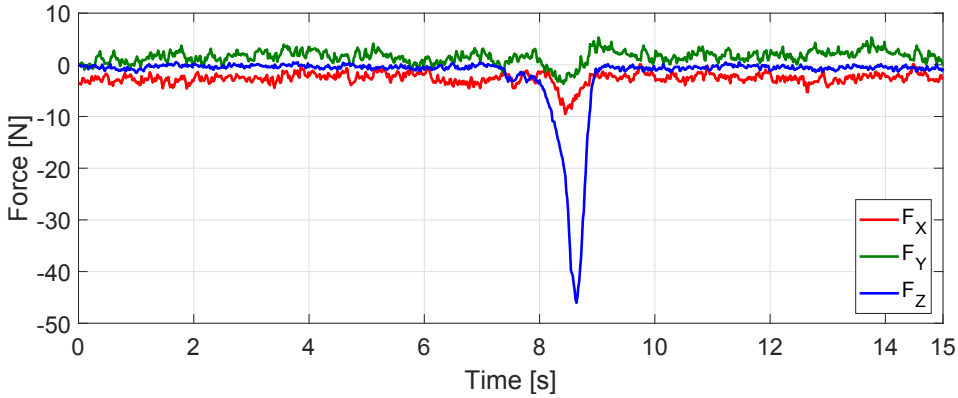

Figure 5.13: Sensor installation indoors - ground-truth measurements of the forces by a 6-axis force/torque sensor.

To begin with, the UAV approaches the target surface at a constant speed of 0.2 m/s. To install the sensor, a sinusoidal signal is used to slowly protrude the end-effector outwards. The low current that drives the end-effector outwards allows for a gentle, compliant touch with the surface and establishes a safe contact. The sensor case is provided with adhesive pads on the *wall* side to allow it to stick on the target surface. Once in contact, the force is progressively increased to ensure a sufficient adhesion of the pads and therefore secure the object in place. The manipulator's force output reaches about 5 N during the installation, whilst the highest proportion of the force output is generated by the UAV itself progressively pitching against the surface. Prior to contact, a few oscillations in pitch occur due to the turbulence in the wall proximity. However, in the majority of the cases these disturbances did not affect the positive outcome of the installation and were overall below ± 5°.

In this particular experiment, a maximum pitch angle of 16.2° is reached and a high compression force up to -46 N is sensed at the target (see Figure 5.13). As seen in the previous section, the force output is also dependant on the vehicle dynamic response when approaching the surface, i.e. speed of approach and momentum generated during the impact. These factors contribute towards higher forces resulting from each installation task. At $t \approx 9s$, the manipulator begins to retract and simultaneously the UAV's pitch angle is decreased, moving the force output F_z towards zero. At the beginning of the vehicle "settling stage", a minor overshoot below the zero is sensed in pitch as the UAV re-enters the hover state following the detachment with the target surface.

The range measurements show no drastic change throughout the dataset as the aerial manipulator approaches, installs the sensor, and homes back. This is mainly because the vehicle positioning is corrected by the flight controller in close-loop control with the motion tracking system, allowing it to adjust any sudden undesired movement due to, for example, an induced momentum. As the UAV hovers in proximity of the wall at the start of the operation, the distance from the target oscillates around 0.5 ±0.05 m, while it starts to diverge more noticeably as the rod retracts, causing a rapid change in the distribution of masses on the vehicle. In Figure 5.14 a time-lapse sequence of a single successful installation indoors is displayed.

In Table 5.5 a summary of the statistical evaluation of the overall performance of the aerial manipulator during installations indoors is illustrated, along with the success rate over the 33 attempts. Overall, 28 out of 33 installations are successful, with a failure rate of about 15%. Failure was associated with the aerial manipulator failing to secure the pad on the target surface and this was mostly due to a positioning error in *yaw*, which

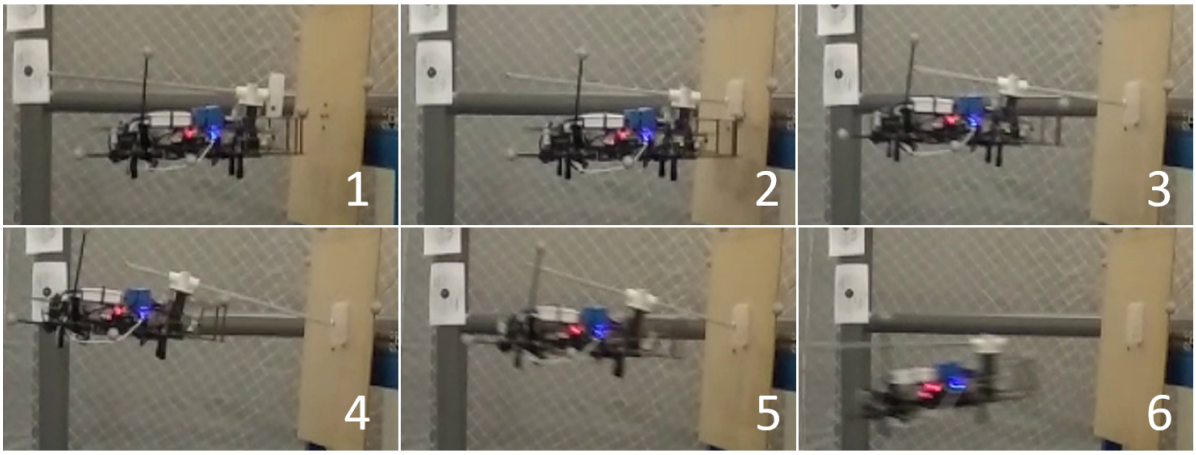

Figure 5.14: Time-lapse sequence of an aerial installation of sensor indoors.

Table 5.5: A summary of the statistics following indoors installation experiments and insights on the mean and standard deviation values of multiple variables averaged throughout the set of 33 experiments.

Sensor Installation Indoors		
Total experiments	33	
Success rate	84.8%	
$AVG\ \mu_{roll} \pm \sigma_{roll}$	0.90 ± 0.45	[deg]
$AVG\ \mu_{pitch} \pm \sigma_{pitch}$	6.91 ± 7.93	[deg]
$AVG\ \mu_{yaw} \pm \sigma_{yaw}$	0.44 ± 0.62	[deg]
$AVG\ \mu_{force} \pm \sigma_{force}$	-27.3 ± 8.94	[N]
max. force	-47.05	[N]

prevented the system from reaching the necessary *pitch* to guarantee enough adhesion of the sensor's pads on the wall.

For each flight the mean value μ and standard deviation σ for roll, pitch, yaw angles and the force output sensed at the wall are computed for both the *contact* and *settling* stages. Subsequently, the values of each variable are averaged over the total number of flights and presented in Table 5.5 as $AVG\ \mu$ and $AVG\ \sigma$ respectively. The table provides an idea of the overall trend of the vehicle stability and force output measured in the experiments. The average μ values are below 1° along roll and yaw angles and likewise the respective standard deviation σ, meaning that the angular disturbances of the aircraft during interaction are quite low and that the vehicle is stable. The pitch angle presents a higher mean value and standard deviation as expected. The average force

measured during indoor installation tasks is 27 N, while the maximum force reached in the experiments is -47 N. The standard deviation σ_{force} shows that the difference in the force output is dependant on the dynamic response of the UAV during contact and the momentum gained before the impact.

5.6.3 Sensor Retrieval Indoors

A total of 15 experiments was performed to validate indoor aerial retrieval. Within these experiments, the ability to engage with and detach an object placed on a vertical wall is validated. The challenge with retrievals is to guarantee a stable hover in close proximity to the wall, which allows the end-effector to hook the sensor in a robust way and therefore initialise the pulling motion to collect it.

To start with, the vehicle flies close to the target surface, with the end-effector extended outwards. The sensor case is already placed on the flat panel by mean of adhesive pads. As the UAM establishes contact with the surface, the manipulator is initially kept passive to ensure a compliant contact with the sensor case. As the end-tool engages with the sensor, the rack automatically retracts exerting a constant force in the opposite direction and pulling the sensor away from its environment. The manipulator's autonomous behaviour is triggered when an error in position and force is sensed at the end-effector. Results of a sample retrieval flight are illustrated in Figures 5.15, 5.16.

It can be observed that between $5.2 < t < 7.5$ s the manipulator is overcoming the adherence force of the pads to retrieve the object causing an error in the force (red line). In response to this, the force controller increases the pull and successfully collects the object. The pulling motion is also visible in Figure 5.16 where a positive tension force is measured by the force/torque sensor of about 5 N on average.

During the “retrieve" stage, the UAV generates the pulling force necessary to collect the sensor by pitching upwards, generating a nose-up pitching moment. Once the sensor is retrieved and the rack fully retracted, some oscillations generate in the vehicle in an attempt to regain the hover state. This is similar to what was seen in the previous section where perturbations in pitch are caused by the sudden detachment from the wall and rapid change in the inertia of the system. A time-lapse sequence of frames captured during a single retrieval task is displayed in Figure 5.17.

Table 5.6: A summary of the statistics following indoors retrieval experiments and insights on the mean and standard deviation values of multiple variables averaged throughout the set of 15 experiments.

Sensor Retrieval Indoors		
Total experiments	15	
Success rate	100%	
$AVG\ \mu_{roll} \pm \sigma_{roll}$	0.64 ± 0.24	[deg]
$AVG\ \mu_{pitch} \pm \sigma_{pitch}$	1.40 ± 5.27	[deg]
$AVG\ \mu_{yaw} \pm \sigma_{yaw}$	0.49 ± 0.56	[deg]
$AVG\ \mu_{force} \pm \sigma_{force}$	6.16 ± 2.04	[N]
max. force	9.23	[N]

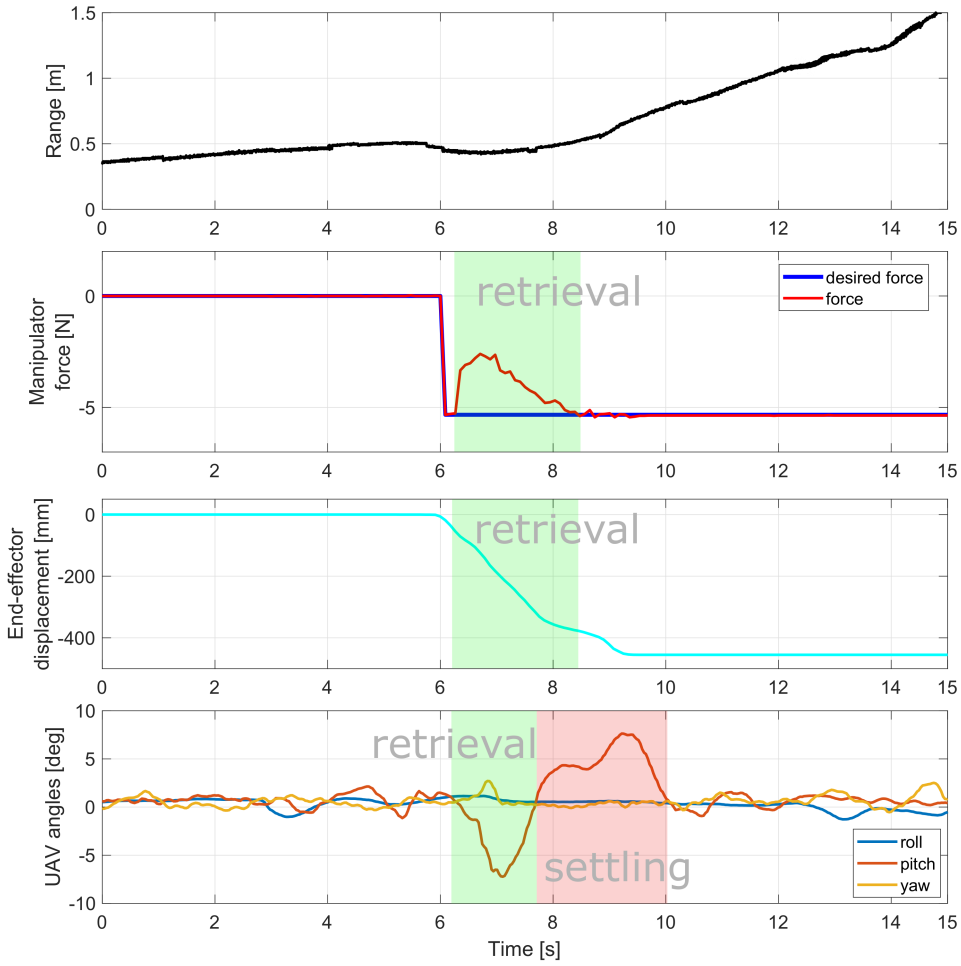

Figure 5.15: Sensor retrieval indoors - data collected by the on-board Raspberry Pi 3. From top to bottom: range information by the distance sensor mounted at the front of the UAV; pulling force exerted by the manipulator, end-effector position and UAV angular states. The highlighted boxes delimit areas of interest, namely the contact stage and the UAV settling stage after interaction.

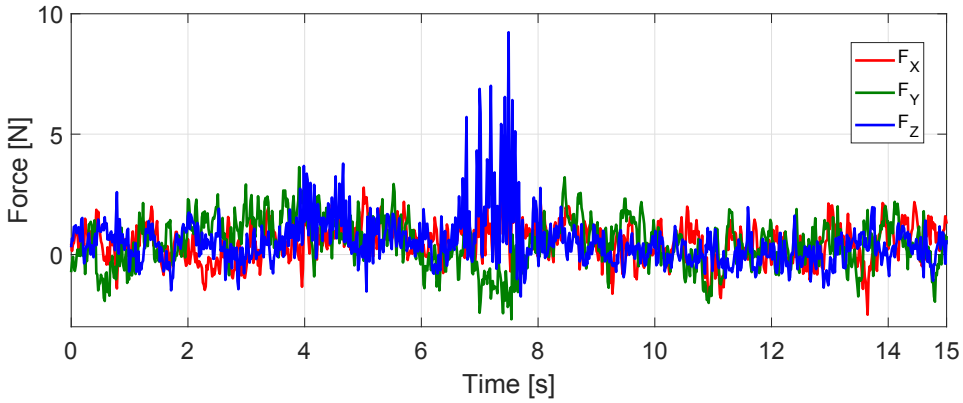

Figure 5.16: Sensor retrieval indoors - ground-truth measurements of the forces by a 6-axis force/torque sensor.

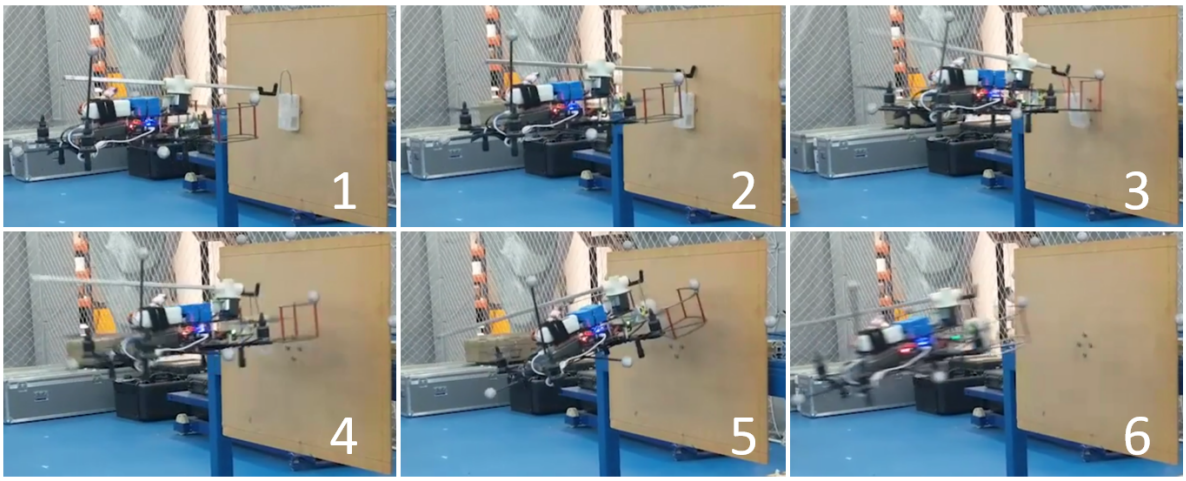

Figure 5.17: Time-lapse sequence of an aerial retrieval of sensor indoors.

In Table 5.6 a summary of the statistical evaluation of the aerial manipulator performance during retrievals indoors is illustrated. Overall, 15 out of 15 retrieval experiments were found to be successful. The values $AVG\ \mu$ and $AVG\ \sigma$ are the mean and standard deviation of the angular states and the force averaged over the total number of flights. The average pitch angle, namely $AVG\ \mu_{pitch}$, measured during retrieval operations is below 10° and shows that a lower force is necessary to pull the sensor away from the than the one necessary to install it. From the table it can be noticed how the angular disturbances in *roll-pitch-yaw* are generally lower than those found in the installation experiments. This is attributed to the nature of the operation itself which requires a less dynamic response and proves overall less challenging to handle from the UAV perspective. Likewise, the maximum force measured by the force/torque sensor is 9.23 N showing that the UAM dynamics involved in these tasks are less demanding than those

seen in the previous section.

5.7 Outdoor Experiments

A total of 41 outdoors experiments were performed outdoors to test the proposed aerial manipulator in more complex conditions. Typically the majority of aerial applications for UAMs includes the interaction with vertical or tilted surfaces of different materials, however the ability to perform installations on more challenging surfaces is tested to further validate the robustness of this approach. In particular, cylindrical irregular surfaces such as tree trunks are chosen for the following outdoors experiments, as they resemble one of the most challenging targets for aerial manipulators to interact with, due to their irregular shape and texture. The experiments are performed on a range of several trees with the purpose to install and retrieve small sensors, such as smoke detectors, to prevent forest fires or to achieve real-time monitoring and surveying.

Flying outdoors brings additional challenges such as accurate position sensing and the presence of unknown obstacles that can generate turbulence over the vehicle. The purpose of these tests was therefore to demonstrate if placement and retrieval is in essence feasible and to identify the best approach to take in order to improve reliability.

5.7.1 Experiment Outline

The experimental setup used for outdoors experiments is similar to the one seen previously, except for the lack of motion capture system reading the UAV states, and the Force/Torque sensor measuring the contact force on the tree trunks. The lack of the VICON tracker reduces the accuracy in the vehicle's pose estimation, which only relies on the use of an on-board GPS. Due to the partial occlusion of the GPS signal in the proximity of tree branches and other obstacles, the flight controller pose estimator experiences a higher level of noise as opposed to open-field flying. An additional precaution taken in this respect was to lower the flight controller gains to have less aggressive flight manoeuvres.

5.7.2 Sensor Installation Outdoors

In Figure 5.18 results of a single sample flight during a successful installation are illustrated. For outdoors experiments, the *current* input used to extend and retract the end-effector was generally lower when compared to the indoors flights. This was chosen

so as to increase the compliance of the end-effector when in contact with the tree and to have a less aggressive behaviour. Moreover, the sinusoidal signal in force has a shorter period compared to the previous section. This is because the duration of the contact is reduced and the force output is tailored for outdoors experiments to perform a safer interaction and account for sudden disturbances in the position estimator. Once contact is established, the UAV progressively increases its pitch to generate a good adhesion on the object, then flies backwards after a successful placement.

Results are illustrated in Figure 5.18. The second figure from the top shows the manipulator's force during the task: contact with the tree occurs at $t = 7$ s, where the impact of the object on the target surface generates a force error in the controller. During this time, the manipulator is still extending (see third figure). As the object is installed and the UAV retrieves the loiter state, disturbances in *pitch* and *yaw* generate, as seen in the bottom figure (settling area).

A general trend experienced in outdoors experiments is the longer settling time needed by the UAV to retrieve the hover state and higher disturbances sensed in *pitch* and *yaw*. As previously discussed, one of the major factors that plays a role in pose estimation is the use of GPS over the VICON motion tracker, which affects the positioning accuracy. Another potential source for a longer settling time and higher angular disturbances is the presence of gusts and other obstacles that induce turbulence, e.g. surrounding trees, branches. Despite these factors, the "settling stage" had minimal effect on the overall success rate of the outdoors trials, with the main cause for failure assigned to an undesired yaw during contact that induced slippage at the end-effector. The undesired yaw generated a lateral force at the end-effector causing it to move out of the interaction plane$y$-z, slipping over the trunk and therefore not generating enough adhesion on the sensor adhesive pads.

In Table 5.7 a summary of the statistical evaluation of the overall performance of the aerial manipulator during installations outdoors is illustrated, along with successful rate throughout the 23 attempts. Overall, 18 out of 23 installations were successful, with a failure rate of about 21%. As experienced in the indoor setting, failure was attributed to an undesired yaw which caused slippage of the end-effector on the target surface, even more so as the target is a cylindrical surface. The table here presented follows the same notation as the ones seen above, where $AVG\ \mu$ and $AVG\ \sigma$ show the averaged mean and standard deviation values for multiple variables and give an idea of the overall trend of the vehicle stability measured in the experiments, validating the repeatability and robustness of this approach.

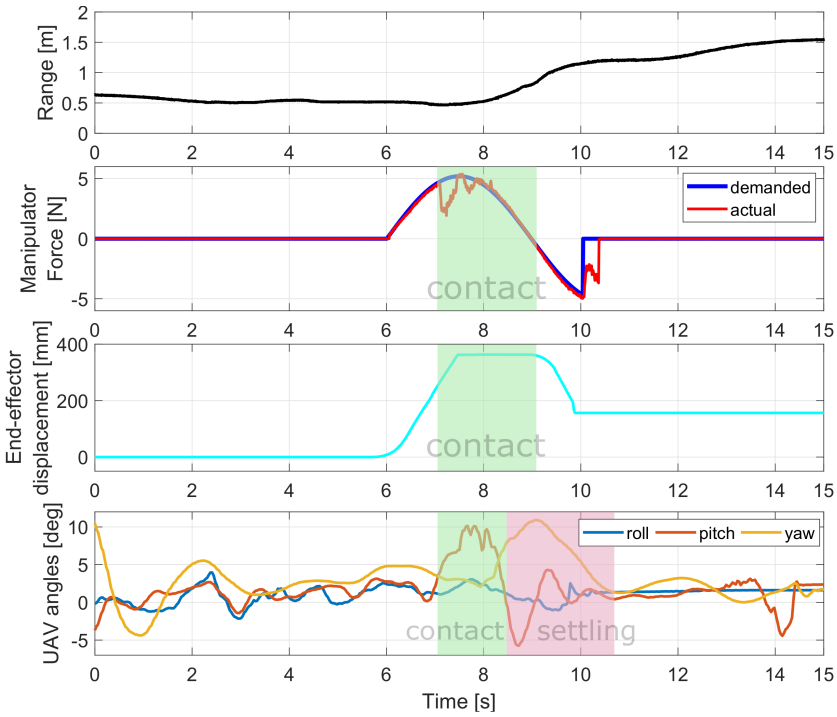

Figure 5.18: Sensor installation outdoors - data collected by the on-board Raspberry Pi 3. From top to bottom: range information by the distance sensor mounted at the front of the UAV; pushing force exerted by the manipulator, rack displacement and UAV angular states.

It can be seen that the larger variations in yaw experienced during outdoors experiments are recorded within the mean μ_{yaw} and standard deviation σ_{yaw}, as these values appear to be larger than in previous cases. The pitch angles reached during installation are lower than those seen in the indoor setting, and this reflects in lower mean and standard deviation values. This is because, as previously discussed, the time of contact with the tree was reduced with respect to indoor trials, hence the pitch “build-up" is also lower. Overall, the pitch angle reached during outdoors installations ranges between [5°,12°]. A time-lapse sequence of frames captured during a single installation task outdoors is displayed in Figure 5.19.

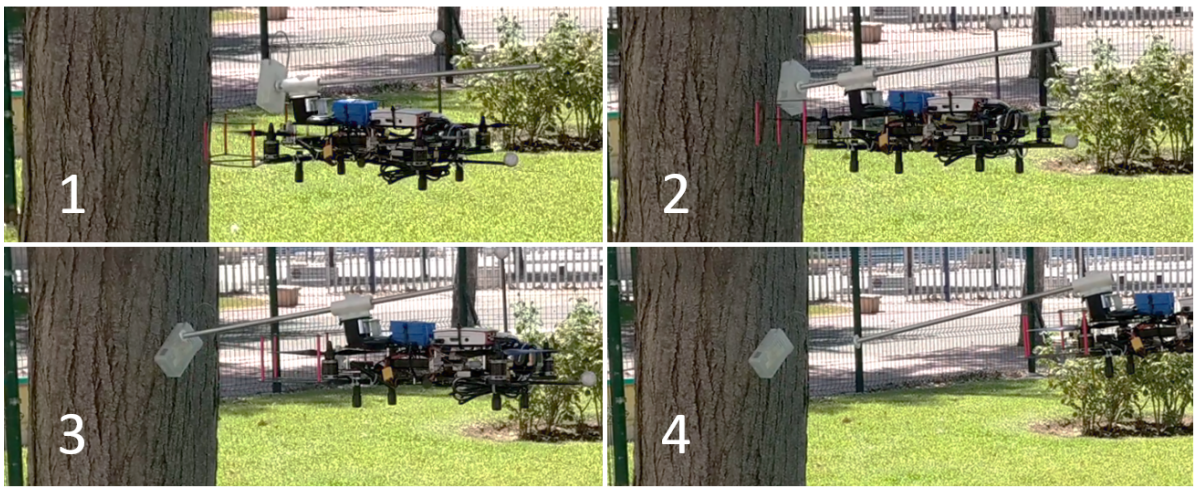

Figure 5.19: Time-lapse sequence of an aerial installation of sensor outdoors.

Table 5.7: A summary of the statistics following outdoors installation experiments and insights on the mean and standard deviation values of multiple variables averaged throughout the set of 23 experiments.

Sensor Installation Outdoors		
Total experiments	23	
Success rate	78.2%	
$\mu_{roll} \pm \sigma_{roll}$	1.07 ± 1.27	[deg]
$\mu_{pitch} \pm \sigma_{pitch}$	3.57 ± 5.02	[deg]
$\mu_{yaw} \pm \sigma_{yaw}$	4.60 ± 2.90	[deg]
estimated avg. force	-22	[N]

5.7.3 Sensor Retrieval Outdoors

Outdoor retrieval experiments were carried in the same way as indoors. Results are shown in Figure 5.20. In general, the same challenges as the indoor setting were present, however the GPS-based flight made long-term stable hovering in the proximity of the target more challenging outdoors as opposed to indoors. Also, the UAV settling time was also found to be longer, as with outdoor installations. Often, the pitch angle oscillates between [-10°,10°] after retrieving the object from the wall, with oscillations also present in yaw. As seen before for the indoor retrieval, the angular disturbances generate from the detachment with the tree as well as the end-effector retracting motion, causing a sudden change in the momentum of the vehicle. Despite these oscillations, the overall success rate in outdoors retrievals is 100% over 18 experiments performed, demonstrating a

higher repeatability than outdoors installations. This is a result that was also found in the indoor setting: the nature of the retrieval task itself leads to a higher robustness during interaction, as it requires a less aggressive and less dynamic behaviour on the flight controller to complete the task. A time-lapse sequence of frames captured during a single installation task outdoors is displayed in Figure 5.21.

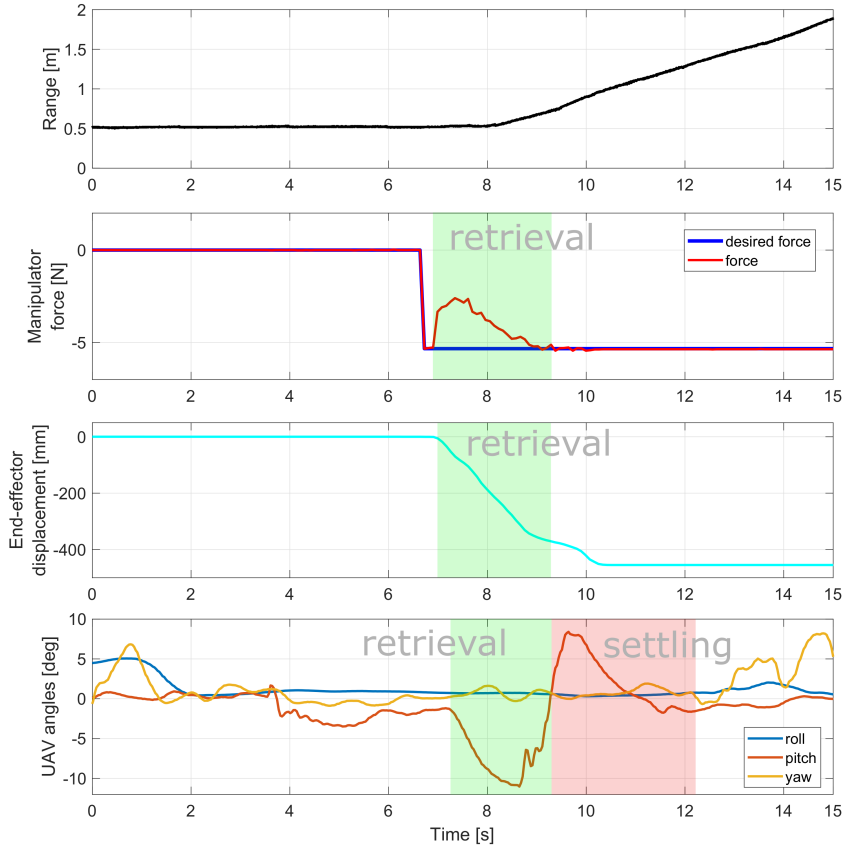

Figure 5.20: Sensor retrieval outdoors - data collected by the on-board Raspberry Pi 3. From top to bottom: range information by the distance sensor mounted at the front of the UAV; pulling force exerted by the manipulator, rack displacement and UAV angular states.

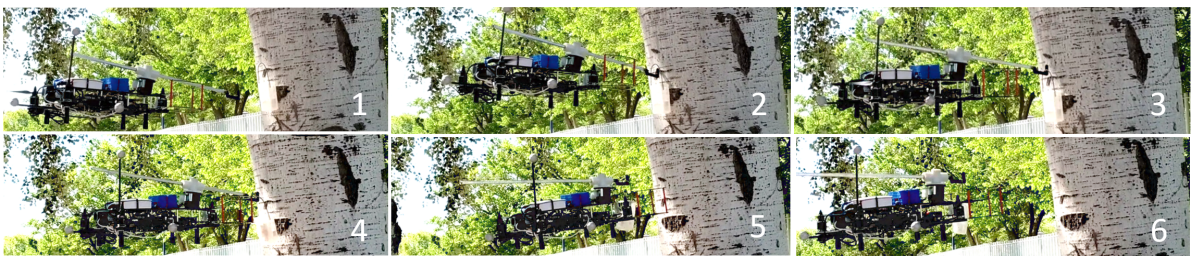

Figure 5.21: Time-lapse sequence of an aerial installation of sensor outdoors.

Table 5.8: A summary of the statistics following outdoors retrieval experiments and insights on the mean and standard deviation values of multiple variables averaged throughout the set of 18 experiments.

Sensor Retrieval Outdoors		
Total experiments	18	
Success rate	100%	
$\boldsymbol{\mu_{roll} \pm \sigma_{roll}}$	0.32 ± 0.27	[deg]
$\boldsymbol{\mu_{pitch} \pm \sigma_{pitch}}$	1.37 ± 4.42	[deg]
$\boldsymbol{\mu_{yaw} \pm \sigma_{yaw}}$	0.45 ± 3.95	[deg]
estimated avg. force	6.4	[N]

In Table 5.8 a summary of the statistical evaluation of the overall performance of the aerial manipulator during retrieval tasks outdoors is illustrated, along with successful rate throughout the 18 attempts. Overall, the angular disturbances were significantly less than those in installations outdoors. Disturbances in the *pitch* and *yaw* are still present, due to the turbulence caused by the propellers moving close to branches and the trunk. However, such disturbances did not affect the positive outcome of the retrieval operations, and all attempts were successful.

To conclude, outdoors experiments demonstrated the feasibility and robustness of the proposed approach for both placement and retrieval tasks. The conclusions drawn from these experiments showed that a stable hover, lower gains of the flight controller and a lower magnitude of the demanded force were the key elements to succeed in the outdoor setting. On the aerial vehicle side, lowering the gains and the demanded pitch angle allowed a safer and less aggressive interaction, and helped compensating for low-accuracy pose estimation. On the manipulator side, lowering the force demanded by the manipulator and the period of application of the force allowed to shorthen the time in contact with the tree and lowered the risk of failure due to latency in the pose estimation under the tree branches. The combination of all these factors proved that outdoor operations were possible and repeatable, where a total of 41 data-sets were produced.

5.8 Conclusions

To address aerial installation and recovery of smart sensors in the environment, a small-sized UAV equipped with a lightweight, compact manipulator is presented in this chapter. The mechanical design, sensing and the electronics of the refined manipulator have been discussed in detail, along with the control approach to tackle such operations. The strength of this design lies in the simplicity of the transmission mechanism and its minimal weight which make it a suitable modular solution for on-site inspection with different aerial platforms.

The proposed UAM is ideally suited for force-driven aerial tasks such as the placement and retrieval of objects, NDT and contact-based inspection. A total of 89 data-sets was produced to demonstrate the reliability and robustness of this approach and the following lessons have been learned:

- devising a manipulator that is adequate for the task is a key design requirement and it unfolds in several sub-requirements such as minimising the payload, addressing the weight distribution and refining the configuration/integration on the aerial vehicle. These are all essential elements that improve the dynamic response of the flying robot whilst interacting with a surface;

- distance sensing on the aerial manipulator is beneficial and it can be used to automate the operation, however it is of limited use during the interaction and the settling stages. Other forms of visual sensing or event-based cameras could be incorporated to further improve sensory feedback on-board and refine the autonomous behaviour;

- real-time force control has proved to be a reliable approach for the specific application of object placement and retrieval, and the validation in the outdoor setting has shown its versatility and potential for other force-induced tasks;

- force sensing is essential to inform the platform on how the interaction is affecting the system's variables, and it allows to achieve closed-loop control over the force;

- indoor experiments demonstrate the effectiveness of the approach in a monitored environment, with accurate pose estimation over the vehicle. Results showed that the UAM is capable of dynamically adjust its angular states whilst in contact with the surface and to combine the force output generated by the active manipulator and by the UAV's pitching motion. This allows the aerial manipulator to generate

a force-to-weight ratio of 130% on average during installations, with a maximum force of 230% its weight;

- outdoor experiments demonstrated good reliability of the proposed aerial manipulator in more challenging conditions and with less accurate pose estimation of the vehicle. Lower gains on the flight controller ensured a more gentle and compliant approach and helped to handle the uncertainty of the outdoor setting, for example GPS signal occlusion. Lower force outputs were demanded on the aerial system, resulting in a less aggressive dynamic response. This ensured a safer interaction with the tree;
- the proposed UAM has the ability to interact with different targeted environments, such as flat vertical surfaces and irregular cylindrical surfaces, demonstrating repeatable outcomes and robustness even in more challenging conditions.

To conclude, the work presented in this chapter aims at demonstrating the capabilities of the proposed lightweight compliant manipulator for force-driven aerial tasks such as the installation and retrieval of smart sensors in the environment, and it lays the foundations towards more dexterous force-driven aerial tasks.

Future work will look at ways to expand the range of applications with the present design, as well as new control strategies tailored for contact-based aerial applications.

CHAPTER 6

AN AERIAL MANIPULATOR FOR CONTOUR FOLLOWING: TOWARDS TACTILE-BASED AERIAL NAVIGATION

Publications

This chapter has resulted in the following peer-reviewed research outputs:

1. Hamaza S., Georgilas I., Richardson T. (2019) Energy-Tank Based Force Control for 3D Contour Following. In *Towards Autonomous Robotic Systems* (K. Althoefer, J. Konstantinova, and K. Zhang, eds.), (Cham), pp. 41–51, Springer International Publishing, 2019. [73]

2. Hamaza, S., Georgilas, I., and Richardson, T. (2019, November). 2D Contour Following with an Unmanned Aerial Manipulator: Towards Tactile-Based Aerial Navigation. In *2019 IEEE/RSJ International Conference on Intelligent Robots and Systems (IROS)*, IEEE. [74]

Manipulation has been at the centre of the state of the art of robotics research for over forty years. However, it wasn't until 7 years ago that the research community had raised an interest in the development of manipulation capabilities for unmanned aerial vehicles. As it was seen in the previous chapters, several challenges are faced by the mobile floating platforms when interacting airborne, mainly caused by

the instability generating on the vehicle when exchanging forces and moments in the environment.

In this chapter a passivity-based control approach using energy-tank methods is explored as a possible solution to prolonged interaction between the aerial manipulator and a surface. Such approach is implemented for contour following applications, and it is particularly suited for aerial systems interacting with unknown structures. The combination of force-tracking with the inherent compliance of the energy-tank method allows to safely exert known forces and interact with un-modelled environments.

The envisioned aerial application for such contour following capabilities is to aid indoor navigation of UAVs, for example in a search and rescue scenario. Often UAVs are deployed to inspect wrecked buildings after an earthquake or other natural calamities, having only to rely on cameras and visual SLAM (Simultaneous Localisation and Mapping) to navigate in such indoor setting. Signal occlusion on the GPS tracking is also a recurring limitation in indoor navigation which needs to be accounted for. Including active tactile feedback on the aerial platform can provide a more robust way to safely operate in poorly lit environments, or areas where visual sensing is simply not enough. Therefore, contour following becomes a useful property that aerial manipulators could exploit, for example, to detect crevices and doorways in which the UAV can fly into.

The main contribution highlighted in this chapter lies in the novel approach to contour following with the use of an aerial manipulator controlled by an energy tank-based force controller. The control laws have been tailored for the 1-DoF manipulator and integrate the aircraft states resulting in closed-loop control within the manipulator

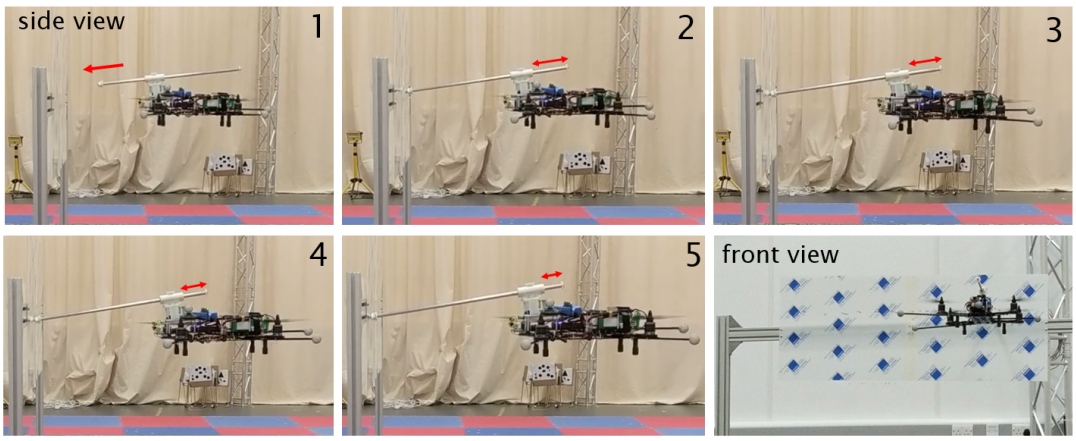

Figure 6.1: A sequence of frames captured during flight experiments show a side view of the aerial system whilst exerting a shear force along a 1.25 metres surface by means of a 1-DoF manipulator. The last frame shows a front view of the same experiment.

itself. Two sets of experiments contribute to show the validity of this approach, both on a stationary/fixed platform and on a mobile one. Successful force-tracking and continuous contact are demonstrated in the experiments, where the manipulator actively adjusts the end-effector's position to deliver a continuous force on the target surface, in both 2D and 3D cases. Reliability and robustness of this approach are therefore demonstrated, showing the potential of this for more complex contour following tasks.

This chapter is laid out as follows: at first some background information on the design of passivity-based methods is discussed, along with some of the key strategies found in the literature to tackle compliant interaction. Then, the modelling and control laws of the proposed energy tank-based controller are discussed. Follows a brief section on the newly developed end-effector design, tailored for contour following applications. Two sets of experiments are then presented: stationary experiments and aerial experiments. The former are aimed at validating the control approach, testing its effectiveness over unknown 3D profiles, on a stationary base. The data-sets collected during aerial experiments are then presented, where the proposed control approach is tested for contour following operations over a 2D surface. Results are discussed in conjunction with the analysis of both the manipulator and aircraft performance. Lastly, the lessons learned from this work are summarised in the conclusions section.

6.1 A Brief Review on Interaction Control

Interaction control strategies can be sub-categorised into *direct* and *indirect* force control. The direct approach achieves the force regulation of the end-effector by adopting an integral action on the force error [75, 76]. Such error is often generated by an outer force loop, i.e. a force feedback loop. On the other hand, indirect force control is based on impedance and compliance control where the output force is the result of an inner motion loop; without the explicit closure of the force loop.

Manipulation control strategies have often been tailored for fixed robots, e.g. industrial robotic arms for assembling purposes. In the works presented in [77, 78] a constrained-based approach that allows to selectively control force, impedance and position has been proposed. The former combines the estimation of geometric uncertainty into the instantaneous task specification and allows for compensation of time-varying coordinates on the end-effector. The latter extends on the to task specification geometry requirements to a guarantee a smoother and more robust indirect force control.

Berensan at al. present several works on constraints-based interaction control. In

[79] a Constrained Bi-directional Rapidly-Exploring Random Tree (CBiRRT) algorithm takes into account a variety of constraints in manipulation planning including the motors' torque, the pose of the object manipulated, and workspace surfaces. This method expands to ways to configure the space manifolds that correspond to constraints, and solves the planning by knowing the allowable error for meeting a constraint. The control is successfully validated on a 7 DoF robotic arm for complex tasks. Similarly the work in [80] evaluates the CBiRRT method with different strategies to intersect and chain the Task Space Regions for more complex tasks.

Projection methods have also arisen in the context of interaction controls and inverse kinematics. Iterative inverse kinematics algorithms use projection methods based on the pseudo-inverse or transpose of the Jacobian to consequently move the robot's end-effector closer to some desired workspace transformation [81]. In the work presented by Sentis and Khatib's [82], a potential-field approach uses recursive null-space projection to synthesise whole-body behaviours by aggregating multiple (behavioural) primitives and establishing a control hierarchy amongst categories, i.e. constraints, operational tasks, and postures.

Hybrid position/force type of controllers gained popularity since their formulation three decades ago, as they allow to work in force and motion sub-spaces that are complimentary to each other in conjunction with the task specification. Despite the versatility of the hybrid approach, the major drawbacks are associated with the need for an accurate modelling of the contact properties *a priori* to achieve a good performance, and the lack of robustness during contact-loss [83].

In 2015, Schindlbeck et al. present a unified method combining force and impedance control via energy-tank, with a particular focus on contact loss compensation [84]. The method is tested on a KUKA robotic arm and it proves useful in force tracking applications over 3D surfaces, coping with contact discontinuities within the target surface. Similarly, Ferraguti et al. propose an energy tank-based method for tele-operated robotic surgery applications [85, 86]. To address these operations, a passivity-based interactive control architecture is implemented to tackle time-varying interactive behaviours, combined with a two-layered bilateral control to ensure stability within the transition between autonomy and tele-operation. Preliminary experiments are conducted on a semi-autonomous surgical robotic systems, showing the potential of the energy approach for the interaction with soft tissues.

Stramigioli et al. also make use of a passivity-based interaction controller combining energy and power-based norms to ensure safety and compliance of domestic robots [87].

The controller works by analysing the energy and power flow of a standard impedance-controlled manipulator, a combined energy and power safety metric is calculated for on-line adjustments of the controller parameters. To ensure continuous passivity during the instantaneous modulation of the controller's parameters, an energy tank-based implementation was used. Simulation and experimental results on a 1-DoF manipulator indicate a good trade-off between safety and performance overall.

In [88] a unified energy-based modelling and control framework for robotic systems is proposed. Such framework is formulated to be applicable to any robotic system in which the energy transfer between sub-systems is made explicit. The architecture considers the separation of a high-level supervisory control loop, and a lower-level actuation controller. By implementing energy "budgets" on the actuation controller, stability is guaranteed through passivity even when latency between sub-systems occurs. Experiments validate the proposed method for stable control of a tele-operated five-bar linkage system, and compare the performance with a traditional controller.

Following the works presented above, the work described in this chapter proposes a force control architecture that includes the concept of energy tanks for stable and prolonged force-tracking as seen in [85, 86]. This approach is believed to be suitable for tackling the contact loss condition, as its effectiveness was demonstrated by [84]. During aerial interaction, contact loss is a scenario that can easily occur due to, for example, gusts, drifting of the vehicle, inaccurate pose estimation of the aircraft, and so on. It was found in the previous chapter that pure force tracking with the lack of an on-board force sensor can lead to instability of the UAV, brought by loss of contact with the surface.

In fact in any open-loop scheme, the manipulator would attempt to deliver the force output regardless contact with a surface is established [76]. This results in an undesired motion at the end-effector, which may lead to instability of the vehicle, and a sudden change in the moment of inertia. Despite there were cases in the experiments of chapter 5 in which such condition was triggered without major causes to the UAV, the objective in this chapter is further enhance the compliance and safety of the aerial system to address interaction with unknown surfaces and contact loss. This approach could be particularly suitable for aerial contour following operations over 2D surfaces, and it represents the first step towards tactile-based navigation in the aerial manipulation's state of the art.

6.2 Control

6.2.1 Force Control Design

Let us start by introducing force-tracking control designed for the manipulation system, using a Proportional-Integral approach. The motor torque τ_m is directly proportional to the Jacobian matrix of the system as follows:

$$\tau_m = J^T(\mathbf{q})\Big[k_p\Big(F(t) - F_d(t)\Big) + k_i \int_0^t \Big(F(t) - F_d(t)\Big)dt\Big] \tag{6.1}$$

where J^T is the transpose of the Jacobian matrix which only depends on the manipulator's configuration, i.e. the vector of generalised coordinates $\mathbf{q} \in \mathbb{R}^n$. Terms $F(t)$ and $F_d(t)$ are the time-varying force and desired force values respectively, and k_p and k_d the proportional and derivative gains respectively.

The use of brushless DC motors as actuators of the manipulator's joints allows to exploit the linear relationship between the input current and output torque, as previously discussed. Hence, rearranging the above equation leads to:

$$\tau_m = J^T(\mathbf{q})\Big[K_T\big[k_p\big(c(t) - c_d(t)\big) + k_i \int_0^t \big(c(t) - c_d(t)\big)dt\big]\Big] \tag{6.2}$$

where the parameter K_T is the motor's torque-current constant and it is provided by the motor's manufacturer, $c(t)$ and $c_d(t)$ are the input current and desired current respectively. This equation describes direct force-tracking exploiting the current-to-torque linear relationship of DC motors, and it can be extended to any n-DoF manipulation system that employs similar actuators.

6.2.2 Energy Tank Design

Energy tank-based methods have frequently been used for tasks concerning tele-operated manipulation [89–91], but also as an addition to impedance control with variable stiffness [85]. The role of the energy tank is to act as a virtual storage element and minimise the energy dissipation of the controlled system. Such energy represents the *passivity threshold* used by the force controller, and the tank being its reservoir. In essence the tank allows to act upon the impedance of the system by monitoring the amount of energy dissipated during the task and amending the output force accordingly. The tank energy is:

$$T(x_t) = \frac{1}{2}x_t^2 \tag{6.3}$$

where the variable $x_t(t) \in \mathbb{R}$ is the state associated with the tank, with the condition of $x_t(0) > 0$. Now, the dynamics are given by:

$$\begin{cases} \dot{x}_t = \dfrac{\beta}{x_t}\left(\dot{\tilde{x}}^T D_d \dot{\tilde{x}} \right) + u_T \\ \tilde{x}(t) = x(t) - x_d(t) \\ u_T = -w(t)^T \dot{\tilde{x}}_t \end{cases} \tag{6.4}$$

where $\dot{x}_t$ is the time derivative of the tank state, $\tilde{x}$ represents the error between desired and actual states. The term $w(t)$ represents the tank control input, and lastly β is defined as:

$$\beta = \begin{cases} 1 & \text{if } T \leq T_{upper} \\ 0 & \text{otherwise} \end{cases} \tag{6.5}$$

β is a design parameter that enables the storage of dissipated energy as long as the total tank energy is below its upper bound T_{upper}. Differently, if the tank energy is greater than T_{upper}, β becomes zero and the tank is disabled. This condition allows to prevent excessive storage. The product ($\dot{\tilde{x}}^T D_d \dot{\tilde{x}}$) represents the power dissipated. The tank control input $w(t)$ is defined as:

$$w(F_{ext}, t) = \frac{\alpha}{x_t}\left(k_p(F_{ext} - F_d) - k_i \int_0^t \left(F_{ext}(t) - F_d(t) \right) \right) \tag{6.6}$$

Therefore the extended motor dynamics can be rewritten as:

$$\tau'_m = J^T(\mathbf{q}) \frac{\alpha}{x_t} \left[k_p(F_{ext} - F_{des}) + k_i \int_0^t (F_{ext} - F_{des}) \right] \tag{6.7}$$

where α is defined as:

$$\alpha = \begin{cases} 1 & \text{if } T \geq T_{lower} \\ 0 & \text{otherwise} \end{cases} \tag{6.8}$$

where $T_{lower} > 0$ represents the lower bound below which the energy cannot be extracted by the tank, leading to $\alpha = 0$ and preventing singularities to occur.

6.2.3 Case Study: Contact Loss

Contact loss can be a recurring scenario during manipulation with an unmodelled environment, even more likely to occur if the interaction is performed on-board of a UAV. Aerial vehicles tend to be unstable in the proximity of obstacles, leading to

disturbances that often generate altitude loss and drifting. Therefore, it is essential that a manipulator intended for aerial applications is able to cope with contact loss, preventing it from executing unsafe motions.

Typically, manipulators that are solely controlled for force-tracking behave by applying the desired force F_{des} regardless of whether or not the contact with the environment is established. The tank-based design brings an improvement to pure force-tracking as the output force is regulated until the tank energy is drained and the lower bound T_{lower} is reached. However, depending on the remaining energy in the tank, undesired substantial and rapid motion can still occur.

To address contact loss a port-based control architecture is hereby proposed, where the controller is switched on and off depending on the contact information sensed at the end-effector. This port-based model works by reading the end-effector states, i.e. position, velocity and current/force, and computing the overall kinetic and potential energy of the manipulator at any given time. During contact loss the output energy quickly reaches higher values as it is dependent on the square of the velocity $\dot{\mathbf{x}}_\mathbf{t}$. Once the saturation point is met, a signal is sent to the energy-tank control block that forces its drainage by setting $\beta = 0$ (see Equation (6.5)). As a result the controller output is set as zero. In Figure 6.2 a control block diagram of the passivity-based force control via Energy-Tanks model is illustrated.

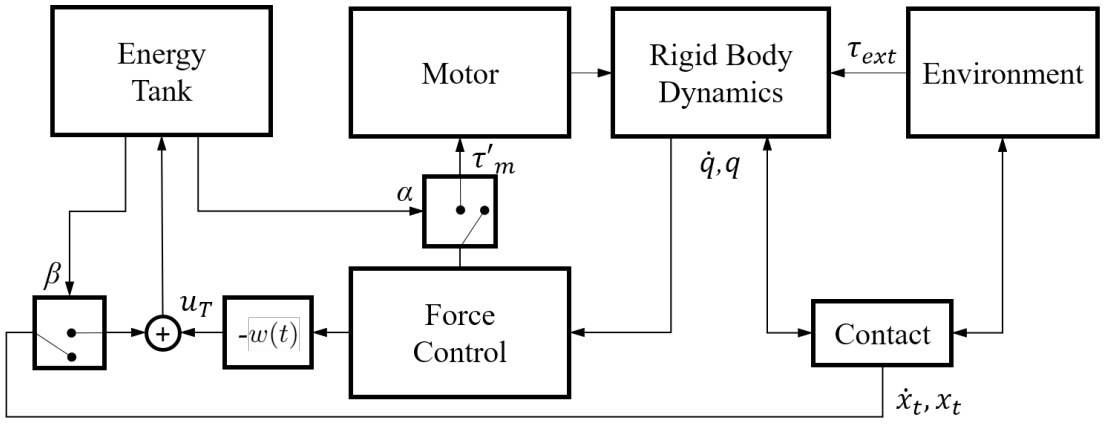

Figure 6.2: Block diagram of the proposed force controller via energy-tanks.

6.3 End-Effector Design

To address contour following application, the aerial manipulator's mechanical design was left as it was (see section 5.1 for further details), and the only changes were brought to the

end-effector. To minimise friction at the contact point and guarantee smooth contouring on uneven surfaces, e.g. surfaces with indents or lumps, a ball caster is mounted at the tip of the rack. This solution is selected as it reduces the contact surface to a single point during interaction, therefore zeroing the moments of the external wrench τ_{ext} leading to pure force exchange F_{ext}. The ball caster's material is metal and has a diameter of 15 mm. A CAD drawing of the linear actuator with the proposed end-effector is illustrated in Figure 6.3.

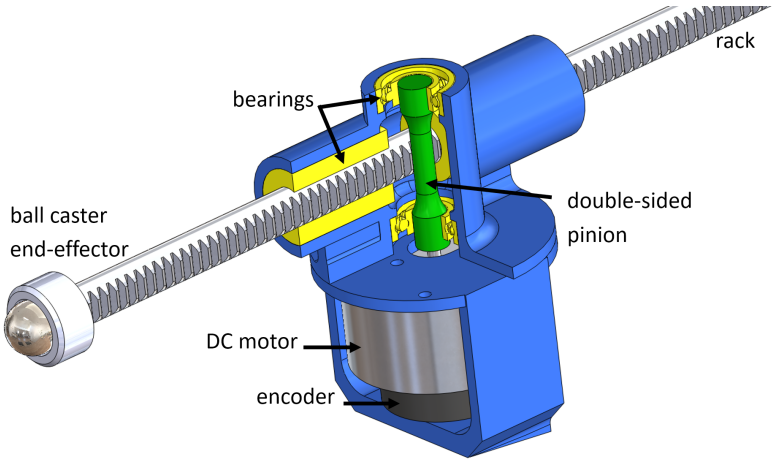

Figure 6.3: CAD drawing of the manipulator's transmission mechanism and the new end-effector solution.

6.4 Stationary Experiments

6.4.1 Experimental Setup

The setup used to validate the proposed control architecture includes the 1-DoF manipulator presented earlier mounted on a stationary base; a 6-axis force/torque sensor to measure the output force and the target surface to contour follow. The sensor chosen is the Robotiq FT 300, sampling at a rate of 100 Hz. The sensor data act as ground truth measurements, as opposed to a feedback for the controller loop. In fact, the estimated force on the end-effector is directly derived from the current information through the

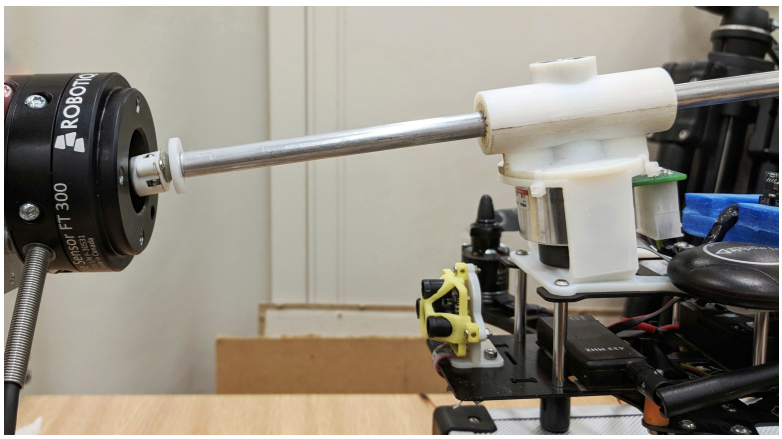

Figure 6.4: Experimental setup: 1-DoF manipulator equipped with a friction-less end-effector, exerting force over a 6-axis Force/Torque sensor.

use of the torque constant K_T (see Section 6.2.1). Figure 6.4 illustrates a snapshot of the setup during the experiments with a close up on the 1-DoF manipulator in contact with the sensor.

6.4.2 Results

Several experiments are conducted to validate the proposed passivity-based force control with energy tank. For each experiment, a different 3D profile with curvatures of different radius spanning from 1cm to 10 cm was contoured to validate the robustness of the control approach. The experiments aim to validate the ability to:

- 3D contour follow an unknown surface;
- establish a force pushing forwards whilst in contact;
- respond to an external input from the environment (τ_{ext}) in a compliant/ passive way;
- cease any force/motion as contact loss with the target is sensed;
- show the robustness of the controller by contouring differently shaped profiles.

In Figure 6.5 the results of a single sample experiment are illustrated, with a focus on the force output generated on the surface (top plot in the figure) and the end-effector's position, velocity and current states (bottom plot in the figure). The end-effector's position profile is depicted by the red line in the bottom plot, and its y-axis lays on the right side. Following the position profile from the beginning of the experiment, the manipulator starts at position 0 and moves forwards until it reaches a plateau, then goes backwards at about $t = 3.3$ seconds.

The velocity profile (blue line, bottom plot) for which the y-axis lays on the left side, displays positive values when motion forward is generated, or negative values when the rack moves backwards. The zero in velocity always follows the position plateau: when the end-effector position is constant, its time derivative is zero. It can be noticed that during the position plateau, the force sensed on the Force/Torque sensor reaches 5 N (green line in the top plot).

The presence of the plateau suggests that the target surface is flat (highlighted yellow areas), hence no motion is generated in either directions. Positive velocity suggests that the target profile is concave (green areas), viceversa negative velocity results from a convex profile (red areas).

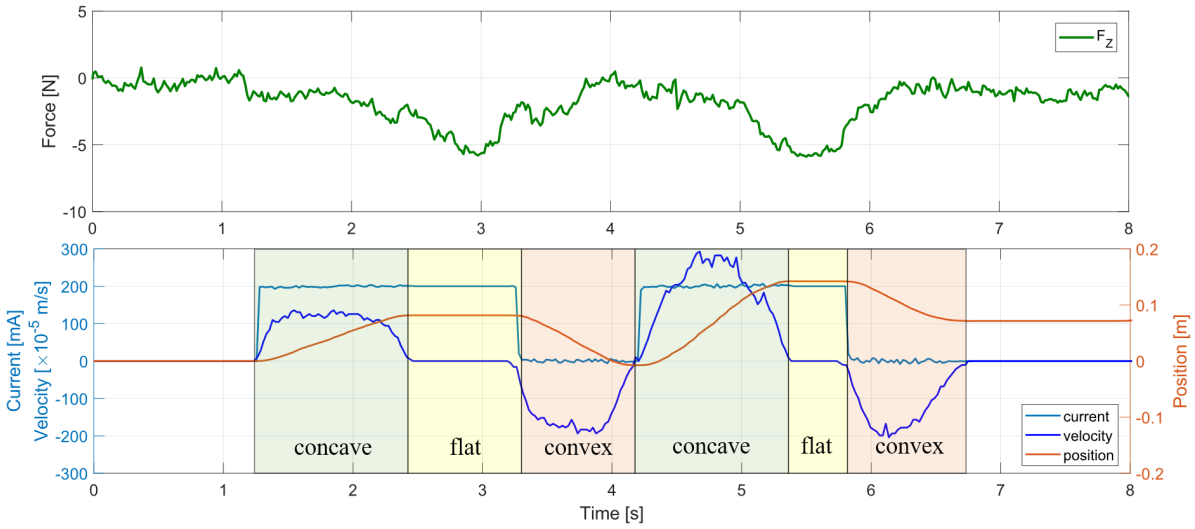

Figure 6.5: 3D contour following experiment highlighting the force curve (top) and the end-effector's position,velocity and current states (bottom).

The current profile is displayed as a light blue line in the bottom plot of the same figure, with its y-axis on the left side, along with the velocity axis. The current drives the rack at 200 mA and moves the end-effector towards the target. As the encoder senses an external force pushing the rack backwards, the *current* output is set as zero and the end-effector responds in a passive way. This occurs every time the manipulator is in contact with a convex profile, causing the end-effector to move backwards. As the targeted contour starts to flatten or becomes concave, the current input is set to positive again and the end-effector maintains contact with the surface.

Therefore, it can be inferred that the transition between concavity and convexity acts as a trigger on the manipulator as the external wrench is no longer zero: $\tau_{ext} > 0$. In the figure, the phases of the task are highlighted within green, yellow and orange boxes as the manipulator contours a concave, flat or convex profile.

Figure 6.6 illustrates another sample experiment. As seen above, the position, velocity and current curves are highlighted inside yellow, green and red boxes describing the flat, concave and convex profile respectively of the contoured structure. Additionally, this figure presents a purple area towards the end of the experiment that highlights the "contact loss" section of the experiment. It is to be noted that the position curve starts at an initial value of 0 and this is just to characterise the start of the experiment, associated with a zero value at the encoder.

The force curve in the top plot shows on average -2 N of force being exerted by the manipulator, with peaks up to -5 N. Towards the end of the experiment, at $t = 16.2s$

the manipulator experiences contact loss with the environment, as the target surface is deliberately removed. As a consequence, the force output on the sensor goes to 0 N, while the manipulator's velocity spikes towards higher values, triggering the *no contact* condition. The energy value inside the virtual tank reaches its upper threshold, as illustrated in the bottom figure (cyan curve). Hence, the tank is instantaneously drained and both current and velocity values quickly move to zero. The effectiveness of the contact loss condition can be seen in the position curve (red line, middle plot) by looking at the displacement of the end-effector since the moment of the contact loss detection: the rack only displaces by 11 mm from the moment the condition is met.

To conclude, the experiments showed a good accuracy in 3D contour following using the 1-DoF manipulator mounted on a stationary base. Continuous contact was kept despite the irregularly shaped profiles and robust control over the end-effector was achieved throughout multiple trials. The ability to cope with contact loss was also demonstrated, as this is a key feature for a manipulator that could operate on mobile robots such as UAVs.

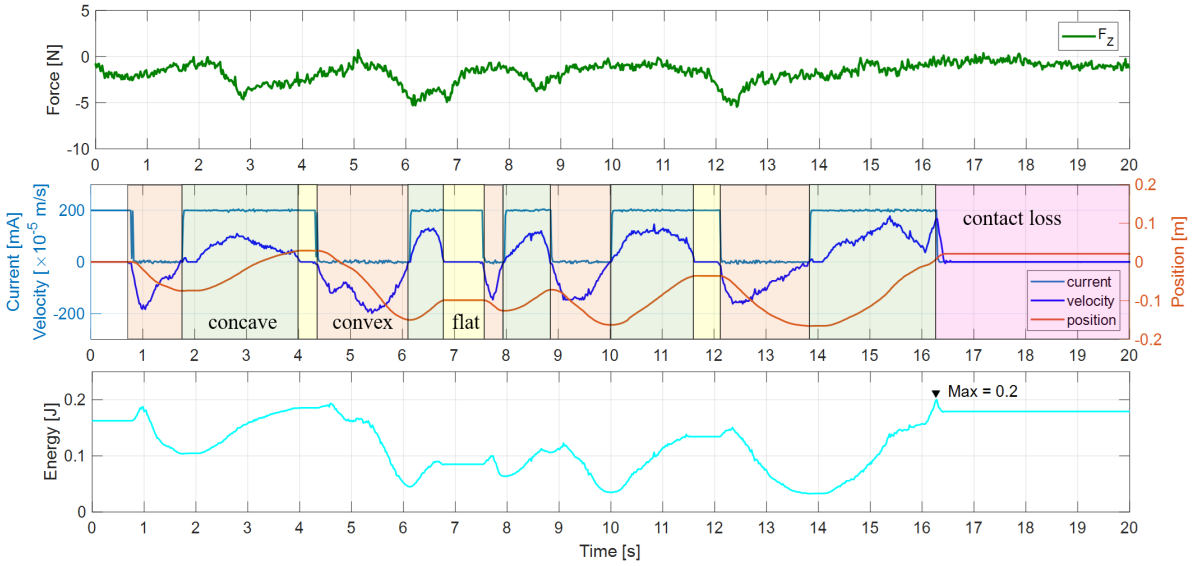

Figure 6.6: Experiment demonstrating 3D contour following for longer periods. From top to bottom: force curve; position,velocity and current curves; and the tank energy curve.

6.5 Flight Experiments

In this section, the flight experiments of the proposed system are presented and discussed. The objective is to demonstrate the ability of the aerial manipulator to apply a continuous shear force over a surface and minimise contact loss with the target.

One of the key challenges faced in the flight tests is the ability to keep stable and un-interrupted contact with the target throughout the entire length of the surface. The main factors that can affect the performance of the operation are the perturbations induced by the turbulence in the proximity of the wall, and those induced by the contact with the target on the vehicle. In fact, despite the minimal friction obtained with a metal ball caster end-effector, some friction still occurs, resulting in a lateral force at the tip of the end-effector. Such force is opposed to the direction of movement and it causes a drag/resistance on the aircraft.

The flight controller normal response to any resistance sensed on the vehicle is to adjust the thrust and angular states in an attempt to gain stability. This behaviour may result in drifting and loss of altitude, as well as in the end-effector's detachment from the contact surface. Therefore, the main challenge faced by the aerial manipulator is the ability to overcome any drifting in the vehicle whilst preserving the contact, and correct the end-effector's position and force output accordingly in real time.

6.5.1 Experimental Setup

The setup used for flight experiments is the same as the one seen in the previous chapter, section 5.1.3. The aerial platform is the quadcopter Lumenier QAV400® (1.1kg) with flight controller Pixhawk 4®. The manipulator on-board computer is a Raspberry PI 3 with Wi-Fi capabilities. The slider joint is actuated by a brushless DC motor, with

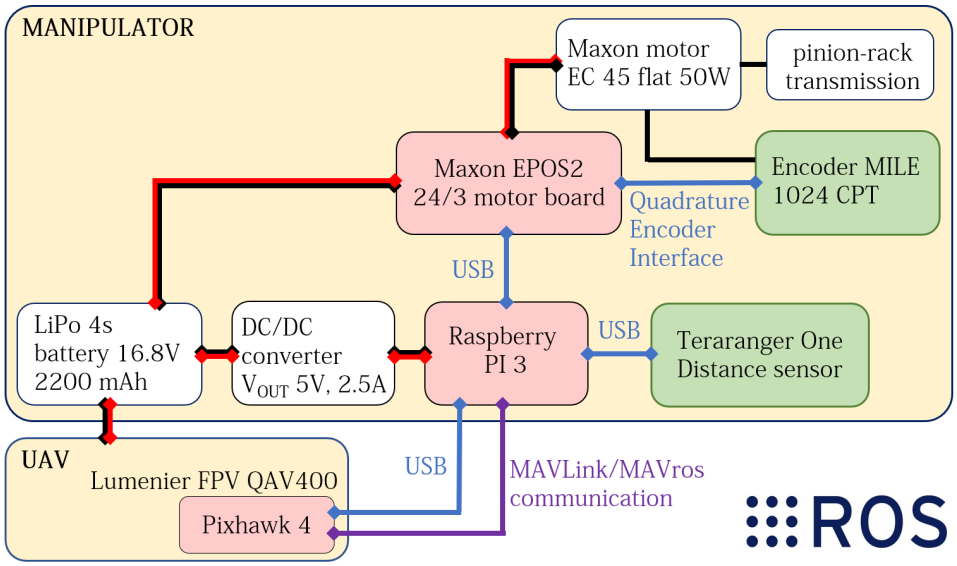

Figure 6.7: Experimental setup of the aerial manipulator during flight experiments, as presented in the previous chapter.

Hall sensor and digital encoder. The motor controller board is the high-performance Maxon® EPOS2 24/3 digital board, sampling at a rate of 10 kHz. The distance sensor is the TeraRanger® One, mounted at the front of the aircraft measuring the UAV's relative position with respect to the obstacle in front. The manipulator total mass is 500 g, and the aircraft all-up weight is 1.85 kg. The software implementation is in ROS. Ground-truth measurements of the UAV states in-flight are acquired by a VICON motion capture system. Figure 6.7 illustrates the experimental setup.

6.5.2 Results

The outline of the experiments is as follow: the UAV flies in *position* mode towards the target surface at a constant speed of 0.5 m/s, following a waypoint mission. The vehicle's angular states and relative position are tracked by the task manager on the manipulator (Raspberry PI 3) thorough a MAVLink/MAVros bridge. Once the conditions on *stability* and *proximity with the target* are met, the manipulation task is autonomously triggered. The UAV states are continuously fed back to the manipulator's force controller, along with the distance information from the rangefinder. After the end-effector is extended and contact is established with the surface, the UAV flies sideways while facing the target ahead, and the manipulator exerts a continuous force over the surface. When the obstacle becomes out of range, the manipulation task terminates and the end-effector retracts to its home position.

Figure 6.8 shows the UAV *x-y-z* coordinates during the task compared to the setpoint. It can be noticed how the vehicle's position error from the target position is kept low throughout the experiment, as illustrated by Figure 6.9. The *x-y* values reach 15 cm as the vehicle moves in between waypoints, outside the contact area. However, both values remain below 5 cm during the interaction task. This was also facilitated by a lower speed of approach within the area of interaction with the vertical wall. Outside the wall boundaries, the UAV velocity was set as $v = 0.5\ m/s$ as opposed to $v = 0.1\ m/s$ during contact.

Looking at the error in x during contact we can notice how it increases in a linear trend. This error is induced by the manipulator extending further in the x-direction, pushing the vehicle's centre-of-gravity backwards with respect to the wall. The error along z is fairly low throughout the entire experiment, i.e. on average less than 2 cm. Figure 6.10 shows the vehicle angular rates. It can be seen that both the *pitch* and *yaw* rate have peak oscillations as the the end-effector makes contact with the wall. From t = 12.5 s until the end of the task the angular rates remain below 0.2, showing that

disturbances sensed by the vehicle are low throughout the interaction, despite the fact that the manipulator is applying a force over 5 N on the target (see Figure 6.11, *bottom*). Overall Figure 6.11 displays the end-effector position and velocity states, along with the force generated at the end-effector.

Figure 6.12 displays a side view of the aerial manipulator during experiments. The ball caster tip has been replaced by a marker pen to give the reader a better visualisation

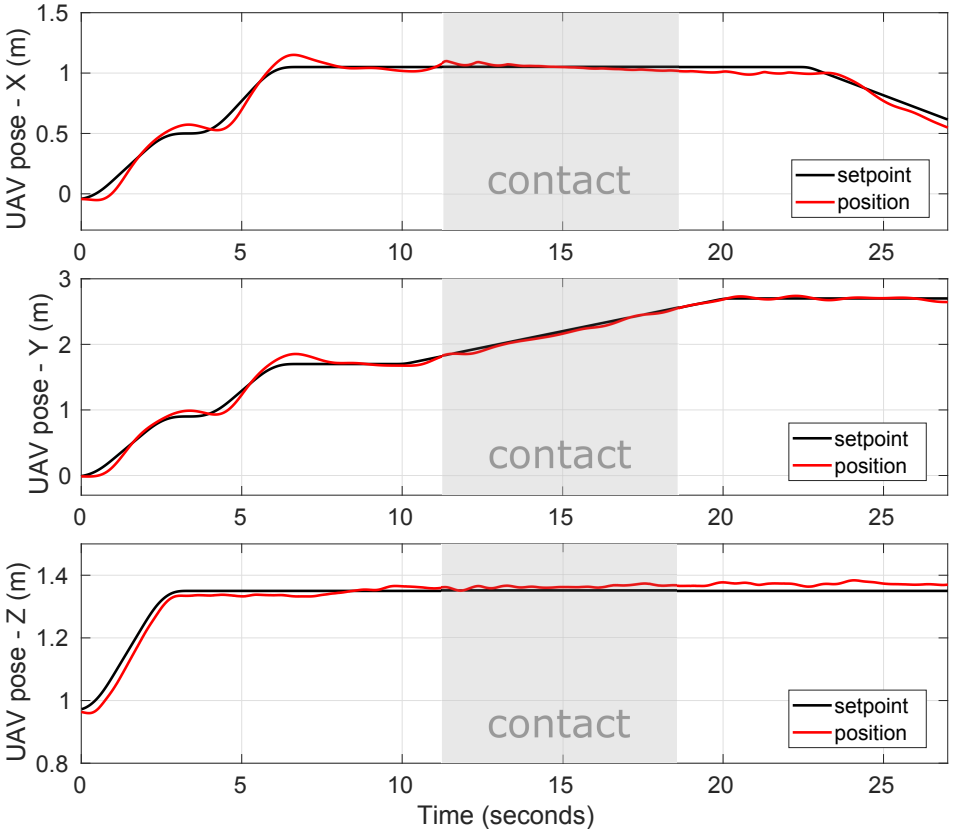

Figure 6.8: UAV position along the *x*-*y*-*z* axes during 2D aerial contour following.

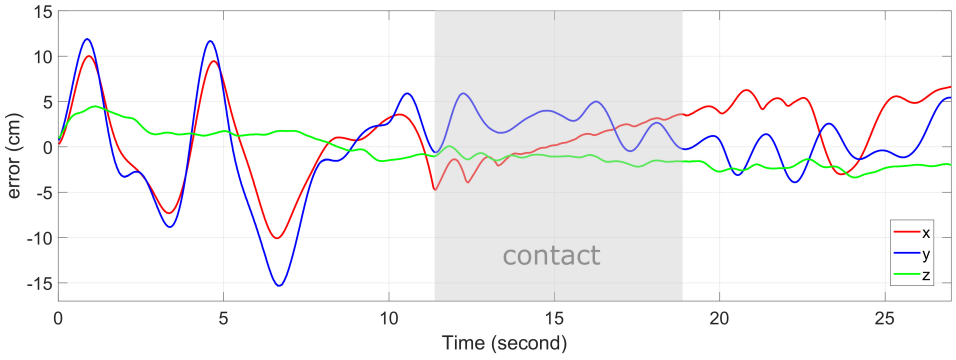

Figure 6.9: UAV positioning error along the *x*-*y*-*z* axes during 2D aerial contour following.

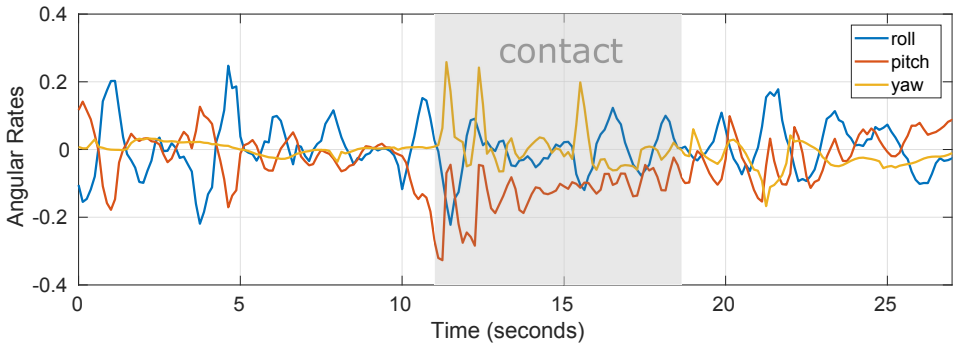

Figure 6.10: UAV angular rates during 2D aerial contour following.

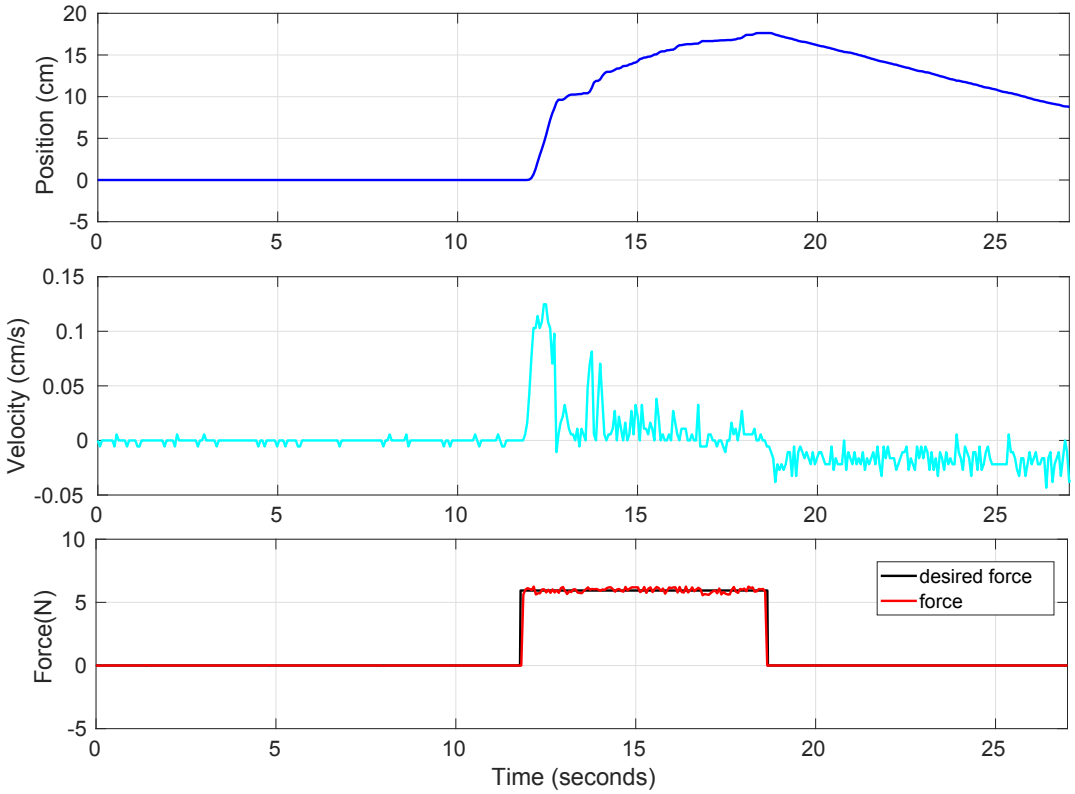

Figure 6.11: From top to bottom: manipulator position and velocity states and force exerted at the end-effector.

on the performance accuracy, as the manipulator draws a line on the target surface. The line is drawn on the whole length of the panel (approximately 1.25 m) and without interruptions.

Looking at figures 6.12 and Figure 6.9 we can appreciate that the error on the z axis (the axis pointing to the ceiling) remains below 1 cm during the interaction task, resulting in a straight line on the target surface. A small drop in height is visible in

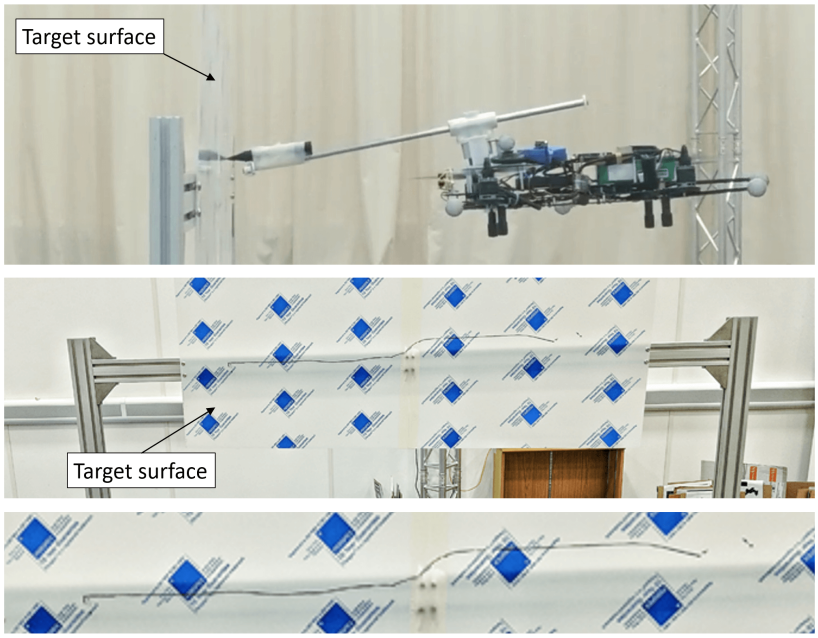

Figure 6.12: Continuous contact between the aerial manipulator and the target surface is demonstrated with the use of a pen marker, which allows the aerial system to draw a continuous line over a length of 1.25 metres.

the middle section of the target surface due to the presence of fixtures on the mounting structure (see Figure 6.12).

Overall, a total number of 15 experiments has been conducted. A successful outcome was assigned to those experiments where the end-effector kept in continuous contact throughout the entire length. Overall, a success rate of 86% was reached.

6.6 Conclusions

Energy tank-based methods can bring significant benefit to aerial manipulators, providing a reliable and robust approach towards interaction control. Within this chapter, the first example of energy tank-based force control for aerial manipulators has been presented, aimed at contour following applications with unknown surfaces. The addition of the virtual tank to the force-tracking capabilities of the manipulator allows to implement a more constrained controller which can be best suited when interacting with un-modelled environments where the contact-loss condition is likely to appear.

The control approach is validated on a single-DoF manipulator in two different setups: on a stationary base and on the aerial platform. Consistent touch and accuracy

are achieved throughout the experiments in both setups, as well as robustness with differently shaped profiles. The ability to successfully apply a continuous shear force over 2D and 3D surfaces for prolonged periods of time is demonstrated, along with the benefits brought by the virtual tank in scenarios where contact loss occurs.

From the experiments conducted, the following *lessons learnt* are derived:

- the virtual tank approach brings a benefit to the overall system's compliance in both cases of interaction on a stationary and floating base thanks to the addition of velocity and accelerations constraints in the control laws. This greatly improves the efficiency of the manipulator, as well as the safety conditions at which the interaction is carried out;

- the proposed end-effector design is well suited when deployed over 3D surfaces on a stationary base, however some limitations are posed by this design during aerial experiments. In particular, it was noted that when irregularities on the target surface were present, lateral forces propagated from the end-effector to the floating base, inducing a momentum to the aircraft. In most cases, such momentum was counteracted by the vehicle while maintaining contact with the target, however this outcome was not consistent throughout all experiments (2 out of 15 aerial experiments displayed contact loss with the target);

- the integration of the vehicle states within the manipulator's controller aids the interaction and offers a way to automate the task. Closed-loop control on the manipulator itself is certainly beneficial to the performance of the aerial manipulator as a whole, however further improvements can be brought when considering the aerial vehicle and the manipulator as a single multi-variable system, that can compensate for each sub-system's limitations;

- success rates of 100% in the stationary case and over 85% in the aerial experiments are achieved, showing the potential of the control approach along with the manipulator's design for tracing out more complex 3D surfaces in the future, and aid other tactile-driven aerial applications.

CHAPTER 7

CONCLUSIONS

In this chapter, the conclusions drawn from the work presented in this thesis are discussed. Recalling the aim of this research stated in the introductory chapter, the goal is to demonstrate that aerial manipulators can be deployed for dynamic physical interaction with the environment and accomplish force-driven tasks that require limited dexterity. The methodology used towards this goal stresses the importance of combining the control strategies with a smart body design. Four main objectives are derived to address the research aim, which unfold in using a simple yet efficient manipulator's design that features compliance to guarantee safe and robust interaction airborne.

The first objective of this research is to analyse aerial interaction and evaluate the vector dynamics to understand which are the variables involved during side-interaction with a surface and how they contribute towards the aerial system's stability and dynamic response. The interaction is evaluated from a theoretical point of view and in simulation studies. One of the key assumptions used for the modelling lies in the planar representation of aerial side-interaction: the force exchange is portrayed only in one plane (the pitch plane), and laterally induced disturbances and slippage at the end-effector are assumed to be negligible. This underlying assumption was incorporated in the manipulator's design and control strategies which excluded the possibility of lateral inputs at the end-effector.

Despite the planar representation portrays a simplified version of the reality, the experiments conducted throughout this thesis have shown how this assumption has held in real experiments, with repeatable and robust outcome. In fact, it was demonstrated

that the disturbances induced by the interaction had negligible effect on the roll and yaw angles, whereas oscillatory response was consistently found on the pitch angle, i.e. the angular state lying on the interaction plane. Therefore it was demonstrated that the planar assumption was applicable to a large extent, with the exception of a few cases in which the vehicle was subjected to laterally induced disturbances. This is an important conclusion as it shows that the challenges of aerial interaction can be simplified from both a design and control perspective to the 3D case, as opposed to the 6D case.

The second objective of this thesis is to tackle aerial interaction from the design perspective and tailor the manipulation system to facilitate force exchange and to benefit the dynamic response. This objective unfolds in several design requirements. To begin with, the available payload poses limitations on the number of the components being used, as well as the total number of degrees of freedom. The choice of a compact, minimal design is consciously made to serve force-based task specifications with limited dexterity involved. Such use of the available payload for a low-DoF manipulator allows to dedicate more attention in the selection of the right components to convey real-time force control and close-loop feedback on the force delivered.

Compliance is also introduced as part of the design, in line with several works found in the literature that exploit such feature. Compliance in the proposed manipulator is achieved through the controller, which mimics a torsional spring behaviour at the prismatic joint via a rack-and-pinion mechanism. This represents a compact and lightweight solution to deliver high forces at the end-effector in real-time and in a compliant way. It is demonstrated within the experiments in chapters 4 to 6 that compliance is crucial for aerial dynamic interaction as it aids the aerial vehicle's stability, it partially absorbs the energy of collisions, it dampens the propagation of the disturbances to the vehicle's CoG and therefore it brings a benefit to performance, safety and indirectly to extended battery life.

Overall the proposed design is lightweight, compact and compliant and demonstrates great adaptability for force-based aerial applications that require limited dexterity. A number of operations were successfully performed using the bespoke manipulator, such as tapping on a surface, installing and retrieving a sensor on a vertical or cylindrical surface, and contour following a 2D wall. The novel approach to aerial manipulation tasks and the introduction of such compact, minimal design validates several advantages associated to low-DoF manipulators and the importance of refinement not only at a control level, but also at a hardware level. Despite the limited dexterity, the bespoke

design shows great versatility, modularity and high accuracy in the accomplishment of challenging tasks.

The third objective relates to the manufacturing of the proposed manipulator and addresses the systems' integration of the aerial vehicle with sensing and electronics on-board, together with initial experiments in force generation. Within the integration of the manipulator on the UAV, further considerations are presented on the configuration, the distribution of masses, the symmetry in the components within the layout, the selection of high performance and low latency electronics. Together with the high-level decisions made in the design process (see previous objective), this new set of low-level decisions channel into the creation of the *final* product, the UAM, and contribute to further favour the vehicle's stability and dynamic response. This objective stresses the importance of addressing the hardware-related constraints at all levels, in order to improve the performance of the system, extend the robustness and ultimately increase the reliability.

The initial set of experiments proves that introducing variable compliance as part of the manipulation system aids the vehicle stability and allows to adjust the force output according to the task specifications. Varying the compliance of the manipulator also has a positive effect on the vehicle dynamic response and recovery period following interaction. Tapping operations using the 2-DoF manipulator are also validated in multiple flight experiments showing that the compliant UAM is able to partially absorb the propagation of kinetic energy induced during tapping motion, and produce repeated cycles of rapid force exchange.

The fourth objective focuses on the refinement of the aerial manipulator as a whole. The broader spectrum of this objective allows to investigate novel approaches in aerial force-exchange in order to shape the force curve delivered, extend the time in contact, and tailor the proposed design to a wider range of applications. Hence, the refinement is brought together at both design and control levels.

In terms of the design, the lessons learnt from the initial experiments are funnelled into the refinement process to bring additional improvements to the mechanics, sensing and electronics of the manipulator. The use of a high performance motor controller on the prismatic joint, and a faster on-board computer make real-time control possible. A new method of force exertion was introduced to deliver a slow force build-up at the end-effector, with the UAV pitch motion included “in the loop". The force output results from the combined action of the manipulator and the vehicle's thrust transferred during

pitching. This approach was tested in different scenarios, both indoors and outdoors with robust and repeatable results in the installation and retrieval of sensors in the environment. The set of experiments demonstrated the ability to shape the force profile, adjust the time in contact and build a slow force build-up thanks to the contribution of both the manipulator and the aircraft. The combined force action was demonstrated for the first time in the state of the art within these experiments, and it proved exceedingly robust and accurate, even in the outdoor setting.

In the last chapter, the refinement of the UAM was tackled from a control perspective to accomplish the exertion of a continuous shear force for contour follow applications. An energy tank-based method was implemented in addition to the force-tracking controller to deliver the force in a safer, energy-efficient way. The flight experiments successfully demonstrated the use of such energy-tank controller for the prolonged application of force over time; along with the ability to generate compliant touch at the end-effector and compensate for the vehicle's drifting and altitude loss while maintaining contact with the target. The goal of the experiments was not only to show the effectiveness of the energy-based approach paired with the bespoke manipulator, but also to explore novel applications in aerial robotics where the manipulation tool can serve multiple purposes, such as behaving as a sensing device that can aid the navigation and provide active tactile feedback to the aerial platform.

Overall, the proposed design has demonstrated to be well suited for force-based tasks that require limited dexterity. Some of the aerial applications envisioned for such compliant aerial manipulator may include:

- marking of cracks on wind turbine blades, bridges and other large-scale structures (through contour following operations);

- declogging of thermocouples obstructed by dust and fumes particles on the walls of high industrial chimneys (through tapping operations);

- aiding UAVs indoor navigation in search and rescue scenarios in which visual sensing alone is insufficient; tactile feedback can assist safe navigation within enclosed areas;

- installation and retrieval of smart sensors for monitoring the structural integrity of bridges and dams;

- installation of smoke detectors and humidity sensors in forestry environment for fire prevention and climate monitoring;
- other more generic contact-based inspection operations and NDT.

It can be concluded that force exchange conducted on an aerial robot has the advantage of tackling a wider range of applications and therefore improves the versatility of aerial manipulators. The two major implications of UAMs capable of interacting in the environment and conduct challenging contact-based tasks are the improvement of safety standards, and the lowered risks and associated costs involved when replacing human operators that work in hard-to-reach locations and hazardous conditions. Throughout this thesis it was demonstrated that a tailored design together with compliant control designate a robust and reliable approach towards new, challenging force-based aerial applications.

7.1 Future Work

In this section some of the ideas to further expand on the work of this thesis are presented. The following concepts may have sprouted from ideas developed on the side, curiosities, or they may have resulted by acknowledging some of the limitations in the current approach that could be the case of further studies. To begin with, some ideas on the expansion of the design are presented.

The proposed manipulation system was developed as a compact, lightweight design to address force-driven tasks. The limited dexterity of the design however makes object-handling hard to achieve in the present state. One idea to increase the dexterity would be to add a wrist-like mobility at the end-effector by the introduction, for example, of a ball and socket joint. An underactuated spherical joint could be developed where the only controlled rotation is about the longitudinal axis, to accomplish twisting motion at the wrist. This could be useful in operations where the installation of the object over a wall may have requirements in the orientation, or for a peg-in-hole task with non-circular objects. If however the vehicle's payload allows for it, all 3 DoFs of the spherical joint could be actuated to accomplish controlled motion about the 3 axes.

Another useful feature would be to incorporate an additional degree of freedom at the base of the manipulator to compensate for disturbances caused in the *yaw* plane. Lateral forces acting at the end-effector propagate to vehicle's CoG through the rack, inducing a momentum on the vehicle about its yaw axis. By including an independent, responsive

actuator that is able to counteract such induced disturbances, both the performance and stability in-flight would be benefited. Similarly to what was done with the introduction of the servo motor in chapter 3 and 4 to decouple the pitch motion of the manipulator from the one of the aircraft, the idea here is to replicate this concept in the yaw plane and introduce an active DoF that could compensate for slippage and lateral forces, avoiding their propagation to the aircraft CoG.

This brings to another point, i.e. the adaptability of such manipulator for a wider range of applications. Recalling the work done in chapter 6 where the UAM is deployed to contour follow a 2D surface, it is expected that 3D aerial contour following would be challenging to achieve with the current design. Throughout the experiments, it was noticed that the lateral forces generated by the shear contact at the EE were negligible, or small enough, to be solely counteracted by the flight controller. The friction-less ball caster at the tip of the rack facilitated smooth shear contact with the target, however it is expected that 3D profiles with prominent curvatures would induce higher forces and momentum on the aircraft. In this respect, the presence of an active DoF in the yaw plane could aid stability and improve the performance, regardless of the target's geometry.

Moving to the sensing, it was found that the high-performance rangefinder seen in chapter 5 and 6 was useful to create a level of autonomy in the operation: the triggering and the retraction of the end-effector were automated based on the proximity information of the sensor included in the control loop. However, the sensor per se was of limited use during the completion of the task itself. Additional sensors such as event-based cameras that implement object and motion tracking could help in this respect, and make the manipulation task fully autonomous. Such visual feedback could also be incorporated in the feedback loop to make supervisory-level decisions during the operation, and to consolidate the safety standards.

Lastly, some ideas for further work in the control domain are presented. Within this thesis, a decentralised approach was taken in the control of the aerial manipulator, and this is in line with the most works found in the literature [4, 33, 40, 42, 46, 54, 71, 90, 92, 93]. However, it would be interesting to see the extent to which the performance could be improved with the introduction of a centralised controller. Such controller would supervise the integration of each sub-system's behaviour and sensorial feedback to enhance accuracy, mobility, robustness and reliability of the aerial manipulator as a whole. The centralised controller could be implemented as an additional layer on top of the flight controller and would take into account the aerial system's states, as well as the

manipulator's states to make high-level decisions during dynamic interaction.

Within this scenario, the propagation of disturbances from the end-effector to the floating base could be compensated by the vehicle itself, even in a predictive way with the use of, for example, Model Predictive Control (MPC). Other approaches in the domain of optimal control could also aid in this respect, possibly stretching to machine learning methods. In essence, the presence of a high-level optimal controller would induce better-performing behaviours in terms of energy, efficiency and power consumption, exploiting the rotors' thrust with the manipulator's force and ultimately creating a single multi-variable system.

BIBLIOGRAPHY

[1] A. Albers, S. Trautmann, T. Howard, T. A. Nguyen, M. Frietsch, and C. Sauter, "Semi-autonomous flying robot for physical interaction with environment," in *Robotics Automation and Mechatronics (RAM), 2010 IEEE Conference on*, pp. 441–446, IEEE, 2010.

[2] L. Marconi, F. Basile, G. Caprari, R. Carloni, P. Chiacchio, C. Hurzeler, V. Lippiello, R. Naldi, J. Nikolic, B. Siciliano, *et al.*, "Aerial service robotics: The airobots perspective," in *2012 2nd International Conference on Applied Robotics for the Power Industry (CARPI)*, pp. 64–69, IEEE, 2012.

[3] A. Q. Keemink, M. Fumagalli, S. Stramigioli, and R. Carloni, "Mechanical design of a manipulation system for unmanned aerial vehicles," in *Robotics and Automation (ICRA), 2012 IEEE International Conference on*, pp. 3147–3152, IEEE, 2012.

[4] E. Cataldi, G. Muscio, M. A. Trujillo, Y. Rodríguez, F. Pierri, G. Antonelli, F. Caccavale, A. Viguria, S. Chiaverini, and A. Ollero, "Impedance control of an aerial-manipulator: Preliminary results," in *Intelligent Robots and Systems (IROS), 2016 IEEE/RSJ International Conference on*, pp. 3848–3853, IEEE, 2016.

[5] T. Bartelds, A. Capra, S. Hamaza, S. Stramigioli, and M. Fumagalli, "Compliant aerial manipulators: Toward a new generation of aerial robotic workers," *IEEE Robotics and Automation Letters*, vol. 1, no. 1, pp. 477–483, 2016.

[6] A. Suarez, G. Heredia, and A. Ollero, "Compliant and lightweight anthropomorphic finger module for aerial manipulation and grasping," in *Robot 2015: Second Iberian Robotics Conference*, pp. 543–555, Springer, 2016.

[7] "AIRobots, A New Generation Of Aerial Service Robots." `http://airobots.ing.unibo.it/`.
2012.

[8] "ARCAS project: Manipulation and assembly in the air: the new powerful drones." http://www.arcas-project.eu/.
2015.

[9] "AEROARMS, Aerial Robotics Systems with Advanced Manipulation Capabilities for Inspection and Maintenance." http://aeroarms-project.eu/.
2015.

[10] "AErial RObotic System for In-Depth Bridge Inspection by Contact." http://www.aerobi.eu/.
2015.

[11] "AEROWORKS, Collaborative Aerial Workers." http://www.aeroworks2020.eu/.
2015.

[12] M. Bernard and K. Kondak, "Generic slung load transportation system using small size helicopters," in *Robotics and Automation, 2009. ICRA'09. IEEE International Conference on*, pp. 3258–3264, IEEE, 2009.

[13] P. E. Pounds, D. R. Bersak, and A. M. Dollar, "The yale aerial manipulator: grasping in flight," in *Robotics and Automation (ICRA), 2011 IEEE International Conference on*, pp. 2974–2975, IEEE, 2011.

[14] P. E. Pounds and A. M. Dollar, "Stability of helicopters in compliant contact under pd-pid control.," *IEEE Transactions on Robotics*, vol. 30, no. 6, pp. 1472–1486, 2014.

[15] N. Michael, J. Fink, and V. Kumar, "Cooperative manipulation and transportation with aerial robots," *Autonomous Robots*, vol. 30, no. 1, pp. 73–86, 2011.

[16] D. Mellinger, M. Shomin, N. Michael, and V. Kumar, "Cooperative grasping and transport using multiple quadrotors," in *Distributed autonomous robotic systems*, pp. 545–558, Springer, 2013.

[17] M. Mohammadi, A. Franchi, D. Barcelli, and D. Prattichizzo, "Cooperative aerial tele-manipulation with haptic feedback," in *2016 IEEE/RSJ International Conference on Intelligent Robots and Systems (IROS 2016)*, 2016.

[18] G. Gioioso, A. Franchi, G. Salvietti, S. Scheggi, and D. Prattichizzo, "The flying hand: A formation of uavs for cooperative aerial tele-manipulation," in *Robotics*

and Automation (ICRA), 2014 IEEE International Conference on, pp. 4335–4341, IEEE, 2014.

[19] Q. Lindsey, D. Mellinger, and V. Kumar, "Construction of cubic structures with quadrotor teams," *Proc. Robotics: Science & Systems VII*, 2011.

[20] F. Augugliaro, S. Lupashin, M. Hamer, C. Male, M. Hehn, M. W. Mueller, J. S. Willmann, F. Gramazio, M. Kohler, and R. D'Andrea, "The flight assembled architecture installation: Cooperative construction with flying machines," *IEEE Control Systems*, vol. 34, no. 4, pp. 46–64, 2014.

[21] F. Augugliaro, A. Mirjan, F. Gramazio, M. Kohler, and R. D'Andrea, "Building tensile structures with flying machines," in *2013 IEEE/RSJ International Conference on Intelligent Robots and Systems*, pp. 3487–3492, IEEE, 2013.

[22] P. E. Pounds and A. Dollar, "Hovering stability of helicopters with elastic constraints," in *ASME 2010 Dynamic Systems and Control Conference*, pp. 781–788, American Society of Mechanical Engineers, 2010.

[23] P. E. Pounds and A. M. Dollar, "Uav rotorcraft in compliant contact: Stability analysis and simulation," in *Intelligent Robots and Systems (IROS), 2011 IEEE/RSJ International Conference on*, pp. 2660–2667, IEEE, 2011.

[24] D. Mellinger, Q. Lindsey, M. Shomin, and V. Kumar, "Design, modeling, estimation and control for aerial grasping and manipulation," in *Intelligent Robots and Systems (IROS), 2011 IEEE/RSJ International Conference on*, pp. 2668–2673, IEEE, 2011.

[25] C. M. Korpela, T. W. Danko, and P. Y. Oh, "Mm-uav: Mobile manipulating unmanned aerial vehicle," *Journal of Intelligent & Robotic Systems*, vol. 65, no. 1-4, pp. 93–101, 2012.

[26] T. W. Danko, K. P. Chaney, and P. Y. Oh, "A parallel manipulator for mobile manipulating uavs," in *Technologies for Practical Robot Applications (TePRA), 2015 IEEE International Conference on*, pp. 1–6, IEEE, 2015.

[27] C. D. Bellicoso, L. R. Buonocore, V. Lippiello, and B. Siciliano, "Design, modeling and control of a 5-dof light-weight robot arm for aerial manipulation," in *2015 23rd Mediterranean Conference on Control and Automation (MED)*, pp. 853–858, IEEE, 2015.

[28] V. Lippiello and F. Ruggiero, "Cartesian impedance control of a uav with a robotic arm," *IFAC Proceedings Volumes*, vol. 45, no. 22, pp. 704–709, 2012.

[29] V. Lippiello and F. Ruggiero, "Exploiting redundancy in cartesian impedance control of uavs equipped with a robotic arm," in *2012 IEEE/RSJ International Conference on Intelligent Robots and Systems*, pp. 3768–3773, IEEE, 2012.

[30] M. Fumagalli, R. Naldi, A. Macchelli, R. Carloni, S. Stramigioli, and L. Marconi, "Modeling and control of a flying robot for contact inspection," in *Intelligent Robots and Systems (IROS), 2012 IEEE/RSJ International Conference on*, pp. 3532–3537, IEEE, 2012.

[31] J. L. Scholten, M. Fumagalli, S. Stramigioli, and R. Carloni, "Interaction control of an uav endowed with a manipulator," in *Robotics and Automation (ICRA), 2013 IEEE International Conference on*, pp. 4910–4915, IEEE, 2013.

[32] S. Kim, S. Choi, and H. J. Kim, "Aerial manipulation using a quadrotor with a two dof robotic arm," in *Intelligent Robots and Systems (IROS), 2013 IEEE/RSJ International Conference on*, pp. 4990–4995, IEEE, 2013.

[33] A. Jimenez-Cano, J. Martin, G. Heredia, A. Ollero, and R. Cano, "Control of an aerial robot with multi-link arm for assembly tasks," in *Robotics and Automation (ICRA), 2013 IEEE International Conference on*, pp. 4916–4921, IEEE, 2013.

[34] F. Huber, K. Kondak, K. Krieger, D. Sommer, M. Schwarzbach, M. Laiacker, I. Kossyk, S. Parusel, S. Haddadin, and A. Albu-Schaffer, "First analysis and experiments in aerial manipulation using fully actuated redundant robot arm," in *Intelligent Robots and Systems (IROS), 2013 IEEE/RSJ International Conference on*, pp. 3452–3457, IEEE, 2013.

[35] G. Giglio and F. Pierri, "Selective compliance control for an unmanned aerial vehicle with a robotic arm," in *Control and Automation (MED), 2014 22nd Mediterranean Conference of*, pp. 1190–1195, IEEE, 2014.

[36] M. Orsag, C. Korpela, S. Bogdan, and P. Oh, "Valve turning using a dual-arm aerial manipulator," in *Unmanned Aircraft Systems (ICUAS), 2014 International Conference on*, pp. 836–841, IEEE, 2014.

[37] M. Fumagalli, R. Naldi, A. Macchelli, F. Forte, A. Q. Keemink, S. Stramigioli, R. Carloni, and L. Marconi, "Developing an aerial manipulator prototype: Physical

interaction with the environment," *Robotics & Automation Magazine, IEEE*, vol. 21, pp. 41–50, 2014.

[38] A. Y. Mersha, S. Stramigioli, and R. Carloni, "Variable impedance control for aerial interaction," in *Intelligent Robots and Systems (IROS 2014), 2014 IEEE/RSJ International Conference on*, pp. 3435–3440, IEEE, 2014.

[39] F. Ruggiero, M. A. Trujillo, R. Cano, H. Ascorbe, A. Viguria, C. Peréz, V. Lippiello, A. Ollero, and B. Siciliano, "A multilayer control for multirotor uavs equipped with a servo robot arm," in *2015 IEEE international conference on robotics and automation (ICRA)*, pp. 4014–4020, IEEE, 2015.

[40] A. Suarez, G. Heredia, and A. Ollero, "Lightweight compliant arm for aerial manipulation," in *Intelligent Robots and Systems (IROS), 2015 IEEE/RSJ International Conference on*, pp. 1627–1632, IEEE, 2015.

[41] J. Bartelds, H. Wopereis, S. Stramigioli, and M. Fumagalli, "A comparison of control approaches for aerial manipulators handling physical impacts," in *Control and Automation (MED), 2016 24th Mediterranean Conference on*, pp. 646–652, IEEE, 2016.

[42] A. Suarez, P. R. Soria, G. Heredia, B. C. Arrue, and A. Ollero, "Anthropomorphic, compliant and lightweight dual arm system for aerial manipulation," in *Intelligent Robots and Systems (IROS), 2017 IEEE/RSJ International Conference on*, pp. 992–997, IEEE, 2017.

[43] C. J. Salaan, K. Tadakuma, Y. Okada, E. Takane, K. Ohno, and S. Tadokoro, "Uav with two passive rotating hemispherical shells for physical interaction and power tethering in a complex environment," in *Robotics and Automation (ICRA), 2017 IEEE International Conference on*, pp. 3305–3312, IEEE, 2017.

[44] A. Briod, P. Kornatowski, J.-C. Zufferey, and D. Floreano, "A collision-resilient flying robot," *Journal of Field Robotics*, vol. 31, no. 4, pp. 496–509, 2014.

[45] A. Suarez, G. Heredia, and A. Ollero, "Physical-virtual impedance control in ultralightweight and compliant dual arm aerial manipulators," *IEEE Robotics and Automation Letters*, 2018.

[46] M. Ryll, G. Muscio, F. Pierri, E. Cataldi, G. Antonelli, F. Caccavale, and A. Franchi, "6d physical interaction with a fully actuated aerial robot," in *2017 IEEE International Conference on Robotics and Automation*, 2017.

[47] R. S. Ball, "The theory of screws: A study in the dynamics of a rigid body," *Mathematische Annalen*, vol. 9, no. 4, pp. 541–553, 1876.

[48] C. Papachristos, K. Alexis, and A. Tzes, "Efficient force exertion for aerial robotic manipulation: Exploiting the thrust-vectoring authority of a tri-tiltrotor uav," in *Robotics and Automation (ICRA), 2014 IEEE International Conference on*, pp. 4500–4505, IEEE, 2014.

[49] G. Jiang and R. Voyles, "Hexrotor uav platform enabling dexterous interaction with structures-flight test," in *2013 IEEE international symposium on safety, security, and rescue robotics (SSRR)*, pp. 1–6, IEEE, 2013.

[50] T. Ikeda, S. Yasui, M. Fujihara, K. Ohara, S. Ashizawa, A. Ichikawa, A. Okino, T. Oomichi, and T. Fukuda, "Wall contact by octo-rotor uav with one dof manipulator for bridge inspection," in *Intelligent Robots and Systems (IROS), 2017 IEEE/RSJ International Conference on*, pp. 5122–5127, IEEE, 2017.

[51] H. W. Wopereis, J. Hoekstra, T. Post, G. A. Folkertsma, S. Stramigioli, and M. Fumagalli, "Application of substantial and sustained force to vertical surfaces using a quadrotor," in *2017 IEEE International Conference on Robotics and Automation (ICRA)*, pp. 2704–2709, IEEE, 2017.

[52] D. R. McArthur, A. B. Chowdhury, and D. J. Cappelleri, "Autonomous control of the interacting-boomcopter uav for remote sensor mounting," in *2018 IEEE International Conference on Robotics and Automation (ICRA)*, pp. 1–6, IEEE, 2018.

[53] D. R. McArthur, A. B. Chowdhury, and D. J. Cappelleri, "Design of the interacting-boomcopter unmanned aerial vehicle for remote sensor mounting," *Journal of Mechanisms and Robotics*, vol. 10, no. 2, p. 025001, 2018.

[54] A. Suarez, G. Heredia, and A. Ollero, "Lightweight compliant arm with compliant finger for aerial manipulation and inspection," in *Intelligent Robots and Systems (IROS), 2016 IEEE/RSJ International Conference on*, pp. 4449–4454, IEEE, 2016.

[55] M. Fumagalli, S. Stramigioli, and R. Carloni, "Mechatronic design of a robotic manipulator for unmanned aerial vehicles," in *Intelligent Robots and Systems (IROS), 2016 IEEE/RSJ International Conference on*, pp. 4843–4848, IEEE, 2016.

[56] S. Hamaza, I. Georgilas, and T. Richardson, "An adaptive-compliance manipulator for contact-based aerial applications," in *2018 IEEE/ASME International Conference on Advanced Intelligent Mechatronics (AIM)*, pp. 730–735, IEEE, 2018.

[57] C. M. Korpela, T. W. Danko, and P. Y. Oh, "Designing a system for mobile manipulation from an unmanned aerial vehicle," in *Technologies for Practical Robot Applications (TePRA), 2011 IEEE Conference on*, pp. 109–114, IEEE, 2011.

[58] K. Kondak, F. Huber, M. Schwarzbach, M. Laiacker, D. Sommer, M. Bejar, and A. Ollero, "Aerial manipulation robot composed of an autonomous helicopter and a 7 degrees of freedom industrial manipulator," in *2014 IEEE International Conference on Robotics and Automation (ICRA)*, pp. 2107–2112, IEEE, 2014.

[59] C. Korpela, P. Brahmbhatt, M. Orsag, and P. Oh, "Towards the realization of mobile manipulating unmanned aerial vehicles (mm-uav): Peg-in-hole insertion tasks," in *Technologies for Practical Robot Applications (TePRA), 2013 IEEE International Conference on*, pp. 1–6, IEEE, 2013.

[60] I. Palunko, P. Cruz, and R. Fierro, "Agile load transportation: Safe and efficient load manipulation with aerial robots," *IEEE Robotics & Automation Magazine*, vol. 19, no. 3, pp. 69–79, 2012.

[61] P. E. Pounds, D. R. Bersak, and A. M. Dollar, "Grasping from the air: Hovering capture and load stability," in *Robotics and Automation (ICRA), 2011 IEEE International Conference on*, pp. 2491–2498, IEEE, 2011.

[62] M. Orsag, C. Korpela, and P. Oh, "Modeling and control of mm-uav: Mobile manipulating unmanned aerial vehicle," *Journal of Intelligent & Robotic Systems*, vol. 69, no. 1-4, pp. 227–240, 2013.

[63] S. P. Timoshenko and J. M. Gere, *Theory of Elastic Stability*. Courier Corporation, 2009.

[64] S. Hamaza, I. Georgilas, and T. Richardson, "Towards an adaptive-compliance aerial manipulator for contact-based interaction," in *2018 IEEE/RSJ International Conference on Intelligent Robots and Systems (IROS)*, pp. 1–9, IEEE, 2018.

[65] M. Bisgaard, A. la Cour-Harbo, and J. D. Bendtsen, "Adaptive control system for autonomous helicopter slung load operations," *Control Engineering Practice*, vol. 18, no. 7, pp. 800–811, 2010.

[66] F. Forte, R. Naldi, A. Macchelli, and L. Marconi, "Impedance control of an aerial manipulator," in *American Control Conference (ACC), 2012*, pp. 3839–3844, IEEE, 2012.

[67] J. G. Ziegler and N. B. Nichols, "Optimum settings for automatic controllers," *trans. ASME*, vol. 64, no. 11, 1942.

[68] S. Hamaza, I. Georgilas, M. J. Fernandez, P. J. Sanchez-Cuevas, T. Richardson, G. Heredia, and A. Ollero, "Sensor installation and retrieval operations using an unmanned aerial manipulator," *IEEE Robotics and Automation Letters*, vol. 4, no. 3, pp. 2793 – 2800, 2019.

[69] S. Hamaza, I. Georgilas, A. Conn, G. Heredia, A. Ollero, and T. Richardson, "A compact and lightweight aerial manipulator for installation and retrieval of sensors in the environment," *Journal of Field Robotics*, vol. 1, no. 1, p. under second revision, 2019.

[70] J. J. Craig, *Introduction to robotics: mechanics and control*, vol. 3. Pearson/Prentice Hall Upper Saddle River, NJ, USA:, 2005.

[71] M. Tognon, B. Yüksel, G. Buondonno, and A. Franchi, "Dynamic decentralized control for protocentric aerial manipulators," in *2017 IEEE International Conference on Robotics and Automation (ICRA)*, pp. 6375–6380, IEEE, 2017.

[72] F. Ruggiero, V. Lippiello, and A. Ollero, "Aerial manipulation: A literature review," *IEEE Robotics and Automation Letters*, vol. 3, no. 3, pp. 1957–1964, 2018.

[73] S. Hamaza, I. Georgilas, and T. Richardson, "Energy-tank based force control for 3d contour following," in *Towards Autonomous Robotic Systems* (K. Althoefer, J. Konstantinova, and K. Zhang, eds.), (Cham), pp. 41–51, Springer International Publishing, 2019.

[74] S. Hamaza, I. Georgilas, and T. Richardson, "2d contour following with an unmanned aerial manipulator: Towards tactile-based aerial navigation," in *2019 IEEE/RSJ International Conference on Intelligent Robots and Systems (IROS)*, p. accepted for presentation at IROS 2019, IEEE, 2019.

[75] B. Siciliano, L. Sciavicco, L. Villani, and G. Oriolo, *Robotics: modelling, planning and control*.
Springer Science & Business Media, 2010.

[76] B. Siciliano and L. Villani, *Robot force control*, vol. 540.
Springer Science & Business Media, 2012.

[77] J. De Schutter, T. De Laet, J. Rutgeerts, W. Decré, R. Smits, E. Aertbeliën, K. Claes, and H. Bruyninckx, "Constraint-based task specification and estimation for sensor-based robot systems in the presence of geometric uncertainty," *The International Journal of Robotics Research*, vol. 26, no. 5, pp. 433–455, 2007.

[78] G. Borghesan and J. De Schutter, "Constraint-based specification of hybrid position-impedance-force tasks," in *Robotics and Automation (ICRA), 2014 IEEE International Conference on*, pp. 2290–2296, IEEE, 2014.

[79] D. Berenson, S. S. Srinivasa, D. Ferguson, and J. J. Kuffner, "Manipulation planning on constraint manifolds," in *2009 IEEE International Conference on Robotics and Automation*, pp. 625–632, IEEE, 2009.

[80] D. Berenson, S. Srinivasa, and J. Kuffner, "Task space regions: A framework for pose-constrained manipulation planning," *The International Journal of Robotics Research*, vol. 30, no. 12, pp. 1435–1460, 2011.

[81] L. Sciavicco and B. Siciliano, *Modelling and control of robot manipulators*.
Springer Science & Business Media, 2012.

[82] L. Sentis and O. Khatib, "Synthesis of whole-body behaviors through hierarchical control of behavioral primitives," *International Journal of Humanoid Robotics*, vol. 2, no. 04, pp. 505–518, 2005.

[83] M. H. Raibert and J. J. Craig, "Hybrid position/force control of manipulators," *Journal of Dynamic Systems, Measurement, and Control*, vol. 103, no. 2, pp. 126–133, 1981.

[84] C. Schindlbeck and S. Haddadin, "Unified passivity-based cartesian force/impedance control for rigid and flexible joint robots via task-energy tanks," in *2015 IEEE international conference on robotics and automation (ICRA)*, pp. 440–447, IEEE, 2015.

[85] F. Ferraguti, C. Secchi, and C. Fantuzzi, "A tank-based approach to impedance control with variable stiffness," in *Robotics and Automation (ICRA), 2013 IEEE International Conference on*, pp. 4948–4953, IEEE, 2013.

[86] F. Ferraguti, N. Preda, A. Manurung, M. Bonfe, O. Lambercy, R. Gassert, R. Muradore, P. Fiorini, and C. Secchi, "An energy tank-based interactive control architecture for autonomous and teleoperated robotic surgery," *IEEE Transactions on Robotics*, vol. 31, no. 5, pp. 1073–1088, 2015.

[87] T. S. Tadele, T. J. de Vries, and S. Stramigioli, "Combining energy and power based safety metrics in controller design for domestic robots," in *2014 IEEE International Conference on Robotics and Automation (ICRA)*, pp. 1209–1214, IEEE, 2014.

[88] S. S. Groothuis, G. A. Folkertsma, and S. Stramigioli, "A general approach to achieving stability and safe behavior in distributed robotic architectures," *Front. Robot. AI 5: 108. doi: 10.3389/frobt*, 2018.

[89] M. Franken, S. Stramigioli, S. Misra, C. Secchi, and A. Macchelli, "Bilateral telemanipulation with time delays: A two-layer approach combining passivity and transparency," *IEEE transactions on robotics*, vol. 27, no. 4, pp. 741–756, 2011.

[90] A. Franchi, C. Secchi, H. I. Son, H. H. Bulthoff, and P. R. Giordano, "Bilateral teleoperation of groups of mobile robots with time-varying topology," *IEEE Transactions on Robotics*, vol. 28, no. 5, pp. 1019–1033, 2012.

[91] C. Secchi, A. Franchi, H. H. Bülthoff, and P. R. Giordano, "Bilateral teleoperation of a group of uavs with communication delays and switching topology," in *Robotics and Automation (ICRA), 2012 IEEE International Conference on*, pp. 4307–4314, IEEE, 2012.

[92] M. Tognon, E. Cataldi, H. A. T. Chavez, G. Antonelli, J. Cortés, and A. Franchi, "Control-aware motion planning for task-constrained aerial manipulation," *IEEE Robotics and Automation Letters*, vol. 3, no. 3, pp. 2478–2484, 2018.

[93] R. Spica, A. Franchi, G. Oriolo, H. H. Bülthoff, and P. R. Giordano, "Aerial grasping of a moving target with a quadrotor uav," in *2012 IEEE/RSJ International Conference on Intelligent Robots and Systems*, pp. 4985–4992, IEEE, 2012.